

國立交通大學

電子工程學系電子研究所

博士論文

高頻半導體元件電路時域模擬之研究

A Time Domain Approach to High-Frequency
Circuit Simulation of Semiconductor Devices

研究生：黃堃宇

指導教授：李建平

中華民國九十四年九月

高頻半導體元件電路時域模擬之研究

A Time Domain Approach to High-Frequency Circuit Simulation of Semiconductor Devices

研究生：黃堃宇

Student: Kuen-Yu Huang

指導教授：李建平 博士

Advisor: Dr. Chien-Ping Lee



A Dissertation
Submitted to Institute of electronics
College of Electrical Engineering and Computer Science
National Chiao Tung University
in partial Fulfillment of the Requirements
for the Degree of
Doctor of Philosophy
in
Electronics Engineering
June 2005
Hsinchu, Taiwan, Republic of China

中華民國 九十四 年 九 月

誌謝

首先要感謝我的指導老師 李建平教授，在過去八年的碩博士研習中與以無私的指導與幫助，老師不僅在學術研究上給予我教導指正，更是我在為人處世上的學習的目標，在此再向我敬重的老師表達誠摯的謝意。

在這段求學的歷程中有許多學長同學及學弟給予許多助力，與你們的相互討論及研究，使我的論文有了新的想法與更完整的研究，特別是黃忠諤博士及廖志豪學弟，在實驗量測與元件特性上，常常向兩位請教及討論，真心感謝兩位的協助。另外，李義明博士在數學理論上對我的論文可說是有關鍵性的影響，在此也要特別說明及表達感謝之意。

最後，我將我的論文獻給我的家人，有了與你們共同扶持的生活，我的生命真是豐富多彩且充滿樂趣，感謝你們，謝謝！

高頻半導體元件電路時域模擬之研究

研究生：黃堃宇

指導教授：李建平 博士

國立交通大學

電子工程學系電子研究所



為了模擬射頻穩態電路問題（意即：高頻週期性電路），在本論文中，我們發展了一個新的時域數值方法，用來解如雙調交互調頻失真 (two-tone intermodulation distortion) 之電路問題。傳統類似 SPICE 之時域電路模擬器中的暫態分析 (transient analysis) 並不適用於解高頻穩態電路問題。由於計算時域解高頻穩態電路問題的嚴苛限制條件，驅使我們發展屬於自己的時域非線性電路模擬器。此新的電路模擬器必須符合穩定、有效率的條件，並且可以處理如：半導體元件等效電路模型之強烈非線性電路問題。為此，我們成功的結合了波形分散法 (waveform relaxation method)、單調疊代法

(monotone iterative method) 與 Runge-Kutta 法 (一種常微分方程式積分法)，用之於解時域電路常微分方程式 (ordinary differential equations)，並且可以符合上述模擬高頻穩態電路之要求。此電路模擬器所用之數值方法已被證明可以收斂並於本論文中揭示其收斂特性曲線。

為了要從模擬出來的時域數值資料之擷取出有用的頻域資訊，我們也做了如離散 Fourier 轉換法 (discrete Fourier transform) 等之後續分析。在本論文中，我們使用自己發展出來的數值解題法與 Gummel-Poon 大訊號電路模型來模擬異質雙接面電晶體 (heterojunction bipolar transistors, HBTs)。于論文中，我們討論了直流電路計算、時域模擬、頻域分析與交互調頻失真特性分析 (intermodulation distortion characterization) 之結果。我們也進一步對不同的電路模擬器 (包括了我們發展的模擬器、HSPICE 與 ADS) 之模擬結果與量測數據做了相互的比較，以說明所發展的數值模擬方法是準確且有效率的。

對於操作在高偏壓與高功率的 HBT 而言，熱效應主導了元件之行為特徵。為此，我們將電熱交互作用的方程式包含到所發展的數值計算方法之中，如此可以進一步增進數值模擬之真實性。在論文的內文中詳盡討論了考慮與不考慮熱效應的電路模擬之不同處。我們

也另行模擬了一個多指 (multi-finger) HBT 上所發生之熱耦合效應 (thermal coupling effect) ，與此效應對 HBT 之直流、射頻功率與交互調頻失真等多項特性之影響。

在附錄中，我們介紹了金氧半導體場效電晶體 (metal-oxide semiconductor field-effect transistors, MOSFETs) 之 EPFL-EKV 大訊號電路模型，並且用所發展的模擬器模擬了相關的電路。此外，我們也進一步的闡述了在本論文中所提出之數值方法的收斂特性。

如本論文所言，我們所發展之數值計算方法不但可以用來解時域電路之非線性常微分方程，也可以推廣應用到包含更多數量及更多種類的半導體元件之高頻電路模擬上。

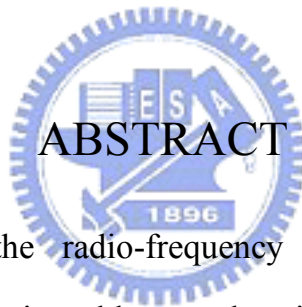


A Time Domain Approach to High-Frequency Circuit Simulation of Semiconductor Devices

Student: Kuen-Yu Huang

Advisor: Dr. Chien-Ping Lee

Department of Electronics Engineering and Institute of Electronics,
National Chiao Tung University



In order to solve the radio-frequency (RF) steady-state, that is, high-frequency periodic circuit problem, such as intermodulation distortion, we develop a new numerical solution technique in this dissertation to simulate circuits in time-domain. Traditional transient analysis in SPICE-like time-domain solver is not suitable for RF steady-state solution. The tough criteria for solving steady-state problem in time-domain drive us to build our own time-domain circuit solver. This solver should be stable, efficient, and able to handle strongly nonlinear circuits, for instance, the large-signal models for semiconductor devices. Combining the waveform relaxation (WR) method, monotone iterative (MI) method, and Runge-Kutta (RK) method, we succeeded in solving the circuit ordinary differential equations (ODEs) in time domain

that satisfies the criteria of the RF steady-state analysis. The convergence of our developed algorithms has been proved and demonstrated in this dissertation.

We also perform subsequent analysis, such as the discrete Fourier transform (DFT), to extract the frequency-domain information from simulated time-domain data. In this dissertation, we use our numerical solution techniques to simulate the characteristics of heterojunction bipolar transistors (HBTs) with the Gummel-Poon (GP) model. The results of DC circuit calculation, time-domain simulation, frequency-domain analysis and intermodulation distortion characterization are presented. Furthermore, we compare the results of various simulators (our solver, HSPICE and ADS) with measured data to show the accuracy and efficiency of the developed method.

For HBTs under high bias and high power operation, the thermal effects dominate the behavior of the device. Therefore, we include the electrical-thermal interactive equations in our numerical solution technique to further improve the reality of the simulation. The difference between the simulations with and without thermal effects is well discussed in the context of this dissertation. In addition, we describe the thermal coupling effects of an multi-finger HBT and its influence on DC, RF power and intermodulation distortion characteristics.

In the appendixes, the EPFL-EKV compact model of the metal-oxide semiconductor field-effect transistors (MOSFETs) is discussed and the related circuits are simulated by the proposed method and HSPICE. The convergence properties of the utilized algorithms are presented in these appendixes.

According to the discussion in this dissertation, the developed approach is not only an alternative computational technique for the time-domain solution of nonlinear circuit ODEs but also can be generalized for high-frequency circuits simulation including more and variant kind of semiconductor devices.



Contents

Abstract (in Chinese)	iv
Abstract	vii
List of Tables	xiv
List of Figures	xv
1 Introduction	1
1.1 Motivation	2
1.2 Background	3
1.3 Historical Development	5
1.4 Organization of the Dissertation	6
2 Mathematical Models	8
2.1 Equivalent Circuit and Parameters of GP Model	12
2.2 Model Equations	16
2.3 Formulation of Node Equations	21
2.3.1 Nodal Equations of GP Model	22
2.3.2 Nodal Equations of Simulated Circuits	23



2.4	Summary of This Chapter	27
3	Computational Techniques and Characterization Methodology	28
3.1	Numerical Algorithms	30
3.1.1	Algorithm for Solving the System of Nonlinear Algebraic Equations	30
3.1.2	Time Domain Solution Algorithm	36
3.1.3	Runge-Kutta Method	46
3.1.4	Algorithm with Electrical-Thermal Feedback	49
3.2	Genetic Algorithm for Parameter Extraction	52
3.3	Further Analysis of Time-Domain Results	61
3.3.1	Transformation of the Time-Domain Data into Frequency-Domain	61
3.3.2	Calculation of Intermodulation Distortion Analysis	65
3.4	Measurement for Intermodulation Distortion	68
3.5	Summary of This Chapter	70
4	DC Simulation and Analysis	72
4.1	DC Simulation	74
4.2	Self-Heating Effect	79
4.3	Thermal Effects of Multi-Finger Device	83
4.4	Summary of This Chapter	90
5	Time Domain Simulation and Frequency Domain Analysis	91

5.1	Non-Thermal-Effect Simulation	93
5.2	Results with Self-Heating Effect	100
5.3	Summary of This Chapter	106
6	Intermodulation Distortion and Power Characteristics	107
6.1	Characteristics without Thermal Effects	109
6.2	Characteristics with Self-Heating Effect	116
6.3	Characteristics with Thermal Coupling Effect	121
6.4	Summary of This Chapter	129
7	Summary and Suggestions	130
7.1	Summary	131
7.2	Suggestions for Further Work	132
	References	134
 Appendix A		
	The MOSFET EKV Model	151
A.1	Equivalent Circuit	153
A.2	Model Equations	156
 Appendix B		
	EKV Model Simulation Results	162
B.1	Time Domain Simulation Results	163
B.2	Spectrum Results After FFT	166
B.3	Simulation of a Low Noise Amplifier	170

Appendix C

Convergence Properties 174

C.1 Convergence of Time-Domain Solution Algorithm 174

C.2 Convergence Properties with Thermal Effect 175

Appendix D

VITA 181

Appendix E

Publication List 183



List of Tables

2.1	A list of BJT GP model parameters.	13
2.2	A list of parameters for thermal effects modelling.	14
3.1	A list of parameters to be extracted.	54
4.1	A set of extracted parameters for Gummel-Poon model used in this study.	74
4.2	A set of extracted parameters for the GP electrical and thermal models.	80
A.1	The MOSFET EKV compact model parameters.	155

List of Figures

2.1	An illustration of Gummel-Poon large-signal equivalent circuit model for the bipolar transistor.	12
2.2	A testing circuit for an HBT without thermal network.	23
2.3	A simulation circuit for an HBT with thermal network.	24
2.4	An equivalent circuit of the investigated multi-finger HBT with high frequency input excitation.	25
3.1	A flowchart of the decoupled methodology for the stationary circuit simulation.	35
3.2	A flowchart of the proposed time-domain simulation methodology.	45
3.3	An illustration of the 4th-order Runge-Kutta method.	48
3.4	A flowchart of the proposed electrical-thermal simulation methodology.	51
3.5	The proposed weight value W for HBT model parameter extraction.	53
3.6	The employed flowchart of parameters optimization in our study.	57

3.7	A comparison of the method with and without the proposed weight value for multiple I-V curves optimization.	58
3.8	A comparison of the method with and without the proposed dynamic mutation rate scheme.	59
3.9	An illustration of the migration processes for the I-V curve optimization.	60
3.10	An illustration of discrete Fourier transformation for a given input time domain data.	63
3.11	An illustration of two-tone intermodulation characteristics for a nonlinear two-port network.	65
3.12	The ideal output amplitudes at fundamental frequencies and the IM3 products versus the input amplitudes.	66
3.13	A setup of on-wafer device testing with harmonic load-pull system.	68
4.1	A cross section view of an InGaP HBT.	75
4.2	The used circuit in the simulation of I_C-V_{BE} and I_B-V_{BE} curves.	76
4.3	Comparison of Gummel plot between the simulated results of HSPICE and our proposed method with the same device parameters.	76
4.4	The used circuit in the simulation and measurement of I_C-V_{CE} DC curves.	77
4.5	Comparison between our simulated results and measured results for I_C-V_{CE} curves of the InGaP HBT.	78

4.6	An equivalent circuit including thermal network of an HBT for DC simulation.	79
4.7	Comparison between our and HSPICE's simulated results for common-emitter I_C-V_{CC} characteristics of the HBT with self-heating effect.	81
4.8	The I_C-V_{CC} characteristics with voltage source V_{IN}	82
4.9	An equivalent circuit including thermal networks of an n -finger HBT with constant current bias.	83
4.10	The common-emitter I-V characteristics: (a) I_{CC} versus V_{CC} (b) and I_{C1} and I_{C2} versus V_{CC} of the three-finger HBT with thermal effects being considered.	86
4.11	T_{J1} with respect to V_{CC} and I_{IN}	88
4.12	T_{J2} with respect to V_{CC} and I_{IN}	89
5.1	The time-variant V_{OUT} , which is simulated by our numerical solver.	93
5.2	The time-variant V_{OUT} , which is simulated by HSPICE solver.	94
5.3	The plot for the output power spectrum ,which bases on the FFT results of Fig. 5.1.	95
5.4	The plot for the output power spectrum ,which bases on the FFT results of Fig. 5.2.	96
5.5	Zoom-in plots investigation for V_{OUT} simulated by the developed solver.	98
5.6	Zoom-in plots investigation for V_{OUT} simulated by HSPICE.	99

5.7	Zoom-in plots investigation for I_C simulated by the developed solver.	101
5.8	Zoom-in plots investigation of I_C simulated by HSPICE.	102
5.9	Spectrum of P_{OUT} simulated by our solver including the self-heating effect.	103
5.10	Spectrum of P_{OUT} simulated by HSPICE solver including the self-heating effect.	104
5.11	Spectrum of P_{OUT} simulated by our solver without the self-heating effect.	105
6.1	Output power, simulated by our solver, at the fundamental frequencies (black-filled symbol) and the IM3 products (white-filled symbol) versus input power.	109
6.2	Output power, simulated by HSPICE solver, at the fundamental frequencies (black-filled symbol) and the IM3 products (white-filled symbol) versus input power.	110
6.3	A deviation plot of OIP3 value versus frequency spacing Δf	112
6.4	Plots of OIP3 value versus J_C , where symbols are measured data and lines are simulated results of our proposed method.	113
6.5	Plots of OIP3 value versus J_C , where symbols are measured data and lines are simulated results of harmonic balance method.	114
6.6	A plot of OIP3 values versus I_{IN} , which demonstrates the difference between results with and without the self-heating effect.	116

6.7	Simulated LO-OIP3 values for an HBT under different I_{IN} and V_{CC} biases.	117
6.8	Simulated HI-OIP3 values for an HBT under different I_{IN} and V_{CC} biases.	118
6.9	A plot of OIP3 values versus I_{IN} , where V_{CC} is set to be 0.8 V.	119
6.10	A plot of OIP3 values versus I_{IN} , where V_{CC} is set to be 6.4 V.	120
6.11	Plots of output power, PAE, and power gain versus P_{in} , respectively.	121
6.12	Plots of PAE for Finger 1 and 2 versus P_{in}	122
6.13	Plots of the collector current density (J_{CC}) versus the input bias current (I_{IN}) for the cases A , B , C , and D	124
6.14	Plots of the junction temperature (T_J) versus I_{IN} for the cases B , C , and D	125
6.15	A comparison of the OIP3 values under different biases I_{IN} between the cases A and B	126
6.16	A comparison of OIP3 values of the whole device under different biases I_{IN} between the cases C and D	127
6.17	Plots of the input third-order intercept point (IIP3) values versus I_{IN} of the case C and D	128
A.1	A EKV MOSFET equivalent circuit for DC and transit analysis.	154
B.1	A MOSFET circuit for large signal time domain analysis and the EKV2.6 large signal model for MOSFET simulation.	163
B.2	A plot of V_{OUT} versus time, which is simulated by our method.	165

B.3	A plot of V_{OUT} versus time, which is simulated by HSPICE simulator.	165
B.4	The spectrum of output power calculated with time-domain data of our method.	167
B.5	The spectrum of output power calculated with HSPICE time-domain data.	167
B.6	A plot of the output power at fundamental frequencies and IM3 products simulated by our method.	169
B.7	A plot of the output power at fundamental frequencies and IM3 products simulated by HSPICE.	169
B.8	The circuit of a low noise amplifier (LNA).	171
B.9	A plot of V_{OUT} for an LNA simulated by the developed method.	172
B.10	A plot of V_{OUT} for an LNA simulated by HSPICE.	172
B.11	The spectrum of V_{OUT} simulated by the developed method.	173
B.12	The spectrum of V_{OUT} simulated by HSPICE simulator.	173
C.1	The maximum norm error of all computed unknowns versus number of the outer iterations.	175
C.2	The maximum norm error of the DC simulation versus number of the outer iterations.	176
C.3	The illustration of the chosen time steps for the convergence comparison.	177
C.4	The maximum norm error versus number of the outer iterations at time steps t_1 and t_2	178

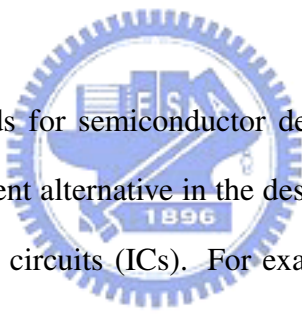
C.5 The maximum norm error versus number of the outer iterations at time steps t_3 and t_4 179

C.6 The maximum norm error of T_j versus number of the outer iterations. 180



Chapter 1

Introduction



Numerical methods for semiconductor devices, circuits and systems provide an efficient alternative in the design and fabrication of novel semiconductor integrated circuits (ICs). For example, one can simulate the semiconductor devices with a physical model, like *drift-diffusion* (DD) model or *hydrodynamic* (HD) model [1]. The partial differential equations (PDEs) of the devices with spatial information are solved to obtain electrical potential and flux. With the pre-process simulation results, before IC fabrication, the engineer can predict the behavior of the devices and design the desire function in the circuits. Furthermore, the designer can also utilize the simulation tools to correct the design after the characterization of the fabricated test ICs. The procedures of design, simulation, fabrication, and testing form an IC production period. Accurate and efficient computer-aided design tools can shorten these time periods and reduce production cost in the same time.

For integrated circuits in the radio frequency (high frequency) (RFICs), such as mixers, oscillators, low-noise amplifiers (LNAs), phase-locked loops (PLLs), and power amplifiers (PAs) [2]-[4], reliable simulation tools are necessary to shorten the design period and minimize the prime cost. Since the fabrication of RFICs is highly sensitive to semiconductor process, the designer needs more accurate simulations for circuits in order to meet the narrow design window. For RFICs applications, the physical-based simulation method is not suitable for solving the time variant problem because of its tremendous computation time. With careful physical analysis and proper approximation, the spatial variables can be pre-calculated and turned into parameters in the analytic equations. The physical based model of device structure, therefore, is simplified to model of analytic equations, called a *compact model*. In mathematics, the partial differential equations (PDEs) are transferred to ordinary differential equations (ODEs) for the integrated spatial terms.

1.1 Motivation

The junction transistor and field effect transistor are the two major types of active semiconductor devices. The bipolar junction transistor (BJT) and metal-oxide semiconductor field-effect transistor (MOSFET) are the examples of these two types of devices. In order to minimize the fabrication cost and improve the high frequency performance, the trend has been towards smaller device size since the invention of IC. Meanwhile, the "compact" models for

BJTs and MOSFETs become much more complex as device size shrinks. Furthermore, the ultra high frequency operation of devices leads many additional effects for device modelling, such as distributed capacitances and lossy transmission lines. In practical cases, the circuit model for novel devices may have near or over one hundred parameters, including the noise model and parasitic terms. The complexity of model equations is a stiff problem for the circuit simulation kernel. In other words, the capability of developing a *nonlinear circuit solver* is necessary to establish a functional device model.

In our study, we first attempt to simulate the two-tone intermodulation distortion of the heterojunction bipolar transistors (HBTs). After several failed attempts, we found that the traditional transient analysis in SPICE-like time-domain solvers [5, 6] are not suitable for the distortion analysis of strongly nonlinear circuit. The need for a more accurate and efficient circuit solver propel us to develop our own solution method. The related computation techniques and measurements for the distortion analysis are also incorporated.

Finally, we extend our numerical solution method to the MOSFET compact model after the success in simulation of the HBT circuit model.

1.2 Background

Most of the algorithms for RF nonlinear circuit simulation can be cataloged into time- and frequency-domain methods [7]-[9]. These two classes of methods are usually complementary in many aspects. Therefore, in recent years,

there have been new hybrid algorithms which combine the advantages of the two classes.

Time-domain methods are much more easily perceived in mathematics. The advantages of time-domain methods are the capability to solve a strongly nonlinear problem and less approximation. The *direct method*, also called transient analysis, solves the ODEs in time domain until the solution arrives at a steady-state. One improved method for RF steady-state simulation is the *shooting method* [10]-[12]. In this method, the ODEs for the circuits are solved by forcing the constrain that the solution is periodic in the steady-state. This condition is expressed as $\mathbf{v}(t) = \mathbf{v}(t + T)$, where \mathbf{v} is the vector of node voltage and T is the period. The algorithm determines the solution which leads to steady state as the criterion is met. The main disadvantages of the time-domain method are the stiff requirement for transient analysis and lengthy calculation time.

The basis of frequency-domain methods is the *harmonic balance method* (HB method) [13]-[18]. The HB method is a frequency-domain technique for periodic and quasi-periodic steady-state analysis of a mildly nonlinear circuit. In this method, the key idea is the application of the Kirchhoff's current law (KCL) [19] for each harmonic. The spectrum of all current at a node is balanced; in other words, the KCL is applied for each independent frequency. The HB method is formulated by expressing the ODEs in terms of a Fourier series [20, 21], then replacing the differentiation in time-domain with algebraic multiplication in frequency-domain. Each variable needs many Fourier

coefficients to guarantee the precision of this method, hence the size of this system is much larger than that of the circuit ODEs. The huge size of system requires the manipulation of relatively dense matrices and consumes a large amount of memory and CPU times. For frequency-dependent dispersive circuit elements, the HB method is capable of handling without difficulty because of the nature of the frequency-domain method.

Many improvements for the above two classes of methods have been made, such as mixed frequency-time methods [22, 23] and envelope method [24]-[27]. These are developed to solve special types of circuit analysis. We note that the mentioned methods for nonlinear RF circuit simulation are large-signal methods. There are also small-signals method, for example, the linear time-varying analysis [28] and Volterra Series analysis [29].

In our developed algorithms, we focus on the development of time-domain direct method. Based on the waveform relaxation (WR) method [30]-[32], the monotone iterative (MI) method [33]-[36], and the Runge-Kutta (RK) method [20, 21], we succeed in solving the circuit ODEs while satisfying the criteria of the RF steady-state analysis in time domain.

1.3 Historical Development

The circuit simulator first appeared in the late 1960's. However, its importance arose with the dramatic growth of the IC market in the 1970's. As the designs became larger and more complicated, the requirement for circuit simulators

increased. The development of the modern circuit simulator is credited in large part of the SPICE group at the University of California, Berkeley. The major advantage of computer-aided circuit simulation tools is formation of the matrix of nodal equations automatically by computer programs with the modified nodal analysis [37]. The modest beginning resulted in the simulation programs being developed and culminated in the release of SPICE in 1972 and SPICE2 in 1975 [5]. Because of the propagation of the standard simulator, the SPICE became very important. The source code for SPICE is available at a nominal cost. In the late 1980's, Berkeley upgraded SPICE to SPICE3 [6]. SPICE3 was written in *C* language and is easier to add new component models.

Meanwhile, Berkeley also released a new circuit simulator named Spectre [38, 39]. Spectre utilized the HB method to compute steady-state analysis of nonlinear RF circuits in the frequency domain. Spectre was further developed by Hewlett-Packard, becoming the Agilent Advanced Design System (ADS) [40]. Also, Cadence Design Systems replaced the HB algorithms with transient analysis algorithms and developed SpectreRF [41]. A more comprehensive historical development of the circuit simulator can be found in [39].

1.4 Organization of the Dissertation

The dissertation is organized as follows: In Chapter 2, we state the studied mathematical models, which include equations of equivalent circuit model,

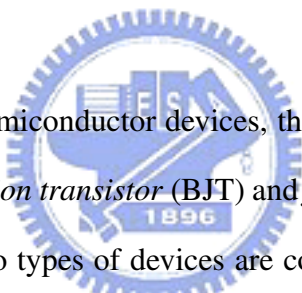
node equations, and electrical-thermal feedback equations. Then, in Chapter 3, we describe the computational techniques for the simulation of DC, time-domain, and electrical-thermal interaction. The characterization methodology for frequency-domain analysis used in this work is also introduced in this chapter. Besides, the genetic algorithm (GA) for parameter optimization and measurement for intermodulation distortion are briefly explained in Chapter 3.

To prove the advantages of our algorithms, we demonstrate the simulated and measured results for HBTs in subsequent chapters: DC simulation and analysis (Chapter 4), time domain simulation and frequency domain analysis (Chapter 5), and intermodulation distortion and power characteristics (Chapter 6). Among these chapters, we discuss the results with and without thermal effects. Our simulation results are compared with the outcomes of other simulators, such as HSPICE and Agilent ADS, and measured data. The DC, power and distortion characteristics of an multi-finger HBT are also shown in Chapter 4 and Chapter 6.

After the discussion of results, we give the conclusion and some suggestions for the future work in Chapter 7. In addition, we represent the MOSFET EKV model and related simulation results in Appendix A and Appendix B to show the capability of our kernel in solving different kinds of devices. Finally, to complete the description of our developed numerical solution algorithms, we further remark on the convergence properties of these algorithms in Appendix C.

Chapter 2

Mathematical Models



Among modern semiconductor devices, the most widely studied types are *bipolar junction transistor (BJT)* and *field effect transistor (FET)*. Though both of these two types of devices are commonly used, the physical principle of them are quite different [42]. Therefore, the formations of equivalent circuit model equations have almost nothing in common for these two types of devices. To demonstrate the adaptability of our proposed simulation kernel, we simulate HBT and MOSFET devices with the Gummel-Poon BJT model and the EKV MOSFET model, respectively.

Equivalent circuit models for BJT have been greatly improved since the middle of the twentieth century. The models change with the shift in structure and material of devices [43]-[48]. The Ebers-Moll (EM) model is a well understood large-signal model [49]. This model include main mechanisms for middle level current injection operation of bipolar transistors. By including

the concept of internal charge control, the Gummel-Poon (GP) model was introduced in 1970. The GP model improves the simulation for low and high level current injection regions. This model also considers the effects such as leakage current at collector-emitter and base-emitter junctions, β -falloff mechanism, and Kirk effect [50]-[52]. Based on EM and GP models, many complex new models have been developed in the past few decades. The researchers focus on improving performance for particular characteristics: dependency on temperature, 2-D or 3-D geometry factors, substrate and leakage current terms, physical structure and material related parameters, and parasitic terms for high frequency operation. For the GP model, there are three internal nodes in the large-signal model. The models developed in recent years have more internal nodes for better simulation of new devices. For examples, the *High-Current Model* (HICUM) [53]-[55] and *Most Exquisite Transistor Model* (MEXTRAM) [56, 57] have five internal nodes, and the *Vertical Bipolar Inter-Company* model (VBIC) [58]-[60] has six internal nodes. The increment of internal nodes can meet the requirement for better fit, but also raises difficulties in nonlinear circuit computation and model parameter extraction. In order to compare with other commercial simulators, such as HSPICE [61] and ADS [40, 62, 63], we use the most popular GP large-signal model in this work. We can still fit the measurement data well by GP model with proper extracted parameters [64].

Thermal effects influence the behavior of semiconductor devices during

DC or RF operation. Both the ambient temperature and heat generated by device power dissipation can induce thermal effects [65]-[72]. The linearity of the device, which strongly depends on bias condition, can also be affected by the thermal-effects [73]-[77]. We introduce the temperature-dependent terms into the conventional GP model. In the meanwhile, the equations, which express the relation between power dissipation and junction temperature, are formed to construct the thermal-electrical iteration loops. With above additional thermal network, our circuit model can simulate the thermal effects of the multi-finger HBT.

Furthermore, the field effect transistor, such as *metal-oxide semiconductor field-effect transistor* (MOSFET), is another important kind of semiconductor device. Though the MOSFETs are not the earliest of semiconductor transistors, they are the mostly fabricated devices today. There are several famous and popular MOSFET compact models. Two of them are the BSIM and EKV models. The BSIM model was developed by the *BSIM Research Group* in the Department of EECS at the University of California, Berkeley. In the BSIM model series [78, 79], BSIM3 is the most widely applied MOSFET model in industry today. The latest version of this model is BSIM3v3.2.4, released in December, 2001. However, as the device line width shrinks to 100 nm or narrower, the BSIM3 model becomes less precise. The BSIM4, the extension of the BSIM3 model, was developed to address the MOSFET physical behavior in the sub-100 nm regime. Though accuracy is improved, the complexity of

the model greatly increased. This situation challenges the corresponding circuit simulator and extraction procedure of model parameters. A similar trend happens to the EKV model. The EKV MOSFET model was developed by the *Electronics Laboratories*, Swiss Federal Institute of Technology (EPFL), in Lausanne, Switzerland [80]. The newest version is EKV3.0, announced in 2004, and is based on the surface potential model combined with inversion charge linearization. The number of model parameters in EKV3.0 is less than that in BSIM4, but it is still difficult to solve this model. For the simulation demonstrated in Appendix B, we list model equations of the EKV model version 2.6 in Appendix A. The EKV2.6 is the previous version of EKV model. We use it in order to compare our solver with HSPICE solver, which has the EKV2.6 model.

In this chapter, the equivalent circuit of GP model and parameters of both electrical and thermal models will be described first. Then, we write the equations of the electrical and thermal models. The internal and external node equations of circuits used in this dissertation are formed in the third section. Finally, we give a brief summary of this chapter.

2.1 Equivalent Circuit and Parameters of GP Model

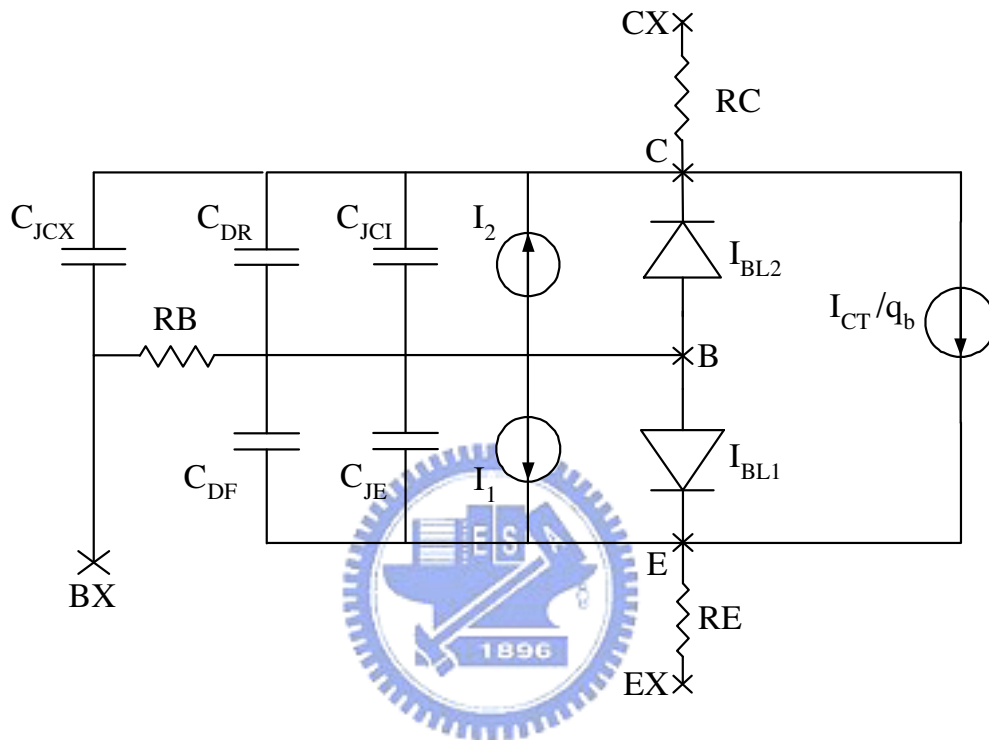


Figure 2.1: An illustration of Gummel-Poon large-signal equivalent circuit model for the bipolar transistor.

Figure 2.1 shows the equivalent circuit of a GP large-signal bipolar junction transistor. The model includes internal nodes: C, B, and E, and external nodes: CX, BX, and EX. The capacitance terms of this model are:

1. Base-emitter junction capacitance, C_{JE} ,
2. Intrinsic portion of collector-emitter junction capacitance, C_{JC1} ,
3. Extrinsic portion of collector-emitter junction capacitance, C_{JCX} ,

Notation	Description	Unit
IS	Transport saturation current	A
BF	Ideal maximum current gain in forward-active mode	-
NF	Ideality factor of the forward current	-
BR	Ideal maximum current gain in reverse-active mode	-
NR	Ideality factor of the reverse current	-
ISE	Base-emitter leakage current	A
NE	Ideality factor of the base-emitter leakage current	-
ISC	Base-collector leakage current	A
NC	Ideality factor of the base-collector leakage current	-
IKF	Corner for the forward beta high-current roll-off	A
IKR	Corner for the reverse beta high-current roll-off	A
RB	Zero bias base resistance	Ω
RE	Emitter resistance	Ω
RC	Collector resistance	Ω
CJEO	Base-emitter zero bias junction capacitance	F
VJE	Base-emitter junction built-in potential	V
MJE	Base-emitter junction exponential factor	-
CJCO	Base-collector zero bias junction capacitance	F
VJC	Base-collector junction built-in potential	V
MJC	Base-collector junction exponential factor	-
XCJC	Factor for intrinsic part of the base-collector capacitance	-
TF	Ideal forward transit time	Sec
XTF	Pre-coefficient for bias dependence of TF	-
VTF	Coefficient of V_{BC} dependence of TF	V
ITF	Coefficient of I_C dependence of TF	A
TR	Reverse transit time	Sec
FC	Coefficient for forward-bias capacitance formula	-
M	Multiplier factor for the transistor connection	-

Table 2.1: A list of BJT GP model parameters.

4. Diffusion capacitance of the charge due to forward active current, C_{DF} .
5. Diffusion capacitance of the charge due to reverse active current, C_{DR} .

The current terms, I_1 , I_2 and I_{CT} are the intermediate current variables. With these terms, we can calculate the base, collector and emitter currents. The remaining current terms, I_{BL1} and I_{BL2} , are the leakage currents of the base-emitter and base-collector junctions, respectively. Furthermore, q_b is the ratio of the base charge Q_B to the equilibrium base charge Q_{B0} .

Notation	Description	Unit
E_a	First bandgap correction factor	eV/K
E_b	Second bandgap correction factor	K
X_{TI}	Temperature exponent for IS	-
X_{TB}	Temperature exponent for BF and BR	-
BB	Fitting parameter for the thermal conductivity	-

Table 2.2: A list of parameters for thermal effects modelling.



The GP large-signal model used in this work involves 28 parameters. The purpose of these parameters can be separated into several groups. The **IS**, **BF**, **NF**, **BR** and **NR** are the main parameters for the forward and reverse current terms. The leakage current related parameters include **ISE**, **NE**, **ISC** and **NC**. **IKF** and **IKR** are introduced to model the high current region of BJT operation. The internal resistance terms include **RB**, **RC** and **RE**. There are seven parameters: **CJEO**, **VJE**, **MJE**, **CJCO**, **VJC**, **MJC** and **XCJC**, used for junction capacitance of the model. Finally, the fitting parameter **FC** and the multiplier factor **M** are also included in this model. For **M** connected

identical devices, the parameters with current or capacitance units are multiplied by M . On the other hand, the parameters with resistance units should be divided by M . A detailed description of parameters and their units are shown in Table 2.1

We also include five important parameters to simulate thermal effects. They are E_a , E_b , X_{TI} , X_{TB} and BB . Descriptions for these are listed in Table 2.2.



2.2 Model Equations

In order to implement the GP model to perform the DC and time-domain characteristic simulations, we must solve the nonlinear large-signal equations. I_1 , I_2 and I_{CT} , the intermediate current variables which dominate current behavior, can be written as follows:

$$I_1 = \frac{IS}{BF} \cdot \left[\exp \left(\frac{V_B - V_E}{NF \cdot V_T} \right) - 1 \right], \quad (2.1)$$

$$I_2 = \frac{IS}{BR} \cdot \left[\exp \left(\frac{V_B - V_C}{NR \cdot V_T} \right) - 1 \right], \text{ and} \quad (2.2)$$

$$I_{CT} = IS \cdot \left[\exp \left(\frac{V_B - V_E}{NF \cdot V_T} \right) - \exp \left(\frac{V_B - V_C}{NR \cdot V_T} \right) \right]. \quad (2.3)$$

V_T represents the thermal voltage ($V_T = \frac{kT}{q}$). For a device operated at 300K, V_T is equal to 0.0259V. In the above equations, V_B , V_C and V_E represent the voltage, which are variables to be solved, at internal node B, C and E, respectively. Leakage currents I_{BL1} and I_{BL2} are written as:

$$I_{BL1} = ISE \cdot \left[\exp \left(\frac{V_B - V_E}{NE \cdot V_T} \right) - 1 \right] \text{ and} \quad (2.4)$$

$$I_{BL2} = ISC \cdot \left[\exp \left(\frac{V_B - V_C}{NC \cdot V_T} \right) - 1 \right]. \quad (2.5)$$

Then, the base charge related term q_b is

$$q_b = \frac{q_1}{2} + \sqrt{\left(\frac{q_1}{2} \right)^2 + q_2}. \quad (2.6)$$

We note that the q_1 and q_1 in equation (2.6) are

$$q_1 = 1 + \frac{V_B - V_E}{VAF} + \frac{V_B - V_C}{VAR} \text{ and} \quad (2.7)$$

$$q_2 = \frac{\mathbf{IS}}{\mathbf{IKF}} \cdot \left[\exp \left(\frac{V_B - V_E}{\mathbf{NF} \cdot V_T} \right) - 1 \right] + \frac{\mathbf{IS}}{\mathbf{IKR}} \cdot \left[\exp \left(\frac{V_B - V_C}{\mathbf{NR} \cdot V_T} \right) - 1 \right]. \quad (2.8)$$

Equation (2.7) models the Early and reverse Early effect of a BJT device. Unlike the Si BJTs, the base-width modulation phenomenon is rarely observed in InGaP HBTs, due to heavy base doping. Therefore, the forward and reverse Early voltage, \mathbf{VAF} and \mathbf{VAR} are large enough in magnitude to approximate q_1 as 1.0 for the HBTs.

The differential voltages among node C, E, B, and BX are defined as the follows.

$$V_{BC} \equiv V_B - V_C, \quad (2.9)$$

$$V_{BE} \equiv V_B - V_E, \text{ and} \quad (2.10)$$

$$V_{BXC} \equiv V_{BX} - V_C. \quad (2.11)$$

With the simplified notation, we can write the equations of all diffusion capacitances,

$$C_{DR} = \frac{\partial \left[\mathbf{TR} \cdot \mathbf{IS} \cdot \exp \left(\frac{V_{BC}}{\mathbf{NR} \cdot V_T} \right) \right]}{\partial V_{BC}} \quad \text{and} \quad (2.12)$$

$$C_{DF} = \frac{\partial \left(\tau_F \cdot \frac{I_{bf}}{q_b} \right)}{\partial V_{BE}}; \quad (2.13)$$

and junction capacitances,

$$C_{JE} = \begin{cases} \text{CJEO} \cdot \left(1 - \frac{V_{BE}}{V_{JE}}\right)^{-MJE} \\ \quad \text{if } V_{BE} \leq \text{FC} \cdot V_{JE} \\ \text{CJEO} \cdot (1 - \text{FC})^{-MJE} \cdot \\ \quad \left[1 - \text{FC} \cdot (1 + MJE) + \frac{MJE}{V_{JE}} \cdot V_{BE}\right] \\ \quad \text{if } V_{BE} > \text{FC} \cdot V_{JE} \end{cases}, \quad (2.14)$$

$$C_{JCX} = \begin{cases} (1 - \text{XCJC}) \cdot \text{CJCO} \cdot \left(1 - \frac{V_{BXC}}{V_{JC}}\right)^{-MJC} \\ \quad \text{if } V_{BXC} \leq \text{FC} \cdot V_{JC} \\ (1 - \text{XCJC}) \cdot \text{CJCO} \cdot (1 - \text{FC})^{-MJC} \cdot \\ \quad \left[1 - \text{FC} \cdot (1 + MJC) + \frac{MJC}{V_{JC}} \cdot V_{BXC}\right] \\ \quad \text{if } V_{BXC} > \text{FC} \cdot V_{JC} \end{cases}, \text{ and} \quad (2.15)$$

$$C_{JCI} = \begin{cases} \text{XCJC} \cdot \text{CJCO} \cdot \left(1 - \frac{V_{BC}}{V_{JC}}\right)^{-MJC} \\ \quad \text{if } V_{BC} \leq \text{FC} \cdot V_{JC} \\ \text{XCJC} \cdot \text{CJCO} \cdot (1 - \text{FC})^{-MJC} \cdot \\ \quad \left[1 - \text{FC} \cdot (1 + MJC) + \frac{MJC}{V_{JC}} \cdot V_{BC}\right] \\ \quad \text{if } V_{BC} > \text{FC} \cdot V_{JC} \end{cases}. \quad (2.16)$$

In equation (2.13), two terms can be described more clearly as

$$I_{bf} = \mathbf{IS} \cdot \left[\exp\left(\frac{V_{BE}}{\mathbf{NF} \cdot V_T}\right) - 1 \right] \quad (2.17)$$

and

$$\tau_F = \mathbf{TF} \cdot \left[1 + \mathbf{XTF} \cdot x^2 \cdot \exp\left(\frac{V_{BC}}{1.44 \cdot \mathbf{VTF}}\right) \right], \quad (2.18)$$

where

$$x = \frac{I_{bf}}{I_{bf} + \mathbf{ITF}}. \quad (2.19)$$

These represent the forward-active current and forward transit time of this device.

We also include thermal effects of HBT in this work [77]. To simulate the thermal-electrical feedback mechanism, the temperature dependant equations of some physical parameters are introduced to the GP model:

$$IS(T_J) = \mathbf{IS} \cdot \left(\frac{T_J}{T_N}\right)^{\mathbf{xTI}} \cdot \exp\left[\left(\frac{E_g(T_N)}{\mathbf{k} \cdot T_N}\right) - \left(\frac{E_g(T_J)}{\mathbf{k} \cdot T_J}\right)\right], \quad (2.20)$$

$$ISE(T_J) = \mathbf{ISE} \cdot \left(\frac{T_J}{T_N}\right)^{\frac{\mathbf{xTI}}{\mathbf{NE}} - \mathbf{xTB}} \cdot \exp\left[\left(\frac{E_g(T_N)}{\mathbf{NE} \cdot \mathbf{k} \cdot T_N}\right) - \left(\frac{E_g(T_J)}{\mathbf{NE} \cdot \mathbf{k} \cdot T_J}\right)\right], \quad (2.21)$$

$$ISC(T_J) = \mathbf{ISC} \cdot \left(\frac{T_J}{T_N}\right)^{\frac{\mathbf{xTI}}{\mathbf{NC}} - \mathbf{xTB}} \cdot \exp\left[\left(\frac{E_g(T_N)}{\mathbf{NC} \cdot \mathbf{k} \cdot T_N}\right) - \left(\frac{E_g(T_J)}{\mathbf{NC} \cdot \mathbf{k} \cdot T_J}\right)\right], \quad (2.22)$$

$$BF(T_J) = \mathbf{BF} \cdot \left(\frac{T_J}{T_N}\right)^{\mathbf{xTB}}, \text{ and} \quad (2.23)$$

$$BR(T_J) = \mathbf{BR} \cdot \left(\frac{T_J}{T_N}\right)^{\mathbf{xTB}}. \quad (2.24)$$

In the equations (2.20)-(2.22), the energy band gap with temperature dependency is shown as

$$E_g(T_J) = E_g(T_N) + \frac{\mathbf{E}_a \cdot T_N^2}{T_N + \mathbf{E}_b} + \frac{\mathbf{E}_a \cdot T_J^2}{T_J + \mathbf{E}_b}, \quad (2.25)$$

where T_J and T_N are junction and nominal temperatures, respectively. In our case, T_N is set to be the ambient temperature, which is 300K. We need to note that T_N is the temperature on the back of the substrate for the highly powered devices. Above equations include the temperature-dependent parameters, not

involved in the original GP model. The parameters are transport saturation current $IS(T_J)$, base-emitter leakage current $ISE(T_J)$, base-collector leakage current $ISC(T_J)$, ideal forward current gain $BF(T_J)$, and ideal reverse current gain $BR(T_J)$.

The thermal model also expresses the relation between power dissipation and junction temperature. In consideration of temperature-dependent thermal conductivity, the junction temperature for an n -finger HBT is

$$\mathbf{T}_J = T_N \left\{ 1 - \frac{(BB - 1)}{T_N} [\mathbf{R}_{TH} \cdot \mathbf{P}_D] \right\}^{\frac{-1}{BB-1}} = \begin{bmatrix} T_{J1} \\ T_{J2} \\ \vdots \\ T_{Jn} \end{bmatrix}, \quad (2.26)$$

where T_{Jn} is the junction temperature of n -th finger [42, 52, 71, 72]. $\mathbf{R}_{TH} \cdot \mathbf{P}_D$ is given by

$$\mathbf{R}_{TH} \cdot \mathbf{P}_D = \begin{bmatrix} R_{T11} & R_{T12} & \dots & R_{T1n} \\ R_{T21} & R_{T22} & & R_{T2n} \\ \vdots & & \ddots & \vdots \\ R_{Tn1} & R_{Tn2} & & R_{Tnn} \end{bmatrix} \cdot \begin{bmatrix} P_{D1} \\ P_{D2} \\ \vdots \\ P_{Dn} \end{bmatrix}. \quad (2.27)$$

Here R_{Tnn} and R_{Tnm} denote the self-heating thermal resistance of n -th finger and the coupling thermal resistance which includes the coupled heat from m -th finger to n -th finger. Furthermore, the power dissipation of n -th finger is denoted by P_{Dn} . We note here that in general the values of \mathbf{R}_{TH} must be computed in advance with the help of a three-dimensional thermal analysis method (for example, a finite element simulation of the structures).

2.3 Formulation of Node Equations

The overall node equations for circuit simulation can be formulated by the Kirchhoff's current law (KCL) [19]. For each node KCL states:

For all lumped circuits, the algebraic sum of the currents leaving any node is equal to zero at all time t .

For circuits which consist of both linear passive and nonlinear active elements, one should formulate the nodal equations at both the external nodes and the internal nodes of active devices. It is necessary to note that KCL is employed to formulate equations for *lumped circuits* in classic circuit theory. For a lumped circuit, voltages and currents need to be well defined everywhere in the circuit. Clearly, microwave circuits cannot be treated as lumped. At microwave frequencies, distributed-circuit and radiation related to propagation of electromagnetic energy become important. In order to derive KCL from Maxwell's equations, one needs to assume slow time variations in operation [9, 17, 18]. In this regime, classic circuit theory is valid as a quasi-static approximation of general electromagnetic theory. However, Kirchhoff's laws are still applicable at high frequencies provided two requirements are met: First, distributed-circuit and radiation effects must be modeled within circuit elements since these effects are ignored by Kirchhoff's laws. Second, voltages and currents be adequately defined at terminals of every circuit element

including those introduced to model distributed-circuit and radiation effects. For instance, a section of transmission line has to be treated as a two-port. Electromagnetic coupling between two parts of the circuit connected by a transmission line has to be modeled through circuits elements like sections of coupled transmission lines or combinations of lumped elements.

2.3.1 Nodal Equations of GP Model

The GP model has three internal nodes and three external nodes for the HBTs simulated here. The substrate portion of the model is neglected because of the vertical structure of the HBTs. For the circuit shown in Fig. 2.1, we formulate the node equation at node C:

$$C_{JCX}\left(\frac{dV_{BX}}{dt} - \frac{dV_C}{dt}\right) + C_{DR}\left(\frac{dV_B}{dt} - \frac{dV_C}{dt}\right) + C_{JCI}\left(\frac{dV_B}{dt} - \frac{dV_C}{dt}\right) + I_2 + I_{BL2} - \frac{I_{CT}}{q_b} + \frac{V_{CX} - V_C}{RC} = 0, \quad (2.28)$$

node E:

$$C_{DF}\left(\frac{dV_B}{dt} - \frac{dV_E}{dt}\right) + C_{JE}\left(\frac{dV_B}{dt} - \frac{dV_E}{dt}\right) + I_1 + I_{BL1} + \frac{I_{CT}}{q_b} + \frac{V_{EX} - V_E}{RE} = 0, \text{ and} \quad (2.29)$$

node B:

$$C_{DR}\left(\frac{dV_B}{dt} - \frac{dV_C}{dt}\right) + C_{JCI}\left(\frac{dV_B}{dt} - \frac{dV_C}{dt}\right) + C_{DF}\left(\frac{dV_B}{dt} - \frac{dV_E}{dt}\right) + C_{JE}\left(\frac{dV_B}{dt} - \frac{dV_E}{dt}\right) + I_1 + I_{BL1} + I_2 + I_{BL2} + \frac{V_B - V_{BX}}{RB} = 0. \quad (2.30)$$

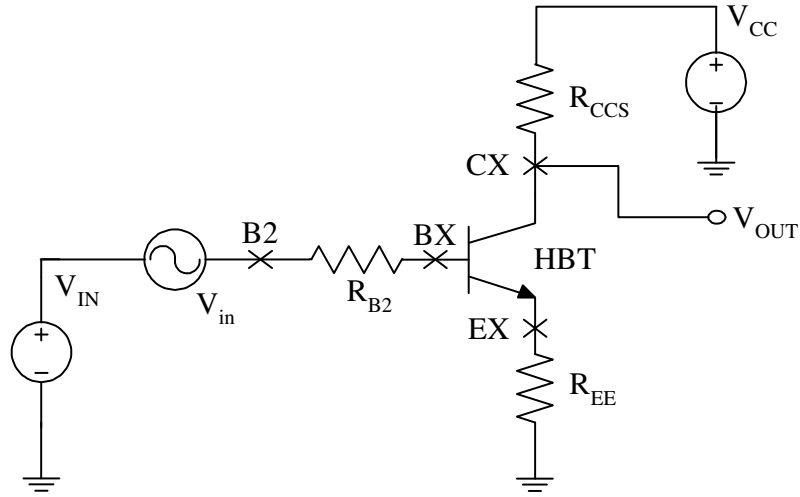


Figure 2.2: A testing circuit for an HBT without thermal network.

2.3.2 Nodal Equations of Simulated Circuits

The external nodes of the active device are connected by lumped elements or other active devices. At these connecting nodes, the external nodal equations are formulated with KCL. For the circuit as shown in Fig. 2.2, four node equations are given by the following,

node BX:

$$C_{JCX} \left(\frac{dV_C}{dt} - \frac{dV_{BX}}{dt} \right) + \frac{V_B - V_{BX}}{R_B} + \frac{V_{B2} - V_{BX}}{R_{B2}} = 0, \quad (2.31)$$

node B2:

$$V_{B2} = V_{IN} + V_{in}, \quad (2.32)$$

node CX:

$$\frac{V_C - V_{CX}}{RC} + \frac{V_{CC} - V_{CX}}{R_{CCS}} = 0, \text{ and} \quad (2.33)$$

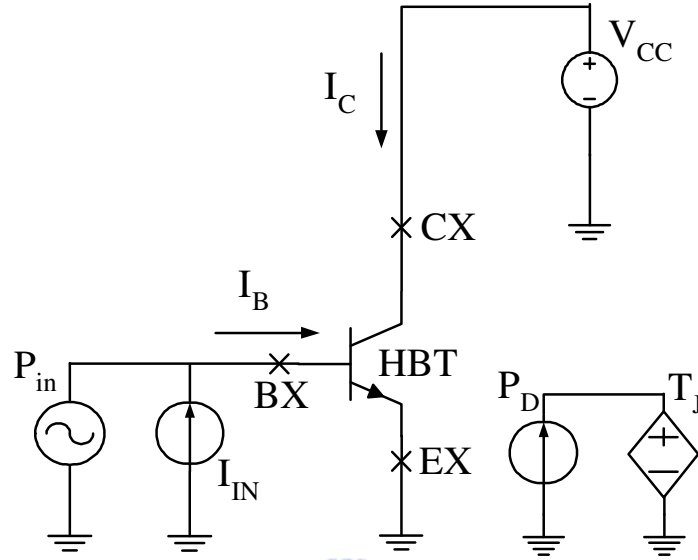


Figure 2.3: A simulation circuit for an HBT with thermal network.

node EX:

$$\frac{V_E - V_{EX}}{R_E} - \frac{V_{EX}}{R_{EE}} = 0. \quad (2.34)$$

In this circuit, V_{CC} and V_{IN} are the DC bias voltages. Time-variant voltage input excitation is denoted by V_{in} . This circuit also includes resistors which serious connect node BX to B2, node EX to ground, and node CX to voltage source V_{CC} . R_{B2} , R_{EE} , and R_{CCS} represent these series resistors, respectively.

To simulate the single-finger HBT with self-heating effect, the electrical circuit and thermal network is plotted in Fig. 2.3. P_D and T_J represent the power dissipation and junction temperature, respectively. V_{CC} and I_{IN} , are collector bias voltage and base injection current. The input excitation is a sinusoidal power signal P_{in} . External nodal equations at node BX, CX, and

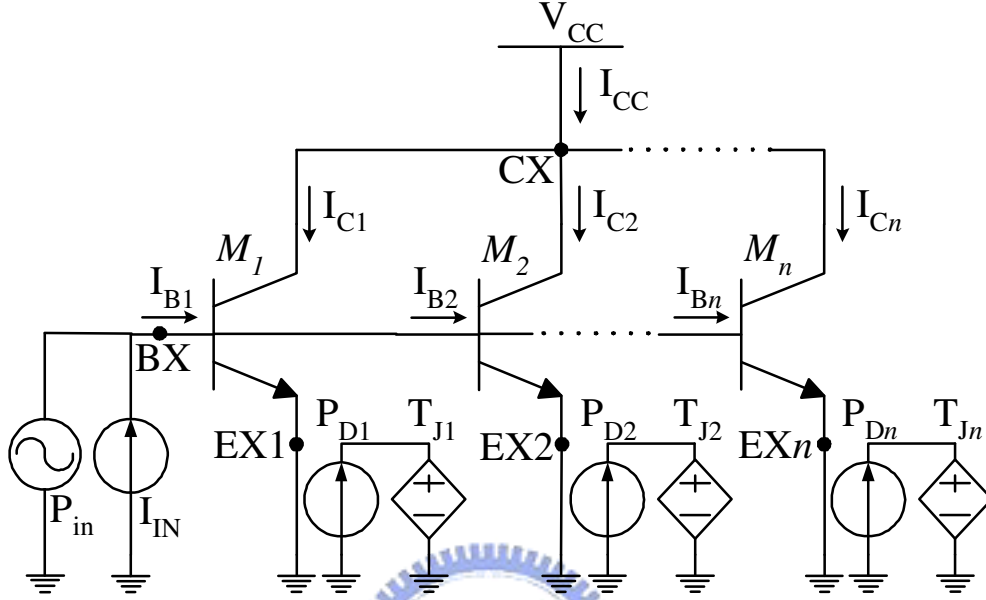


Figure 2.4: An equivalent circuit of the investigated multi-finger HBT with high frequency input excitation.

EX are written as

$$C_{JcX} \left(\frac{dV_C}{dt} - \frac{dV_{BX}}{dt} \right) + \frac{V_B - V_{BX}}{RB} + I_{IN} + \frac{P_{in}}{V_{BX}} = 0, \quad (2.35)$$

$$V_{CX} = V_{CC}, \text{ and} \quad (2.36)$$

$$V_{EX} = 0. \quad (2.37)$$

For an n -finger HBT, we draw the equivalent circuit with thermal networks in Fig. 2.4. The whole device is represented by a circuit of n shunted transistors. The k -th finger is denoted by M_k , $k = 1, 2, \dots, n$. The voltage, current, power dissipation, and junction temperature of each distinct finger can be written as V_{Xk} , I_{Xk} , P_{Dk} and T_{Jk} . Each finger is excited by the same time-variant

power source P_{in} and biased with the same DC voltage source V_{CC} at collector and DC current source I_{IN} at base. Now we list the node equations of external nodes:

at node BX:

$$\sum_{k=1}^n C_{JCXk} \left(\frac{dV_{Ck}}{dt} - \frac{dV_{BX}}{dt} \right) + \sum_{k=1}^n \frac{V_{Bk} - V_{BX}}{RB} + I_{IN} + \frac{P_{in}}{V_{BX}} = 0, \quad (2.38)$$

at node CX:

$$V_{CX} = V_{CC}, \quad (2.39)$$

and at Node EX of k -th finger:

$$V_{EXk} = 0, \quad k = 1, 2, \dots, n. \quad (2.40)$$

Finally, the input excitations for above circuits need to be defined more rigorously. For the circuit in Fig. 2.2, the two-tone input excitation is a time-variant voltage source

$$V_{in} = V_m [\cos(\omega_1 t) + \cos(\omega_2 t)], \quad (2.41)$$

where $\omega_1 = 2\pi f_1$ and $\omega_2 = 2\pi f_2$. f_1 and f_2 are fundamental frequencies of the two-tone signal. The amplitude of this signal is denoted by V_m .

On the other hand, for the circuit in Fig. 2.3 and Fig. 2.4, the input power signal of two-tone modulation is written as

$$P_{in} = P_m [\cos(\omega_1 t) + \cos(\omega_2 t)], \quad (2.42)$$

where P_m represents the amplitude of the time-variant input signal. Here we define the input signal as power sources because of the convenience in identifying the input power level in the frequency-domain.

2.4 Summary of This Chapter

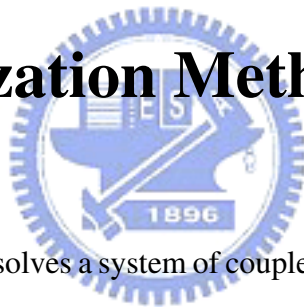
In this chapter, we discussed the following issues in detail:

- the equations of GP large-signal model,
- a brief description for the parameters of GP model,
- the testing circuits utilized in this study,
- the internal and external node equations for the testing circuits, and
- the equations for the thermal-electrical interaction.

All the equations and parameters mentioned in this chapter will be used in the numerical methods to be presented in Chapter 3. In addition, we will also demonstrate the simulation and measurement results of the tested circuits in this dissertation.

Chapter 3

Computational Techniques and Characterization Methodology



Circuit simulation solves a system of coupled ordinary differential equations (ODEs) in time- or frequency-domain. These ODEs are the node or loop equations formulated by electrical circuit analysis. The nodal equations of linear lumped elements can be formulated in matrix form automatically by computer programs [9]. The major difficulty arises from the nonlinear portion of the circuit. Here, our efforts focus on solving the nonlinear elements in the time domain without neglecting details. We introduce the waveform relaxation (WR) method [30]-[32] and monotone iterative (MI) method [33]-[36] to solve the ODEs in the time domain directly. With the proposed algorithms, we overcome error propagation, the major problem of two-tone analysis in the time domain. The solution maintains accuracy after

many simulated time steps.

This chapter is organized as follows. In section 3.1, we state the numerical algorithms for both stationary and time-variant circuit simulation. In the second section, we introduce the genetic algorithm (GA) for parameter extraction and optimization. For further analysis, additional calculation techniques for the simulated time-domain data are presented in Sec. 3.3. These methods provide useful information in frequency-domain, such as the intermodulation distortion characteristic. In the fourth section, the measurement for intermodulation characterization is described briefly. Finally, a brief summary of this chapter is given.



3.1 Numerical Algorithms

After the formulation of node equations are , the circuit simulation still need to solve them correctly. In this section, we will present a time-domain circuit simulation method. In order to solve the system of ODEs in the large-scale time period efficiently, we propose a decoupled and globally convergent simulation technique for solving the system ODEs. First, under the steady state condition, we find the DC solutions, which provide a starting point to compute the time dependent solutions.

3.1.1 Algorithm for Solving the System of Nonlinear Algebraic Equations



DC equilibrium is an important parts of circuit analysis. In a traditional RLC circuit, the circuit equations form a system of algebraic-differential equations represetned by:

$$\frac{\partial q(x)}{\partial t} + F(x) - i(t) = 0 . \quad (3.1)$$

Under certain conditions, the circuit will reach an equilibrium state, where all circuit variables such as currents, voltages, and charges are time-invariant. In this situation, the time varying function $\frac{\partial q(x)}{\partial t}$ will become zero, and $i(t)$ is replaced by the constant i_0 . Hence the equation (3.1) becomes

$$F(x_0) - i_0 = 0 . \quad (3.2)$$

The unknown to be solved is x_0 . Due to the strongly nonlinear function F , the DC analysis problem is hard to solve and can even challenge the most robust algorithms, such as Newton's method.

Under the DC condition, the capacitor can be seen as an open circuit. By applying KCL to the circuit shown in Fig. 2.2, we can formulate a system of nonlinear algebraic equations for DC simulation. In other words, the equations (2.28)-(2.30) and (2.31)-(2.34) become

$$I_2 + I_{BL2} - \frac{I_{CT}}{q_b} + \frac{V_{CX} - V_C}{RC} = 0, \quad (3.3)$$

$$I_1 + I_{BL1} + \frac{I_{CT}}{q_b} + \frac{V_{EX} - V_E}{RE} = 0, \quad (3.4)$$

$$I_1 + I_{BL1} + I_2 + I_{BL2} + \frac{V_B - V_{BX}}{RB} = 0, \quad (3.5)$$

$$\frac{V_{B2} - V_{BX}}{R_{B2}} = 0, \quad (3.6)$$

$$V_{B2} = V_{IN}, \quad (3.7)$$

$$\frac{V_C - V_{CX}}{RC} + \frac{V_{CC} - V_{CX}}{R_{CCS}} = 0, \text{ and} \quad (3.8)$$

$$\frac{V_E - V_{EX}}{RE} - \frac{V_{EX}}{R_{EE}} = 0. \quad (3.9)$$

The unknowns are V_C , V_E , V_B , V_{BX} , V_{CX} , and V_{EX} .

If we let f be a general form of these nonlinear equations,

$$f : \mathcal{D} \rightarrow \mathbb{R}^n. \quad (3.10)$$

The node equations (3.3)-(3.9) can be rewritten as

$$\begin{aligned}
 f_C(V_C, V_E, V_B, V_{BX}, V_{EX}, V_{CX}) &= I_2 + I_{BL2} - \frac{I_{CT}}{q_b} + \frac{V_{CX} - V_C}{RC} = 0, \\
 f_E(V_C, V_E, V_B, V_{BX}, V_{EX}, V_{CX}) &= I_1 + I_{BL1} + \frac{I_{CT}}{q_b} + \frac{V_{EX} - V_E}{RE} = 0, \\
 f_B(V_C, V_E, V_B, V_{BX}, V_{EX}, V_{CX}) &= I_1 + I_{BL1} + I_2 + I_{BL2} + \frac{V_B - V_{BX}}{RB} = 0, \\
 f_{BX}(V_C, V_E, V_B, V_{BX}, V_{EX}, V_{CX}) &= \frac{V_{IN} - V_{BX}}{R_{B2}} = 0, \\
 f_{CX}(V_C, V_E, V_B, V_{BX}, V_{EX}, V_{CX}) &= \frac{V_C - V_{CX}}{RC} + \frac{V_{CC} - V_{CX}}{R_{CCS}} = 0, \text{ and} \\
 f_{EX}(V_C, V_E, V_B, V_{BX}, V_{EX}, V_{CX}) &= \frac{V_E - V_{EX}}{RE} - \frac{V_{EX}}{R_{EE}} = 0.
 \end{aligned} \tag{3.11}$$

Involving a notational change,

$$Z = \begin{pmatrix} V_C \\ V_E \\ V_B \\ V_{BX} \\ V_{CX} \\ V_{EX} \end{pmatrix}, \tag{3.12}$$

and decoupled Scheme shown in Fig. 3.1, the iteration can be written as

$$\begin{aligned}
f_C(Z^{(k)} \rightarrow V_C^{(k+1)}) &= 0, \\
f_E(Z^{(k)}, V_C^{(k+1)} \rightarrow V_E^{(k+1)}) &= 0, \\
f_B(Z^{(k)}, V_C^{(k+1)}, V_E^{(k+1)} \rightarrow V_B^{(k+1)}) &= 0, \\
f_{BX}(Z^{(k)}, V_C^{(k+1)}, V_E^{(k+1)}, V_B^{(k+1)} \rightarrow V_{BX}^{(k+1)}) &= 0, \\
f_{CX}(Z^{(k)}, V_C^{(k+1)}, V_E^{(k+1)}, V_B^{(k+1)}, V_{BX}^{(k+1)} \rightarrow V_{CX}^{(k+1)}) &= 0, \text{ and} \\
f_{EX}(Z^{(k)}, V_C^{(k+1)}, V_E^{(k+1)}, V_B^{(k+1)}, V_{BX}^{(k+1)}, V_{CX}^{(k+1)} \rightarrow V_{EX}^{(k+1)}) &= 0.
\end{aligned}
\tag{3.13}$$

Giving initial guesses $V_C^{(0)}$, $V_E^{(0)}$, $V_B^{(0)}$, $V_{BX}^{(0)}$, $V_{CX}^{(0)}$, and $V_{EX}^{(0)}$, we first solve the nonlinear equation f_C and substitute the new V_C into f_E to approximate a new V_E . Then the algorithm proceeds by repeating the above procedure for V_B , V_{BX} , V_{CX} , and V_{EX} , respectively. Each decoupled algebraic equation is solved with the MI iterative method. When the overall outer loop error is within the error tolerance, the solution algorithm stops.

The steps of the solution algorithm shown in Fig. 3.1 are described as follows:

- **Step 1:** With the given bias conditions V_{IN} and V_{CC} , we properly input a set of values $V_X^{(0)}$ to all unknowns as initial guesses.
- **Step 2:** The system of nonlinear algebraic equations are decoupled through WR method.
- **Step 3:** With V_E , V_B , and other variables kept constant, the decoupled algebraic equation of unknown V_C are solved with MI

formula to get new $V_C^{(n+1)}$.

- **Step 4:** If the norm error $|V_C^{(n+1)} - V_C^{(n)}|$ is less than the preset tolerance (TOL), $V_C^{(n+1)}$ is used to substitute the V_C in the next algebraic equations of unknown V_E , V_B and etc. If not, **Step 3** is repeated until the norm error meets the prescribed criterion.
- **Step 5:** The new V_C solved in previous iterative loop is substituted. Then, the decoupled equation of unknown V_E are solved with other variables kept constant.
- **Step 6:** If the norm error $|V_E^{(n+1)} - V_E^{(n)}|$ is less than the preset tolerance (TOL), $V_E^{(n+1)}$ is used to substitute the V_E in the next algebraic equations of unknown V_B , V_{BX} and etc. If not, **Step 5** is repeated until the norm error meets the prescribed criterion.
- **Step 7:** Similar iterative loops as that described in **Step 5** and **Step 6** are performed for the remaining unknowns.
- **Step 8:** If all norm errors ($|V_C - V_{CO}|$, $|V_E - V_{EO}|$, ...) are less than TOL, we arrive at a set of solution for the DC simulation. If not, the data of V_{XO} is updated with newly solved V_X , and the procedure is repeated from **Step 3**.

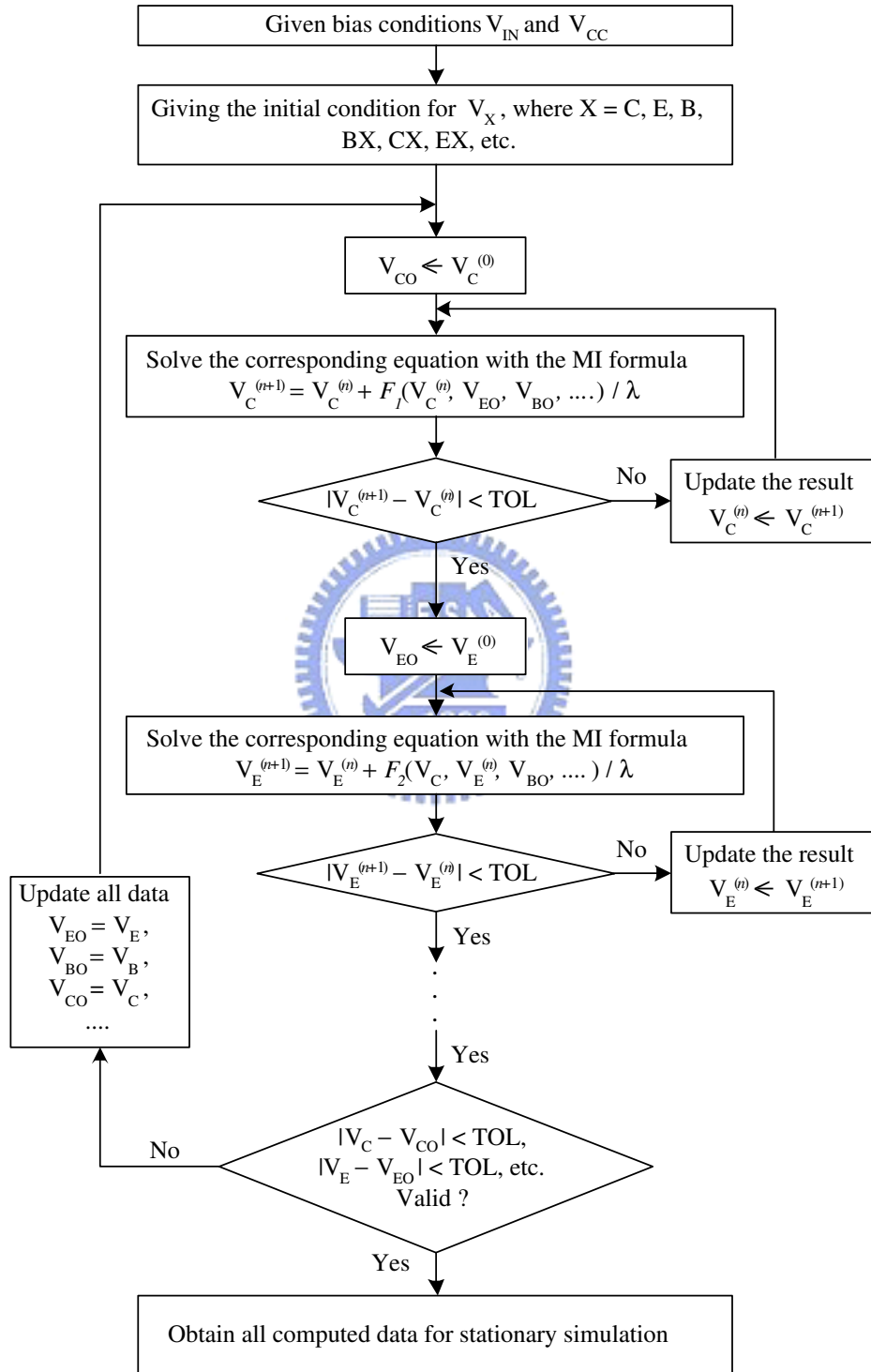


Figure 3.1: A flowchart of the decoupled methodology for the stationary circuit simulation.

3.1.2 Time Domain Solution Algorithm

In order to simulate the circuit shown in Fig. 2.2, we formulate a system of ODEs and algebraic equations by using the KCL for this circuit (see Chapter 2, equations (2.28)-(2.30) and (2.31)-(2.34)). For a specified time period T , these nonlinear ODEs needs to be solved in the time domain. The following steps are taken to accomplish this [35, 82]:

- **Step 1:** The initial time step t , total time period T , and time step Δt . are determined first.
- **Step 2:** The decoupling method is used to decouple all equations (2.28)-(2.30) and (2.31)-(2.34).
- **Step 3:** Each decoupled ODE is solved sequentially with the MI and Runge-Kutta methods.
- **Step 4:** Each MI loop is convergence tested.
- **Step 5:** Overall outer loop is convergence tested.
- **Step 6:** If the specified stopping criterion is not met for the outer loop, all data is updated with newer results and recalculate from **Step 3**.
- **Step 7:** **Step 3 - 6** are repeated until the time step meets the specified time period T .

First, all coupled ODEs are decoupled by the waveform relaxation (WR) method [30]-[32]. The WR method starts with a general nonlinear system of

\mathcal{D} ODEs with associated initial conditions,

$$\frac{dV}{dt} = f(V, t), \quad V(0) = V_0, \quad t \in [0, T], \quad (3.14)$$

where $T > 0$, $f : \mathbb{R}^{\mathcal{D}} \times [0, T] \longrightarrow \mathbb{R}^{\mathcal{D}}$, $V_0 = [V_{1,0}, V_{2,0}, \dots, V_{\mathcal{D},0}] \in \mathbb{R}^{\mathcal{D}}$ is the initial vector of V , and $V(t) = [V_1(t), V_2(t), \dots, V_{\mathcal{D}}(t)] \in \mathbb{R}^{\mathcal{D}}$ is the solution vector. The system can be written as follows:

$$\begin{cases} \frac{d}{dt} V_1 = f_1(V_1, V_2, \dots, V_{\mathcal{D}}, t), & V_1(0) = V_{1,0} \\ \frac{d}{dt} V_2 = f_2(V_1, V_2, \dots, V_{\mathcal{D}}, t), & V_2(0) = V_{2,0} \\ \vdots \\ \frac{d}{dt} V_{\mathcal{D}} = f_{\mathcal{D}}(V_1, V_2, \dots, V_{\mathcal{D}}, t), & V_{\mathcal{D}}(0) = V_{\mathcal{D},0} \end{cases} \quad (3.15)$$

The WR method for solving Eq. (3.14) is a continuous-time iterative method. Therefore, given a function which approximates the solution, it calculates a new approximation along the whole time-interval of interest. Clearly, it differs from most standard iterative techniques in that its iterations are functions in time instead of a scalar value. The iteration formula is chosen in such a way that one avoids having to solve a large system ODEs. A particularly simple, but often very effective iteration scheme which maps the old iterate $V^{(n-1)}$ is written here:

$$\left\{ \begin{array}{l} \frac{d}{dt} V_1^{(n)} = f_1(V_1^{(n)}, V_2^{(n-1)}, V_3^{(n-1)}, \dots, V_{\mathcal{D}}^{(n-1)}, t), \quad V_1^{(n)}(0) = V_{1,0} \\ \frac{d}{dt} V_2^{(n)} = f_2(V_1^{(n)}, V_2^{(n)}, V_3^{(n-1)}, \dots, V_{\mathcal{D}}^{(n-1)}, t), \quad V_2^{(n)}(0) = V_{2,0} \\ \vdots \\ \frac{d}{dt} V_{\mathcal{D}}^{(n)} = f_{\mathcal{D}}(V_1^{(n)}, V_2^{(n)}, V_3^{(n)}, \dots, V_{\mathcal{D}}^{(n)}, t), \quad V_{\mathcal{D}}^{(n)}(0) = V_{\mathcal{D},0} \end{array} \right. \quad (3.16)$$

This is similar to the Gauss-Seidel method for iteratively solving linear and nonlinear systems of algebraic equations; the so-called Gauss-Seidel waveform relaxation scheme. This scheme converts the task of solving a differential equation in \mathcal{D} variables into a task of solving a sequence of differential equations in a single variable. A closely related iteration is the Jacobi waveform relation scheme, the iteration formula is given by:

$$\left\{ \begin{array}{l} \frac{d}{dt} V_1^{(n)} = f_1(V_1^{(n)}, V_2^{(n-1)}, V_3^{(n-1)}, \dots, V_{\mathcal{D}}^{(n-1)}, t), \quad V_1^{(n)}(0) = V_{1,0} \\ \frac{d}{dt} V_2^{(n)} = f_2(V_1^{(n-1)}, V_2^{(n)}, V_3^{(n-1)}, \dots, V_{\mathcal{D}}^{(n-1)}, t), \quad V_2^{(n)}(0) = V_{2,0} \\ \vdots \\ \frac{d}{dt} V_{\mathcal{D}}^{(n)} = f_{\mathcal{D}}(V_1^{(n-1)}, V_2^{(n-1)}, V_3^{(n-1)}, \dots, V_{\mathcal{D}}^{(n)}, t), \quad V_{\mathcal{D}}^{(n)}(0) = V_{\mathcal{D},0} \end{array} \right. \quad (3.17)$$

Note that the Jacobi algorithm is fully parallel. The equations can be solved simultaneously. The Gauss-Seidel waveform relaxation algorithm is formulated in the following.

Algorithms:

$n = 0$; choose $V_x^0(t)$ for $t \in [0, T]$, $x = 1, 2, \dots, \mathcal{D}$

do

$n = n + 1$

for $x = 1, 2, \dots, \mathcal{D}$

solve $\frac{d}{dt}V_x^{(n)} = f_x(V_1^{(n)}, V_2^{(n)}, \dots, V_{x-1}^{(n)}, V_x^{(n)}, V_{x+1}^{(n-1)}, \dots, V_{\mathcal{D}}^{(n-1)}, t)$

with $V_x^n(0) = V_{x,0}$

end for

while $|V_x^n - V_x^{n-1}| < \text{TOL}$, for $x = 1, 2, \dots, \mathcal{D}$

Each decoupled ODE is solved with the MI algorithm. To clarify the MI algorithm for the numerical solution of the decoupled nonlinear ODEs, we write the ODEs (2.28)-(2.30) and (2.31) in the following form

$$\frac{dV_x}{dt} = f(V_x, t), \quad (3.18)$$

where V_x is the unknown to be solved and f is the collection of nonlinear functions from each node. We define the MI parameter $\lambda = \frac{\partial f}{\partial V_x}$ and insert λ into Eq. (3.18), arriving at the MI equation

$$\frac{dV_x}{dt} = f(\eta, t) - \lambda(V_x - \eta), \quad (3.19)$$

where $v_0 \leq \eta \leq \omega_0$ is a value in $[0, T]$, and v_0 and ω_0 are the lower and upper solutions of Eq. (3.18), respectively. Based on nonlinear behaviors of each decoupled circuit ODEs, we will show mathematically that the solution algorithm exhibits monotone convergence.

To clarify the MI algorithm [35, 36, 81] for the numerical solution of the decoupled nonlinear ODEs, we rewrite the decoupled ODEs as the following form:

$$\begin{aligned} \frac{dV_X^{(g)}}{dt} &= f(V_X^{(g)}, t) \\ V_X^{(g)}(0) &= V_{X_0}^{(g)} \end{aligned}, \quad (3.20)$$

where $V_X^{(g)}$ is the unknown to be solved, g is the decoupling index ($g = 0, 1, 2, \dots$). We note that the f is a collection of nonlinear functions with $f \in C[I \times \mathbb{R}, \mathbb{R}]$ and $I = [0, T]$. For a fixed index g and X , since the upper and lower solutions, $\overline{V}_X^{(g)}$ and $\underline{V}_X^{(g)}$, exist in the circuit and $\overline{V}_X^{(g)} \geq \underline{V}_X^{(g)}$, we can prove the solution existence in the set $\Omega = \{(t, V_X^{(g)}) \mid \overline{V}_X^{(g)} \geq V_X^{(g)} \geq \underline{V}_X^{(g)}, \forall t \in I\}$ for each decoupled circuit ODE.

Theorem 3.1.1 *Let $\overline{V}_X^{(g)}$ and $\underline{V}_X^{(g)}$ be the upper and lower solutions of Eq. (3.20) in $C^1[I \times \mathbb{R}, \mathbb{R}]$ such that $\overline{V}_X^{(g)} \geq \underline{V}_X^{(g)}$ in the time interval I and $f \in C[I \times \mathbb{R}, \mathbb{R}]$. Then there exists a solution $V_X^{(g)}$ of Eq. (3.20) such that $\overline{V}_X^{(g)} \geq V_X^{(g)} \geq \underline{V}_X^{(g)}$ in the time interval I .*

Proof 3.1.1 *It is a direct result with the continuous property of f , here the comparison theorem is applied [35]. ■*

Remark 3.1.1 *We note that for each decoupled ODE, the nonlinear function f is nonincreasing function of the unknown $V_X^{(g)}$ and the upper and lower solutions $\overline{V}_X^{(g)}(0)$ and $\underline{V}_X^{(g)}(0)$ of Eq. (3.20) in I can be found. We can further prove there exists a unique solution $V_X^{(g)}$ of Eq. (3.20) in I and $\overline{V}_X^{(g)}(0) \geq V_X^{(g)} \geq \underline{V}_X^{(g)}(0)$.*

We see that the **Theorem 3.1.1** provides an existence condition of the problem, and we can now describe a monotone constructive method for the computer simulation of the circuit ODEs. The constructed sequences will converge to the solution of Eq. (3.20) for all decoupled ODEs in the circuit simulation. In this condition, instead of original nonlinear ODE to be solved, a transformed ODE is solved with such as the RK method. Now we state the main result for the solution of each decoupled circuit ODEs.

Theorem 3.1.2 *Let the $f \in C[I \times \mathbb{R}, \mathbb{R}]$, $\overline{V}_X^{(g)}(0)$ and $\underline{V}_X^{(g)}(0)$ be the upper and lower solutions of Eq. (3.20) in I . Because $f(t, V_X^{(g)}) - f(t, \tilde{V}_X^{(g)}) \geq -\lambda(V_X^{(g)} - \tilde{V}_X^{(g)})$, $\overline{V}_X^{(g)}(0) \geq V_X^{(g)} \geq \tilde{V}_X^{(g)} \geq \underline{V}_X^{(g)}(0)$ and $\lambda \geq 0$, sequences $\overline{V}_{X_n}^{(g)} \xrightarrow{\text{unif.}} \overline{V}_X^{(g)}$ and $\underline{V}_{X_n}^{(g)} \xrightarrow{\text{unif.}} \underline{V}_X^{(g)}$ as $n \rightarrow \infty$ monotonically in I [35].*

Proof 3.1.2 *For $\mathcal{V} \in C[I \times \mathbb{R}, \mathbb{R}]$ such that $\overline{V}_X^{(g)} \geq \mathcal{V} \geq \underline{V}_X^{(g)}$, we consider the following transformed ODE equation for the fixed g and X*

$$\begin{aligned} \frac{dV_X}{dt} &= f(\mathcal{V}, t) - \lambda(V_X^{(g)} - \mathcal{V}) \\ V_X^{(g)}(0) &= V_{X_0}^{(g)} \end{aligned}, \quad (3.21)$$

then $\forall \mathcal{V}, \exists ! V_X^{(g)}$ of Eq. (3.20) in I . Define $\Theta \mathcal{V} = V_X^{(g)}$ and we can prove: (i) $\Theta \overline{V}_X^{(g)}(0) \geq \overline{V}_X^{(g)}(0)$ and $\Theta \underline{V}_X^{(g)}(0) \leq \underline{V}_X^{(g)}(0)$; (ii) Θ is a monotone operator in $[\overline{V}_X^{(g)}(0), \underline{V}_X^{(g)}(0)] \equiv [V_X^{(g)} \in C[I, \mathbb{R}] \mid \overline{V}_X^{(g)}(0) \geq V_X^{(g)} \geq \underline{V}_X^{(g)}(0)]$.

Now we construct two sequences by using the mapping $\Theta : \Theta \overline{V}_{X_n}^{(g)} = \overline{V}_{X_{n+1}}^{(g)}$ and $\Theta \underline{V}_{X_n}^{(g)} = \underline{V}_{X_{n+1}}^{(g)}$ and by above observations, the following relation holds

$$\overline{V}_{X_0}^{(g)} \geq \cdots \geq \overline{V}_{X_n}^{(g)} \geq \underline{V}_{X_n}^{(g)} \geq \cdots \geq \underline{V}_{X_0}^{(g)}$$

in I. Hence $\overline{V}_{X_n}^{(g)} \xrightarrow{\text{unif.}} \overline{V}_X^{(g)}$ and $\underline{V}_{X_n}^{(g)} \xrightarrow{\text{unif.}} \underline{V}_X^{(g)}$ as $n \rightarrow \infty$ monotonically in

I. Furthermore the $\overline{V}_{X_n}^{(g)}$ and $\underline{V}_{X_n}^{(g)}$ satisfy

$$\begin{cases} \frac{d\underline{V}_{X_{n+1}}^{(g)}}{dt} = f(\underline{V}_{X_n}^{(g)}, t) - \lambda(\underline{V}_{X_{n+1}}^{(g)} - \underline{V}_{X_n}^{(g)}) \\ \underline{V}_{X_n}^{(g)}(0) = V_{X_0}^{(g)} \end{cases}, \quad (3.22)$$

and

$$\begin{cases} \frac{d\overline{V}_{X_{n+1}}^{(g)}}{dt} = f(\overline{V}_{X_n}^{(g)}, t) - \lambda(\overline{V}_{X_{n+1}}^{(g)} - \overline{V}_{X_n}^{(g)}) \\ \overline{V}_{X_n}^{(g)}(0) = V_{X_0}^{(g)} \end{cases}, \quad (3.23)$$

respectively. Thus $\overline{V}_X^{(g)}$ and $\underline{V}_X^{(g)}$ are the solution of Eq. (3.20). ■

Theorem 3.1.3 For decoupled ODEs. the nonlinear function f is nonincreasing in $V_X^{(g)}$ and $f(t, V_{X_1}^{(g)}) - f(t, V_{X_2}^{(g)}) \geq -\lambda(V_{X_1}^{(g)} - V_{X_2}^{(g)})$, $\forall V_{X_1}^{(g)} \geq V_{X_2}^{(g)}$. Thus $\{\overline{V}_{X_n}^{(g)}\}_{n=1}^{\infty}$ and $\{\underline{V}_{X_n}^{(g)}\}_{n=1}^{\infty}$ converge uniformly and monotonically to the unique solution $V_X^{(g)}$ of Eq. (3.20) [35].

Proof 3.1.3 By using Theorem 2 and note the nonincreasing property of f , the result follows directly. ■

Fig. 3.3 shows the flowchart of the proposed time domain simulation methodology. In order to solve the equations (2.28)-(2.30) and (2.31)-(2.34) in the time domain, we solve V_C , V_E , V_B , V_{BX} , V_{CX} , and V_{EX} sequentially by the decoupled scheme of the system ODEs. Here we state the computational steps of the methodology:

- **Step 1:** For a given time interval T , we obtain the DC solution as an initial guess and start the time evolution processes.
- **Step 2:** Giving a time step (t) , we can apply the MI and Runge-Kutta (RK) method [20, 21] to solve the decoupled ODE in Eq. (2.28) with the solved solution $(V_C^{(t-1)}, V_E^{(t-1)}, V_B^{(t-1)}, V_{BX}^{(t-1)}, V_{CX}^{(t-1)})$. The notation $V_X^{(t-1)}$ represents the solution of voltage V_X at time step $(t-1)$. In the monotone loop, $V_C^{(t-1)}$ has been solved with the RK formula (fourth-order RK method is used in practical case). The estimation time step of RK method is adaptive to fit the error tolerance criterion in this work [20].
- **Step 3:** If the norm error $|V_C^{(t)} - V_{CO}^{(t)}|$ is less than the given error tolerance value (TOL), the solution algorithm will exit the monotone loop and enter the next decoupled ODE Eq. (2.29). Otherwise we update $V_{CO}^{(t)}$ with $V_C^{(t)}$ and continue the monotone loop described in **Step 2** until the tolerance condition has been achieved.

- **Step 4:** With the newly solved $V_C^{(t)}$, we can solve the ODE Eq. (2.29) with the same method as described in **Step 2**.
- **Step 5:** When the norm error $|V_E^{(t)} - V_{EO}^{(t)}|$ is less than TOL, we solve the next ODE Eq. (2.30) with the new results $(V_C^{(t)}, V_E^{(t)})$. Otherwise we return to the **Step 4**.
- **Step 6:** Similar iterative loops, such as that formed by **Step 2** and **Step 3**, are executed for all unknown variables. As $(V_C^{(t)}, V_E^{(t)}, V_B^{(t)}, V_{BX}^{(t)}, V_{CX}^{(t)})$ converge in their respective inner loops, we apply the convergence test for the overall outer loop. If the outer loop error is less than the TOL, this calculated set of $(V_C^{(t)}, V_E^{(t)}, V_B^{(t)}, V_{BX}^{(t)}, V_{CX}^{(t)})$ is the solution for this given time step (t) . The process is then repeated for the next time step $(t + 1)$. If the TOL is not satisfied, we update all $(V_{CO}^{(t)}, V_{EO}^{(t)}, V_{BO}^{(t)}, V_{BXO}^{(t)}, V_{CXO}^{(t)})$ and continue the inner loop for each ODE until the outer loop tolerance condition is met.
- **Step 7:** When t exceeds the given time interval T , the simulation will terminate and the results be ready for further processes, such as fast Fourier transform (FFT).

The convergence properties of this time-domain solution algorithm are presented in Appendix C.

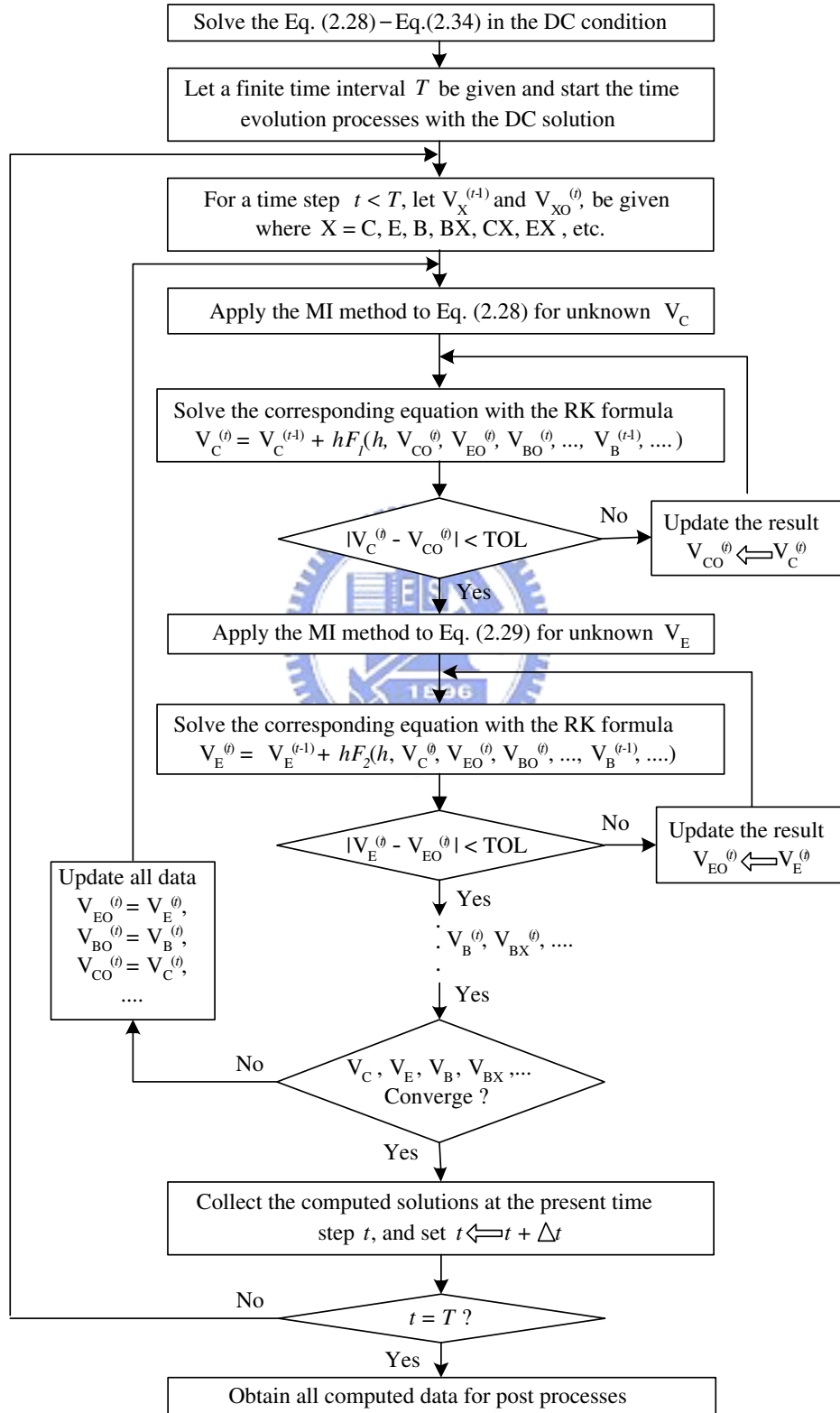


Figure 3.2: A flowchart of the proposed time-domain simulation methodology.

3.1.3 Runge-Kutta Method

In previous subsection, we combined the *Runge-Kutta* (RK) and MI method in the time-domain algorithm. The RK method is a type of ODEs integrations [20, 21]. The ODEs for circuit analysis are usually initial value problems and RK method is suitable for solving these equations. The generic problem in our simulation cases can be reduced to a set of N coupled first-order ODEs, having the general form

$$\frac{dy_i(t)}{dt} = f_i(t, y_1, \dots, y_N), \quad i = 1, \dots, N, \quad (3.24)$$

where f_i are known functions. By the WR method, we can decouple these ODEs and treat the problem as a simple ODE in one local iteration loop.

$$\frac{dy(t)}{dt} = f(t, y), \quad y(0) = y_0, \quad (3.25)$$

where y_0 gives the initial condition. We define the value of $y(t)$ at point t_n as y_n and the time interval as h . The objective of RK method is to calculate the solution $y_{n+1} = y(t_{n+1}) = y(t_n + h)$ with a known value of y_n . To reach the goal, we integrate Eq. (3.25) over the interval $[t_n, t_{n+1}]$ as

$$y_{n+1} = y_n + \int_{t_n}^{t_{n+1}} f(t, y) dt. \quad (3.26)$$

The RK method are derived by applying a numerical integration method to the integral on the right hand side of Eq. (3.26). Here we approximate the integral by trapezoidal rule.

$$\int_{t_n}^{t_{n+1}} f(t, y) dt \simeq \frac{1}{2}h[f(t_n, y_n) + f(t_{n+1}, y_{n+1})]. \quad (3.27)$$

In this equation, y_{n+1} is still unknown and can be estimated by the forward Euler method. We denote the estimated value as \tilde{y}_{n+1} . Then, Eq. (3.27) becomes

$$\begin{aligned} \tilde{y}_{n+1} &= y_n + hf(t_n, y_n) \quad \text{and} \\ y_{n+1} &= y_n + \frac{h}{2}[f(t_n, y_n) + f(t_{n+1}, \tilde{y}_{n+1})]. \end{aligned} \quad (3.28)$$

The scheme derived above is named the second-order Runge-Kutta method.

We summarize the 2nd-order RK method in a more standard form:

$$\begin{aligned} k_1 &= hf(t_n, y_n), \\ k_2 &= hf(t_{n+1}, y_n + k_1), \text{ and} \\ y_{n+1} &= y_n + \frac{1}{2}(k_1 + k_2) + O(h^3). \end{aligned} \quad (3.29)$$

Here, $O(h^3)$ represents the error term of the 2nd-order RK method.

There are higher-order methods to estimate \tilde{y}_{n+1} in Eq. (3.28) that all agree to first order, but with different coefficients of high-order terms. Here, we choose the fourth-order Runge-Kutta method. This method is accurate to the fourth-order term of the Taylor expansion, so the local error is proportional to h^5 . Based on the Simpson's 1/3 rule, the 4th-order RK is written as

$$\begin{aligned} k_1 &= hf(t_n, y_n), \\ k_2 &= hf(t_n + \frac{h}{2}, y_n + \frac{k_1}{2}), \\ k_3 &= hf(t_n + \frac{h}{2}, y_n + \frac{k_2}{2}), \\ k_4 &= hf(t_n + h, y_n + k_3), \text{ and} \\ y_{n+1} &= y_n + \frac{1}{6}(k_1 + 2k_2 + 2k_3 + k_4) + O(h^5). \end{aligned} \quad (3.30)$$

The illustration of 4th-order RK method is shown in Fig. ref4th-RK. In Sec. 3.1.2, we modified $f(t, y)$ of above equations and combined the MI method to solve

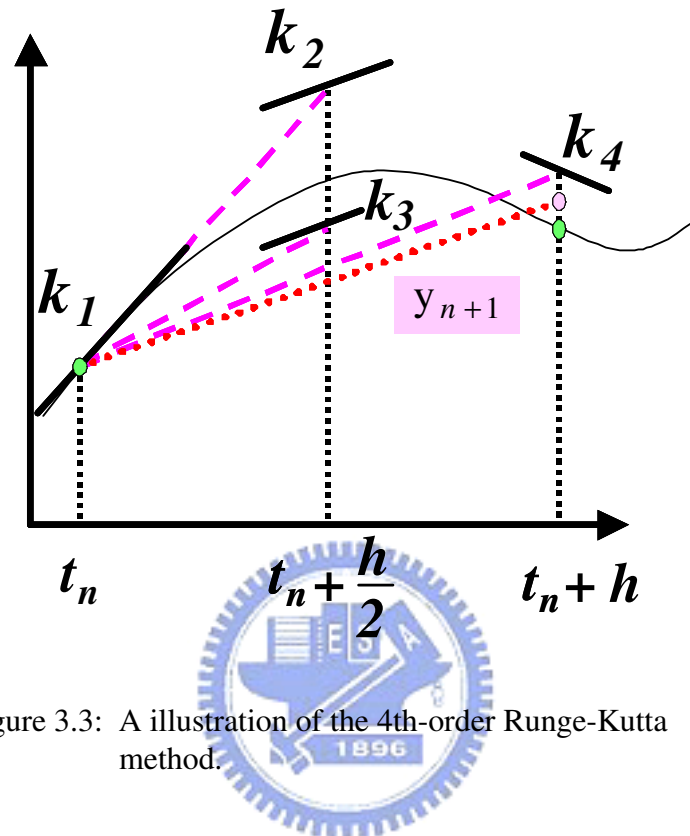


Figure 3.3: A illustration of the 4th-order Runge-Kutta method.

the ODEs of time-domain circuit simulation. Though this has 4 additional algebraic equations in each estimation, the 4th-order RK method can still remain highly efficient in the calculation for the numerical solutions of related ODEs.

3.1.4 Algorithm with Electrical-Thermal Feedback

Here, we will briefly outline the computational flowchart for the proposed electrical-thermal simulation technique, shown in Fig. 3.4. We combine the electrical and thermal models in Sec. 2.2, and perform the electrical-thermal iteration loop. This simulation technique consists of the following steps:

- **Step 1:** We set all parameters of the electrical and thermal models, DC input current, RF input power, and the nominal temperature T_N .
- **Step 2:** We initialize the junction temperature (set $T_J = T_N$).
- **Step 3:** The steady-state electrical simulation at initialized junction temperature T_J is performed;
- **Step 4:** Once convergent results are obtained, we calculate the power dissipation and solve the electrical-thermal feedback equations to get new junction temperature T_J .
- **Step 5:** Temperature dependant model parameters, such as $E_g(T_J)$, are then recalculated.
- **Step 6:** We perform the steady-state electrical simulation at this new junction temperature T_J .
- **Step 7:** Convergence tests for all the calculated currents and voltages are performed. If all computed physical quantities are convergent with the specified stopping criterion then **Step**

8 will be executed. Otherwise we return to **Step 4** for next iteration.

- **Step 8:** We set the bias condition of each finger and perform time-domain transient simulation.

The steady-state and time-domain transient simulation appeared above are accomplished by using the WR and MI techniques [35, 36, 77, 82, 83, 84]. Details of the simulation are discussed in Sec. 3.1.1 and Sec. 3.1.2. The notation T_j^n denotes the calculated junction temperature in the n -th electrical-thermal iterative loop, where $n = 0, 1, 2, 3, \dots$. According to equations (2.20)-(2.27), we perform DC simulation by our developed kernel and HSPICE simulator. For HSPICE simulation, the relation between dissipated power and junction temperature (equations (2.26) and (2.27)), should be included by user in the `.ps` file. The convergent behavior of junction temperature for both our and HSPICE's simulation are demonstrated in Appendix C.

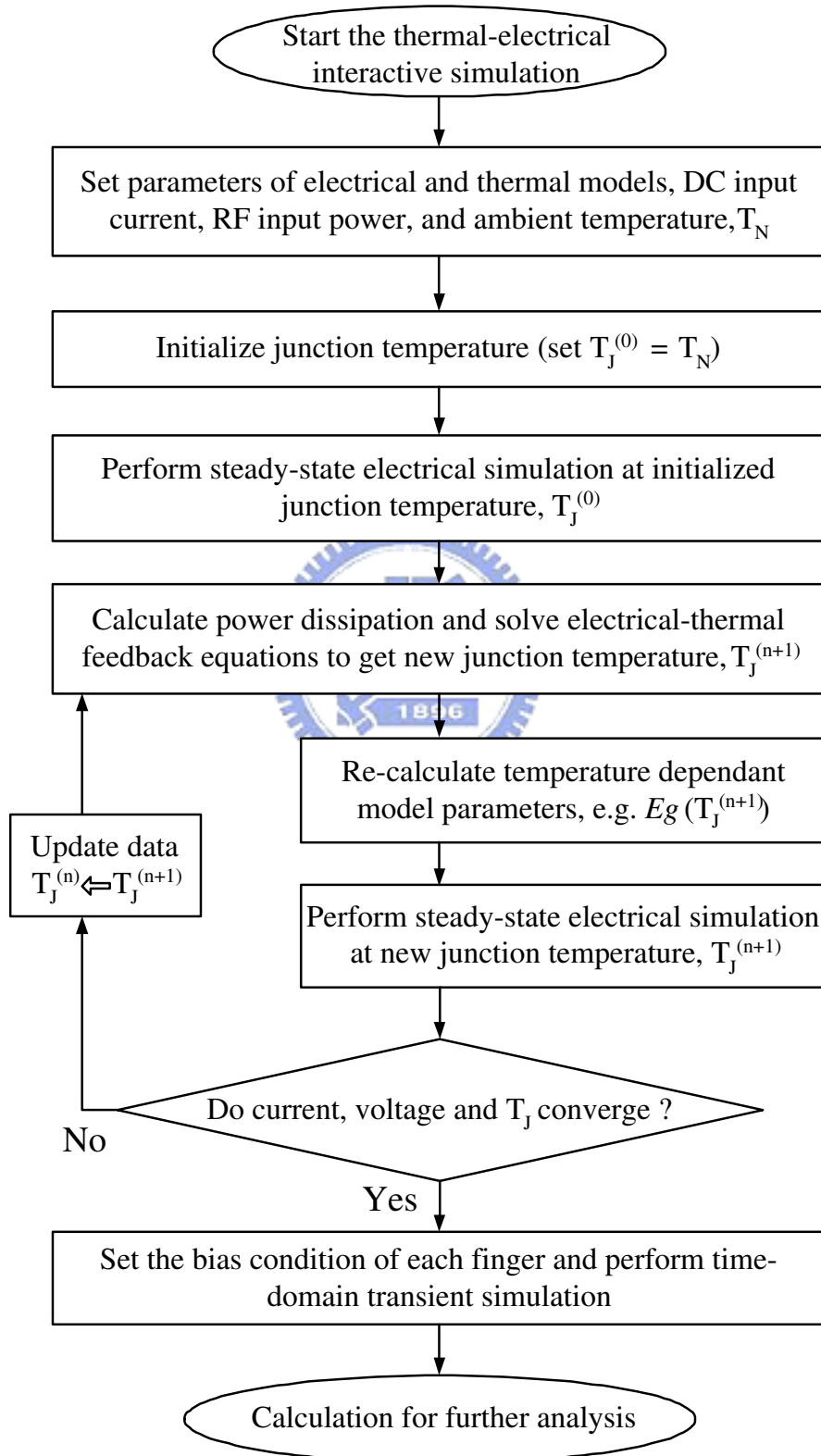


Figure 3.4: A flowchart of the proposed electrical-thermal simulation methodology.

3.2 Genetic Algorithm for Parameter Extraction

For circuit simulation, well extracted model parameters are as important as the device model itself. A rough extraction procedure can lead erroneous simulation results and eventually circuit design failure. According to the conventional extraction method, the parameters are first extracted from the specific measured characteristics. Using numerical curve fitting [20], the model parameters can be estimated so that the calculated outcome will fit the measured data quit well in each parameter's characteristic. However, in practical cases, this set of parameters is not good enough for modelling the whole device behavior, such as family curves. The experienced engineer will spend much time to get a set of useful parameters. Because of the imperfect device model, the engineer should ignore some misfit data and focus on the critical parts of the characteristic. Although we use CAD tools to fit the curves, the fine-tuning of a whole set of parameters still needs to be done semi-manually. This procedure is called *parameter optimization* and is a time-consuming task in microelectronic industry.

To optimize the parameters for the various types and considerable quantities of devices, a robust and automatic technology CAD (TCAD) tool is necessary both in academic research and industry applications. The genetic algorithm (GA) is a global optimal strategy used in a wide rage of applications [64],[85]-[89]. In microelectronics it has been applied to various aspects

in VLSI designs, such as cell placement, channel routing, test pattern generation and design for test. In this work, we applied the GA in model parameters optimization for semiconductor device models. The GA is based on floating-point operators and suitable for solving this numerical optimization problem. In the previous sections, the MI and WR method are proposed and implemented for circuit simulation. Because MI method is fast convergent and highly accurate, we can optimize the parameters efficiently with combining MI method with the GA. In this section, we take the optimization for DC

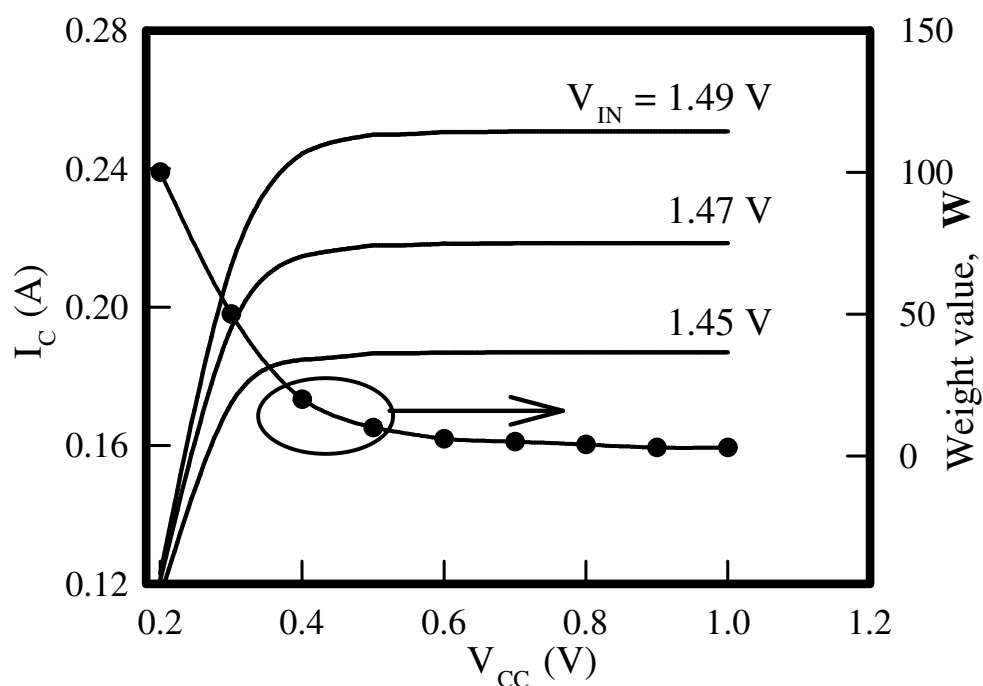


Figure 3.5: The proposed weight value W for HBT model parameter extraction.

family curves as an example. As mention in Sec. 3.1.1, Eq. (3.3)-(3.9) are the governing nonlinear algebraic equations to be solved for the circuit operated at the steady state condition (DC). The current models I_1 , I_2 , I_{BL1} , I_{BL2} , I_{CT} are the functions of V_B , V_C , and V_E , respectively. For a given set of parameters, there is a corresponding set of I-V curves. Table 3.1 shows a part of parameters to be extracted. The parameters resolution and numeric range are also included. The final result is a set of DC I-V curves as shown in Fig. 3.5.

Variable	Range	Resolution	Unit
RB	2.0 ~ 6.0	0.00001	Ω
IS	$1.0e^{-25} \sim 1.0e^{-24}$	$1.0e^{-25}$	A
BR	0.2 ~ 0.3	0.02	—
NR	1.0 ~ 1.1	0.001	—

Table 3.1: A list of parameters to be extracted.

The genetic algorithm is a self-adaptive optimization strategy that mimics a living system. We briefly state the GA method for the HBT circuit optimal characterization.

- **Step 1: Problem Definition.** The relationship between modelling input parameter (V_{CC} and V_{IN}) and simulated result collector current I_C can be written as follows:

$$f(V_{CC}, V_{IN}, \tilde{\mathbf{P}}) = I_C . \quad (3.31)$$

The function f can be regarded as a nonlinear equations

solver, and $\tilde{\mathbf{P}}$ contains all parameters to be extracted. The set of I_C data points represents an I-V curve. The goal of evolution is to minimize the difference between a set of targets and simulated I-V curves, and to find out their corresponding model parameters.

- **Step 2: Encoding Method.** The design of gene encoding strategy depends on the property of problem. In this problem model, there are totally 15 parameters for DC simulation and all variables are floating-point numbers. We transform the floating-point numbers into bit strings instead of real numbers. The bit string has strongly combinatorial property, and we have found this representing has better results in crossover and mutation.
- **Step 3: Fitness function (F) Calculation.** We consider the following function:

$$F = \mathbf{W} * \sqrt{(I_{C_T} - I_{C_S})^2}, \quad (3.32)$$

where the \mathbf{W} is weight value shown in Fig. 3.5. I_{C_T} and I_{C_S} are the sets for target and simulated I-V points, respectively. Because the saturation region of the HBT I-V curve is rather sensitive, we define \mathbf{W} to emphasize the relative importance of each I-V point. It decreases as the applied voltage V_{CC} increases. We evaluate the discrepancy for two I-V sets with

the F .

- **Step 4: Reproduction.** We adopt the *tournament selection* with floating-point operators as the selection strategy and this hybrid strategy not only selects better chromosomes but also keeps weak ones for few generations to achieve higher population diversity. For the crossover scheme, in HBT device model, all parameters to be optimized can be classified into four categories which represent different numerical constraints. We take an uniform crossover scheme [85, 86, 90]; and based on our simulation experience, it is more effective than single and two-point crossover schemes. Finally, the mutation strategy changes the mutation rate dynamically to keep the population diversity.

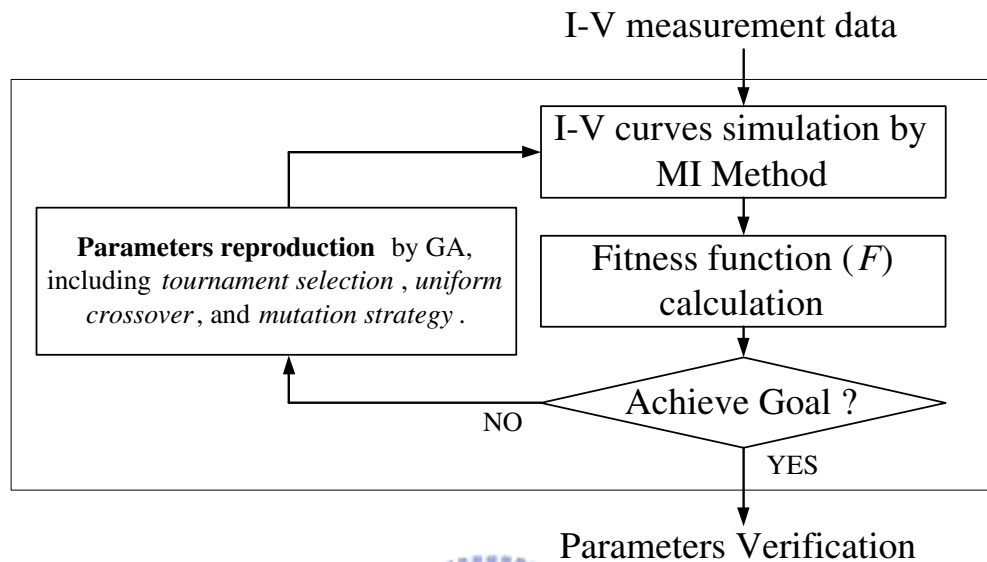
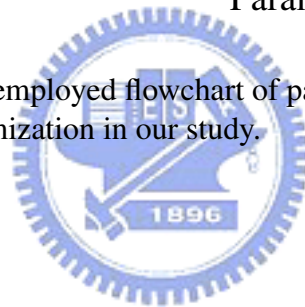


Figure 3.6: The employed flowchart of parameters optimization in our study.



The illustration of above steps are plotted in flowchart, Fig. 3.6. We should simulate all data points with respect to the measured data. The numerical efficiency of our circuit simulator can reduce the consumed time for GA parameter extraction. In Fig. 3.6, we note that the extracted parameters should be verified by physical checks after GA procedure. It is because that we can achieve the evolution goal by more than one set of parameters. Figure 3.7 shows the comparison between multiple I-V curves evolution with and without the weight value after 300 generations. The evolutionary I-V curves with applying weight value achieve the target I-V curves rapidly, and it has a good evolution behavior. The importance of weight value introduced here not only

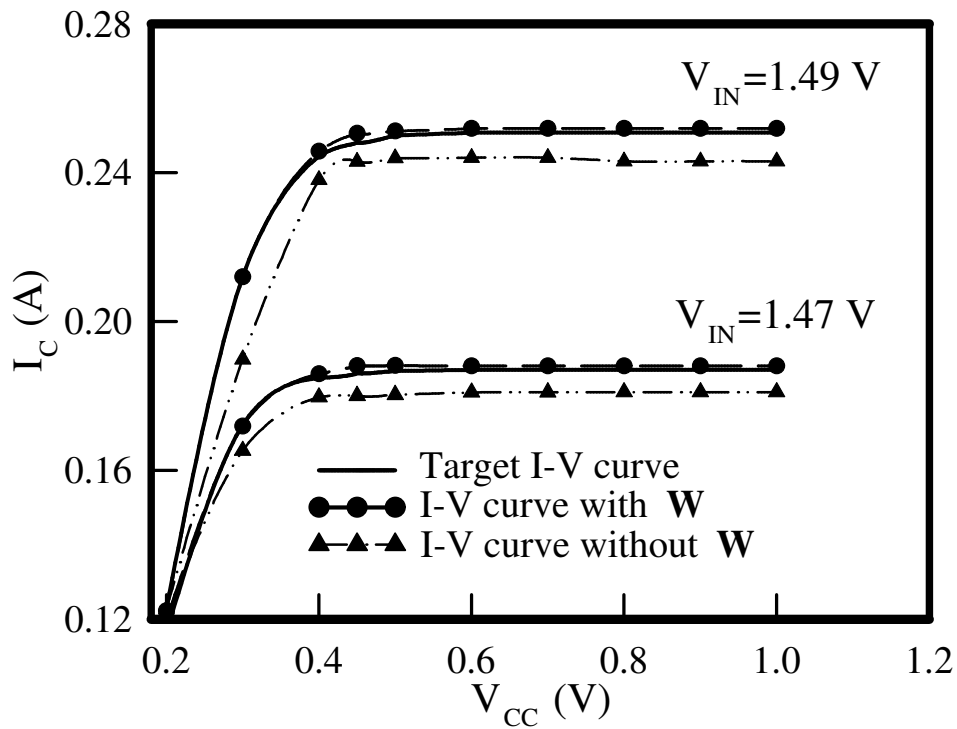


Figure 3.7: A comparison of the method with and without the proposed weight value for multiple I-V curves optimization.

redirects the evolution trend to better direction but also reduces the searching space in this multiple objective evolution problem, and the efficiency can be obtained.

In addition, Fig. 3.8 shows the fitness score convergence behavior for the multiple I-V curves evolution with or without the dynamic mutation technique.

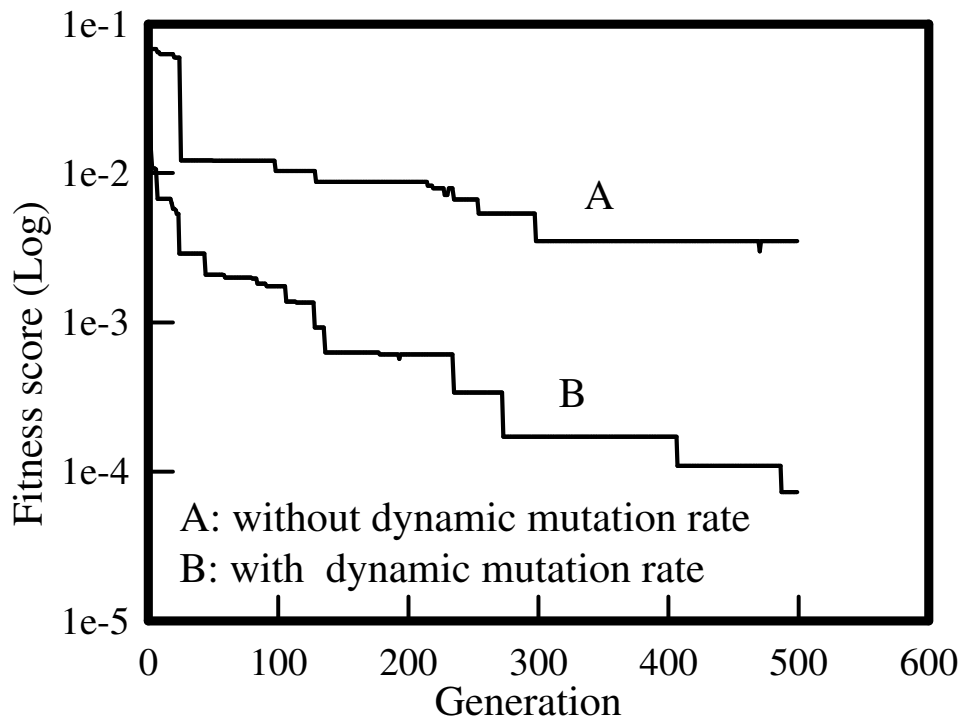


Figure 3.8: A comparison of the method with and without the proposed dynamic mutation rate scheme.

The results suggest that the dynamic mutation scheme with floating-point operators keeps the population diversity and finally has better evolutionary results.

Figure 3.9 shows the evolutions of the I-V curve. Starting from an arbitrary I-V curves, it approaches to the desired final I-V curve step by step. Based on the MI and GA methods, the above process, from a given I-V curve to the final optimal I-V curve, is solved and evolved automatically. Compared with

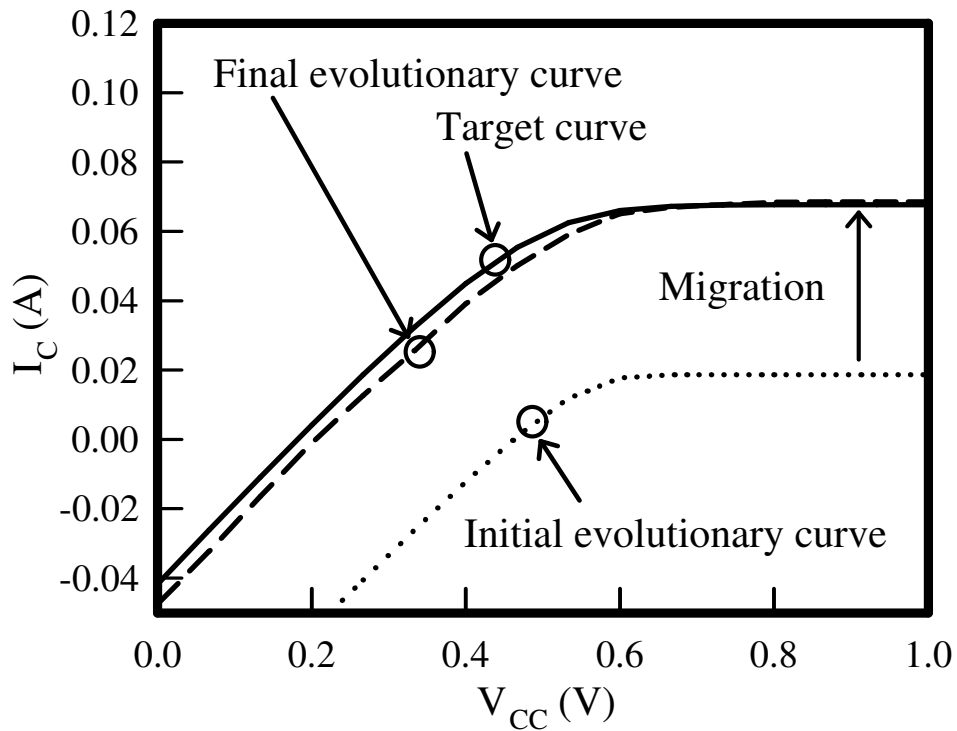


Figure 3.9: An illustration of the migration processes for the I-V curve optimization.

the conventional trial-and-error methodology to extract optimal parameters of the circuit model, our approach successfully reduces the complex procedures and simulation time significantly.

3.3 Further Analysis of Time-Domain Results

In this section, we describe the steps of further analysis for time-domain data. In order to perform intermodulation distortion analysis, the Fourier transform for discrete sampled data and proper calculation for the third order intermodulation (IM3) products is necessary.

3.3.1 Transformation of the Time-Domain Data into Frequency-Domain

With the time domain results, we can extract the intensity of amplitude or power at a specified frequency from the discrete data. We use the discrete Fourier transform (DFT) to transfer the time domain results into the frequency domain [20, 21]. For a function $g(t)$ is sampled. Suppose we have N consecutive sampled values. Let Δt denote the time interval between two samples, so that the sequence of sampled values is

$$g_k \equiv g(k \cdot \Delta t), \quad (3.33)$$

where $k = 0, 1, 2, \dots, N - 1$. For any Δt , there is a special frequency f_{NC} , named *Nyquist critical frequency*

$$f_{NC} \equiv \frac{1}{2\Delta t}. \quad (3.34)$$

If the function $g(t)$, sampled at Δt , happens to be bandwidth limited to frequencies lower than f_{NC} , then $g(t)$ is completely determined by its samples

g_k . It is called *Nyquist criterion* for sampling theorem. The sampling interval should meet this criterion or else the aliased Fourier transform will be caused. With N numbers of input, we can estimate the Fourier transform $G(f)$ at the discrete value

$$f_n \equiv \frac{n}{N \cdot \Delta t}, \quad (3.35)$$

where $n \equiv -\frac{N}{2}, \dots, \frac{N}{2}$. Then, we approximate the integral of Fourier transform by a discrete sum,

$$G(f_n) = \int_{-\infty}^{\infty} g(t) e^{2\pi i f_n t} dt \approx \sum_{k=0}^{N-1} g_k e^{2\pi i f_n t_k} \cdot \Delta t = \Delta t \sum_{k=0}^{N-1} g_k e^{2\pi i k \frac{n}{N}}. \quad (3.36)$$

The final summation in equation (3.36) is called the discrete Fourier transform of the N points g_k . Let us denote it by G_n .

$$G_n \equiv \sum_{k=0}^{N-1} g_k e^{2\pi i k \frac{n}{N}}. \quad (3.37)$$

Fig. 3.10 illustrates the DFT for a given time-domain data. The remaining work for the application to the intermodulation distortion analysis is to determine the resolution in frequency-domain. For a system with two-tone excitation, in which fundamental frequencies are denoted by f_1 and f_2 , the resolution, i.e., the frequency interval,

$$\Delta f_n = \frac{f_n}{n} = \frac{1}{N \Delta t}, \quad (3.38)$$

must be equal to or smaller than a half of the spacing between f_1 and f_2 , $\frac{\Delta f}{2}$, in magnitude. For given the central frequency $f_c = \frac{f_1 + f_2}{2} = \frac{1}{\Delta t_c}$, the total

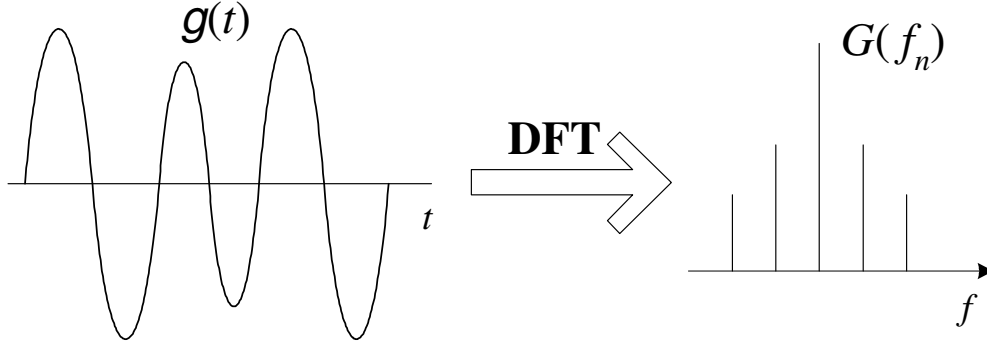


Figure 3.10: An illustration of discrete Fourier transformation for a given input time domain data.

interval T for the time-domain data can be presented by

$$T = N\Delta t \equiv N_c\Delta t_c = \frac{N_c}{f_c}. \quad (3.39)$$

Where, t_c is the notation of time interval for a input signal cycle at frequency f_c and N_c is the total number of cycles in the interval T . Assume that Δf is equal to $\frac{f_c}{M}$, then combine this assumption with equations (3.38) and (3.39).

The requirement for frequency interval becomes

$$\Delta f_n = \frac{f_c}{N_c} \leq \frac{\Delta f}{2} = \frac{f_c}{2M}. \quad (3.40)$$

So we should perform time-domain simulation for $N_c \geq 2M$ input excitation cycles to meet the resolution requirement of intermodulation distortion analysis (i.e. $T = N_c\Delta t_c \geq \frac{2M}{f_c}$). In this work, f_c and Δf is set to be 1.8 GHz and 180 MHz, therefore $M = 10$. The total time interval of time-domain simulation should be at least 20 input cycles ($T \geq \frac{20}{1.8\text{GHz}} = 11.11\text{ns}$). There is an advanced method, called fast Fourier transform (FFT), and the calculation time

for transformation can be reduced with this method. The commercial numerical software METLAB has internal function `fft()` for FFT algorithm [91].



3.3.2 Calculation of Intermodulation Distortion Analysis

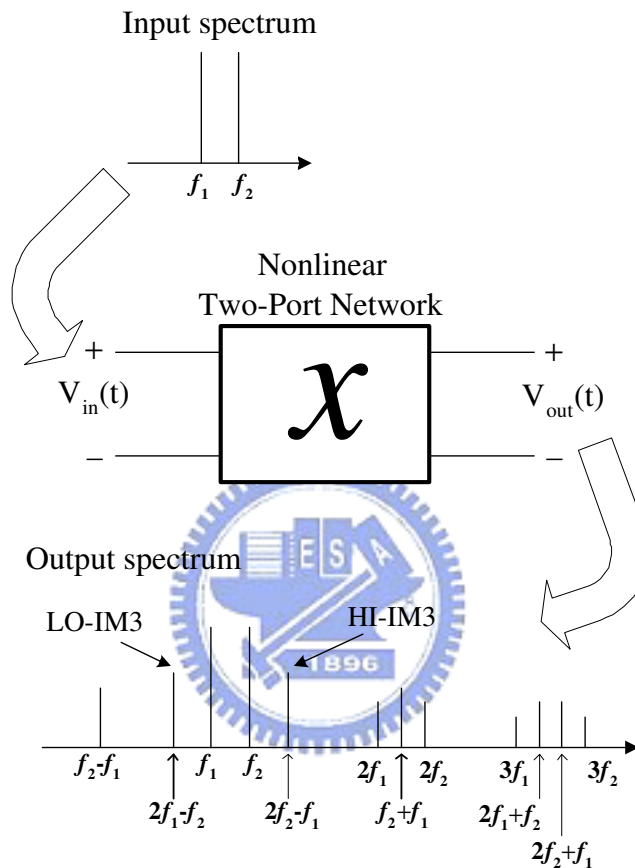


Figure 3.11: An illustration of two-tone intermodulation characteristics for a nonlinear two-port network.

When a two-tone input signal V_{in} is applied to a nonlinear two-port network and shown as

$$V_{in}(t) = V_m \sin(\omega_1 t) + V_m \sin(\omega_2 t), \quad (3.41)$$

where, V_m is the amplitude and $\omega_1 = 2\pi f_1$ and $\omega_2 = 2\pi f_2$ are the fundamental

frequencies. The output signal can be represented by the power series,

$$V_{out} = a_1 V_{in}(t) + a_2 (V_{in}(t))^2 + a_3 (V_{in}(t))^3. \quad (3.42)$$

Fig. 3.11 shows the input and output spectrum characteristic of a nonlinear two-port network. We mark the third order intermodulation (IM3) products in this figure. The IM3 products play an important role for the intermodulation

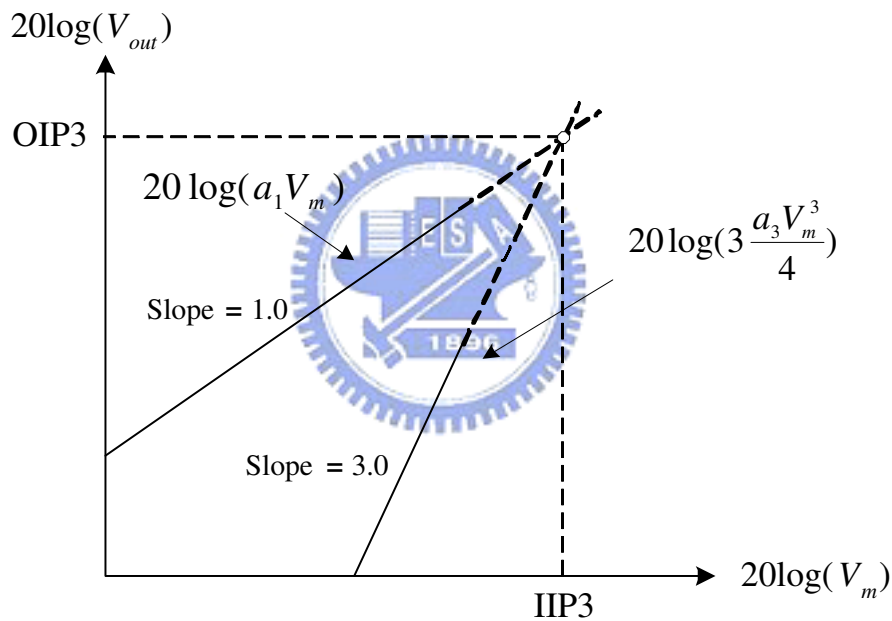
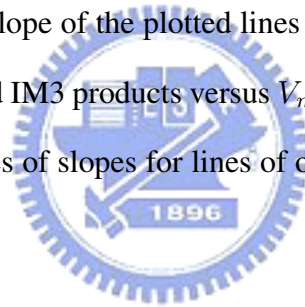


Figure 3.12: The ideal output amplitudes at fundamental frequencies and the IM3 products versus the input amplitudes.

linearity of semiconductor devices. From Eq. (3.41) and Eq. (3.42), we note the output amplitudes at fundamental frequencies and IM3 products are $a_1 V_m$ and $\frac{3}{4} a_3 V_m^3$. The value of the output third-order intercept point (OIP3) is the

projection of the cross point of these two extrapolated lines on output axis and the value of input third-order intercept point (IIP3) is the projection on input axis. It is an important benchmark to evaluate the linearity of the devices at frequency modulation [92]-[98]. The value of OIP3 depends on the device material and the design of the device structure. In general, the higher OIP3 value represents the better linearity of the two-tone intermodulation characteristics.

Figure 3.12 shows the theoretical curves of the output amplitudes at fundamental frequencies and the IM3 products versus the input power. Derive from Eq. (3.42), we have the slope of the plotted lines of output amplitudes at fundamental frequencies and IM3 products versus V_m equal 1 and 3, respectively. And the theoretical values of slopes for lines of output power are the same in log scale.



3.4 Measurement for Intermodulation Distortion

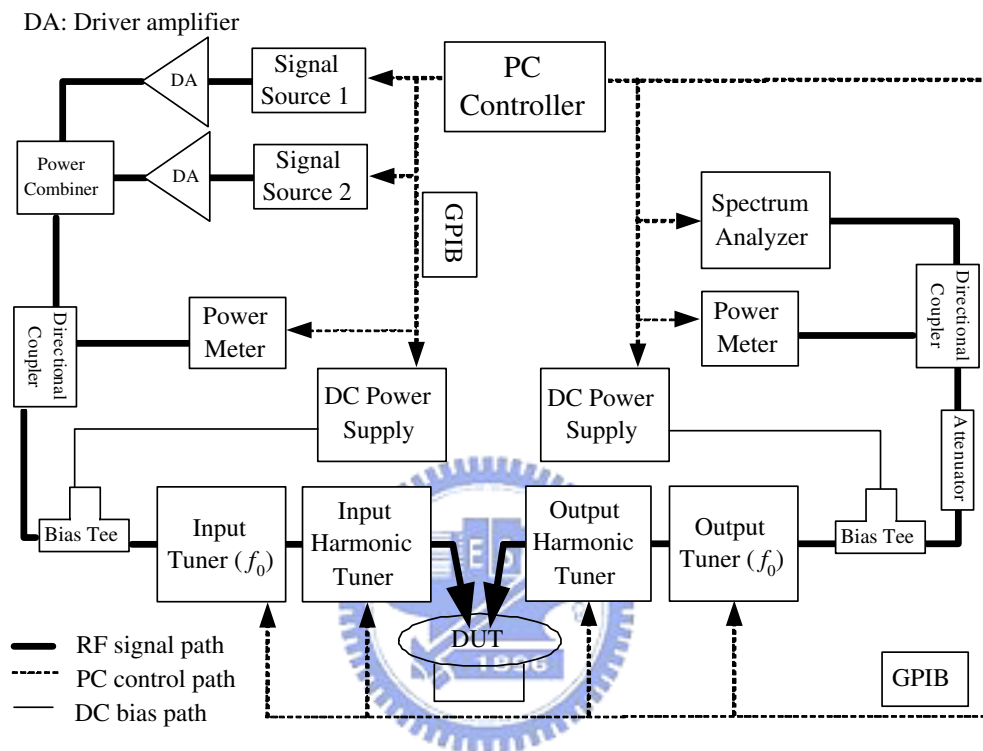


Figure 3.13: A setup of on-wafer device testing with harmonic load-pull system.

The intermodulation distortion measurement in this work is accomplished by the harmonic load-pull system. The equipment setup for on-wafer testing is shown in Fig. 3.13. The load-pull measurement is useful for power characterization of the large-signal operated, nonlinear devices [52],[99]-[102]. The load-pull system has two sets of tuners, which are input tuners for the "source pulling" and output tuners for the "load pulling". In order to measure a device-under-test (DUT) in actual operating conditions. The calibration

for measuring the available input power at the power source reference plane and the coupling value of the directional coupler should be done before output power and gain measurement. With considering the dissipative loss of all tuners (and probes in on-wafer measurement) and reflected power at the source, one can get the power and gain values at the DUT reference planes. Once we can get the real power and gain, the DUT will be measured under different source and load impedance. Based on above measurement data, the contours for source pull and load pull can be plotted. The source pull contours are measured and calculated in the same way of the load pull contours. In our measurement, we choose the max gain matching for source impedance and the max power matching for load impedance from the contours. After calibrating and optimum impedance matching, we can perform measurement for the output power with variant input power. The power of the third order intermodulation products (IM3) is detected by the spectrum analyzer as shown in Fig. 3.13. Finally, "one" OIP3 value can be calculated by the values of output power at fundamental frequencies and IM3 products. Unfortunately, once the bias condition is changed, the matching condition should be tuned again because of the device nonlinearity. There is one more thing that should be noticed in the measurement, the DUT oscillation. Once the DUT begins to oscillate, power gain becomes almost meaningless. These oscillation is usually caused by high level bias and RF input signal excitation with poor source

matching. For a HBT device with high voltage base bias, the oscillation happens easily and can bring second breakdown in our experience. The measurement for RF characteristics should be done with carefulness and passion, so that the measured data could be useful to the research.

3.5 Summary of This Chapter

In this chapter, we stated all numerical algorithms and computation techniques used in this study. Besides, the measurement procedure was also described simply in the last section. Here, we summarize this chapter as:

- algorithms for solving the system algebraic equations (DC node equations).
- large-signal time-domain solution algorithm with WR, MI, and RK methods.
- algorithm with electrical-thermal feedback,
- GA for parameter extraction and optimization,
- discrete Fourier transform,
- calculation for intermodulation distortion analysis, and
- measurement for intermodulation distortion.

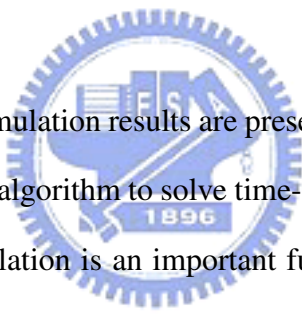
With utilization of above numerical methods and measurement skill, we can perform our simulation and compare our results with measured data in the following chapters.

Additionally, we present the convergent characteristics of the algorithms mentioned above in Appendix C. These convergence properties can further illustrate the efficiency of the numerical methods used in this study.



Chapter 4

DC Simulation and Analysis



In this chapter, DC simulation results are presented and discussed. For our proposed simulation algorithm to solve time-domain large signal circuits, the accuracy of DC simulation is an important fundamental. By solving the node equations without time dependency, we can get the DC solutions of the circuit as the initial conditions for the time domain simulation. Therefore, DC simulation results are discussed in this chapter before others of our work. An InGaP hetero-junction bipolar transistor (HBT) device with no thermal effect is simulated and measured in the first section of this chapter. Comparison between the results of measurement and HSPICE simulation shows the proposed method has a very good accuracy. Next, we demonstrate the simulation answers for DC I-V curves of an HBT with self-heating effect. In the third section, we calculate the junction temperatures, collector currents and collector current density of a multi-finger HBT device. The effects of self-heating

and thermal coupling among fingers have been considered for those simulation results as shown in this section. Lastly, we summarize the contents of this chapter.



4.1 DC Simulation

Notation	Value	Unit	Notation	Value	Unit
IS	2.85E-24	A	VJE	1.367	V
BF	86.59	-	MJE	0.1188	-
NF	1.068	-	CJEO	130.0E-15	F
IKF	0.1815	A	XTF	275.6	-
IKR	1.032E-3	A	VTF	66.0	V
ISE	2.34E-18	A	CJCO	24.27E-15	F
NE	1.91	-	VJC	0.7161	V
BR	1.47	-	MJC	0.266	-
NR	1.06	-	XCJC	0.3428	-
ISC	2.142E-14	A	TR	350.0E-12	Sec
NC	1.954	-	TF	2.680E-12	Sec
RB	48.13	Ω	ITF	419.80E-3	A
RE	1.256	Ω	FC	0.5	-
RC	6.75	Ω	M	104	-

Table 4.1: A set of extracted parameters for Gummel-Poon model used in this study.

An NPN InGaP HBT device is fabricated and measured in this work. The schematic cross section of this HBT structure is shown in Fig. 4.1 [103]. The epitaxial wafer of this HBT is grown by metal-organic vapor deposition (MOCVD). The main epitaxial structure consists of:

- an emitter cap for ohmic contact, including: an $\text{In}_{0.6}\text{Ga}_{0.4}\text{As}$ layer (500-Å, $n^+ > 10^{19} \text{ cm}^{-3}$), a gradient layer from $\text{In}_{0.6}\text{Ga}_{0.4}\text{As}$ to GaAs (500-Å, $n^+ > 10^{19} \text{ cm}^{-3}$), and a GaAs layer (1200-Å, $n^+ = 4 \times 10^{18} \text{ cm}^{-3}$),
- an $\text{In}_{0.49}\text{Ga}_{0.51}\text{P}$ (400-Å) emitter with silicon-dopant ($3 \times 10^{17} \text{ cm}^{-3}$),

- a GaAs (1200-Å) base with carbon-dopant ($4 \times 10^{19} \text{ cm}^{-3}$),
- a GaAs (1- μm) collector with silicon-dopant ($3 \times 10^{16} \text{ cm}^{-3}$), and
- a GaAs (5500-Å) sub-collector with silicon-dopant ($5 \times 10^{18} \text{ cm}^{-3}$).

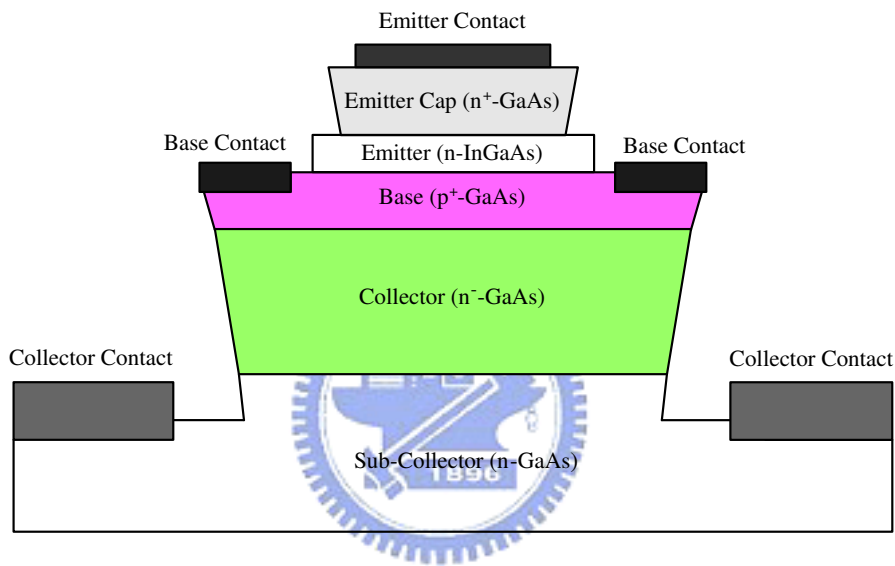


Figure 4.1: A cross section view of an InGaP HBT.

We simulate this HBT as a one-finger device without the consideration for any thermal effects. Figure 4.2 shows the simulation circuit of $I_C - V_{BE}$ and $I_B - V_{BE}$ curves. Where, I_C , I_B , and V_{BE} represent the collector current, base current, and base-emitter voltage, respectively. The value of parameters used for the simulated device are listed in Table 4.1.

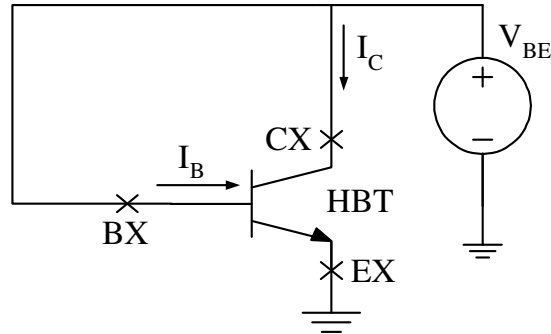


Figure 4.2: The used circuit in the simulation of $I_C - V_{BE}$ and $I_B - V_{BE}$ curves.

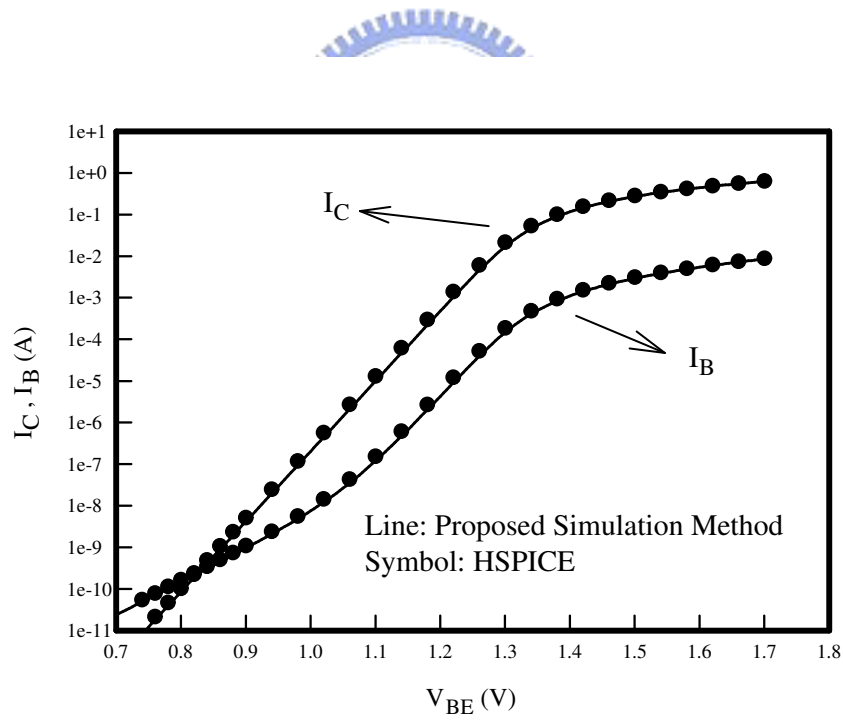


Figure 4.3: Comparison of Gummel plot between the simulated results of HSPICE and our proposed method with the same device parameters.

Here, we should note that the multiplier factor M is set to be 104. Which means we treat 104 fingers as 104 identical isolated one-finger devices; and their homologous terminals are shunted together in this simulation case.

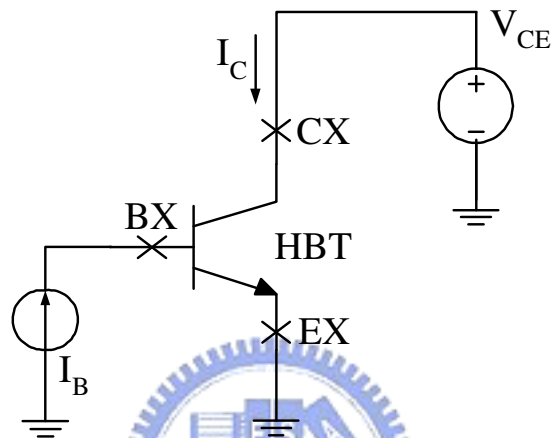


Figure 4.4: The used circuit in the simulation and measurement of I_C - V_{CE} DC curves.

As shown in Fig. 4.3, which is named Gummel Plot, the comparison has been done between simulated results by feeding the benchmark parameters and biases into our and HSPICE simulator. Both of them have consistency in the DC conditions.

In the following, Fig. 4.4 shows the circuit for the family curves of this HBT. V_{CE} denotes the collector-emitter voltage. The calculated results by our simulator as shown in Fig. 4.5 are quite in agreement with the measurement data under different input base current, I_B .

In the simulation for a one-finger NPN HBT device, the results of our simulator can stand comparison with those of HSPICE simulator. With a proper set of parameters, our results can also meet the DC measurement data well. From above reasons, our DC simulation will provide accurate initial conditions for solving time-domain circuits.

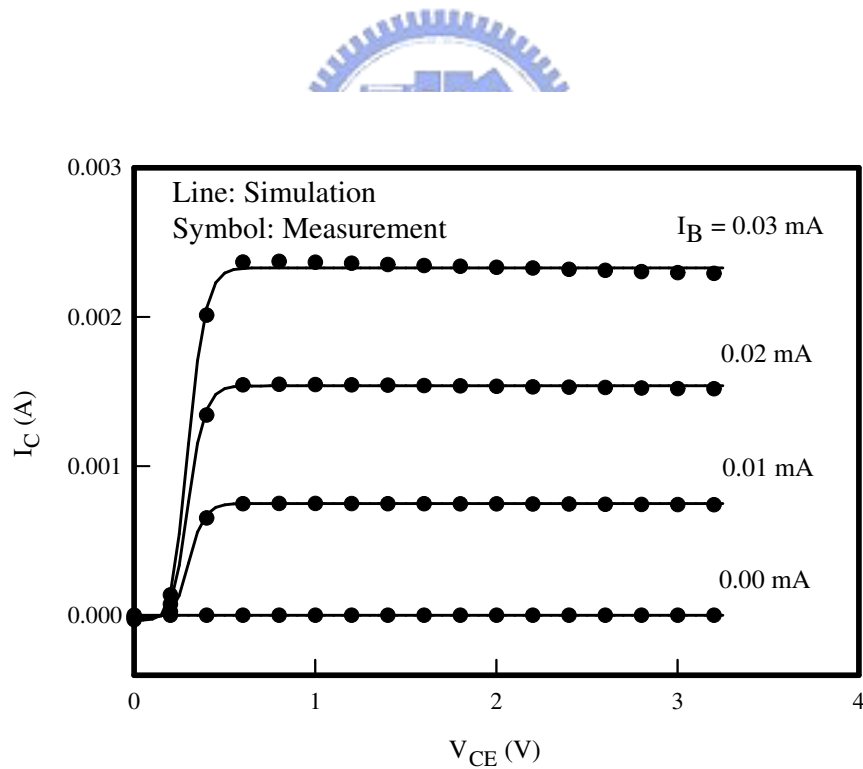


Figure 4.5: Comparison between our simulated results and measured results for I_C-V_{CE} curves of the InGaP HBT.

4.2 Self-Heating Effect

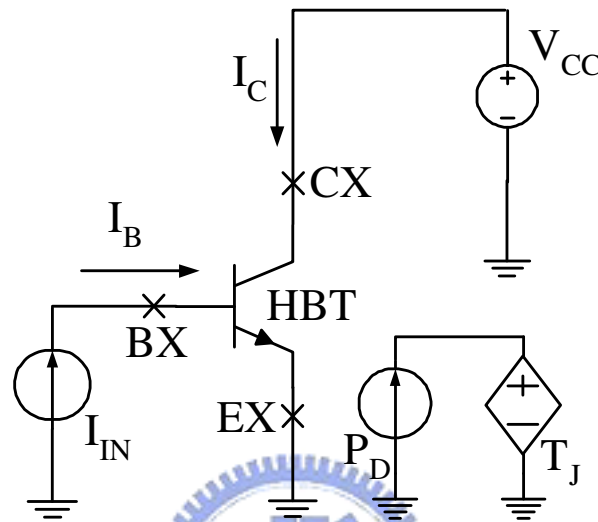


Figure 4.6: An equivalent circuit including thermal network of an HBT for DC simulation.

By introducing equations (2.20)-(2.27), the self-heating effect for an NPN HBT can be simulated by the developed solver. These equations are also formed in the HSPICE .ps file in order to compare with our solver. It is unlike our solver that we need manually force the HSPICE to do the global iteration loop among thermal and electrical equations for 20 times in this case (see also Fig. C.6). The circuit for DC simulation with thermal network are shown in Fig. 4.6. For the one-finger device, Eq. (2.26) is expressed as

$$T_J = T_N \left\{ 1 - \frac{(BB - 1)}{T_N} [P_D \cdot R_{TH}] \right\}^{\frac{-1}{BB-1}}. \quad (4.1)$$

The parameters used for the simulation in this section are written in Table 4.2.

Those parameters for time-domain and thermal simulation are also included in this table.

Notation	Value	Unit	Notation	Value	Unit
IS	2.85E-24	A	VJE	1.367	V
BF	86.59	-	ITF	419.80E-3	A
NF	1.068	-	TF	2.680E-12	Sec
IKF	0.1815	A	XTF	275.6	-
IKR	1.032E-3	A	VTF	66.0	V
ISE	2.34E-18	A	CJCO	24.27E-15	F
NE	1.91	-	VJC	0.7161	V
BR	1.47	-	MJC	0.266	-
NR	1.06	-	XCJC	0.3428	-
ISC	2.142E-14	A	TR	350.0E-12	Sec
NC	1.954	-	FC	0.5	-
RB	56.88	Ω	E _a	5.405E-4	eV/K
RE	10.256	Ω	E _b	204	K
RC	6.75	Ω	BB	1.22	-
CJEO	130.0E-15	Ω	XTI	3.0	-
MJE	0.1188	-	XTB	-2.0	-

Table 4.2: A set of extracted parameters for the GP electrical and thermal models.

In Eq. (4.1), R_{TH} is equal to $1834.20 \text{ }^\circ\text{C/W}$ for an HBT with $2.8 \times 12 \text{ } \mu\text{m}^2$ emitter area size. We also set the multiplier factor M to 3, which means there are three identical thermal isolated HBTs parallel connected in the simulation. Additionally, the thermal coupling among HBTs is not taken into consideration in this section.

The result of DC simulation is shown in Fig. 4.7. The data of our solver

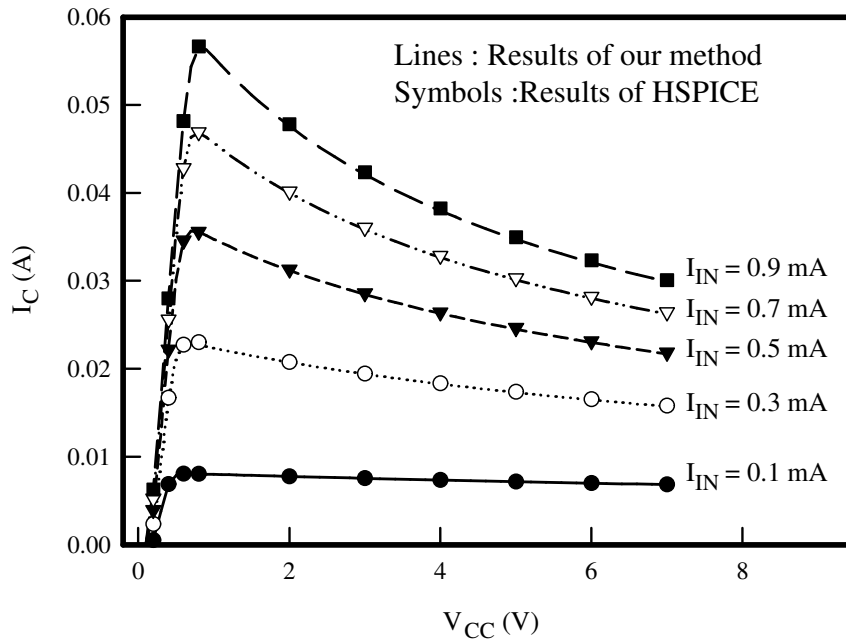


Figure 4.7: Comparison between our and HSPICE's simulated results for common-emitter $I_C - V_{CC}$ characteristics of the HBT with self-heating effect.

has great agreement with the data calculated by HSPICE solver. The collector current I_C decreases gradually as collector-emitter voltage V_{CC} increases. This situation results a negative differential resistance (NDR) region in common-emitter I-V characteristic and becomes negative feedback as I_{IN} increases. This degradation of I_C is caused by the increase of back injection current, because of the energy barrier lowering at high junction temperature. The NDR region happens only if the input bias is current source. It causes degradation, which is reversible as input current decreases again. On the other hand, when

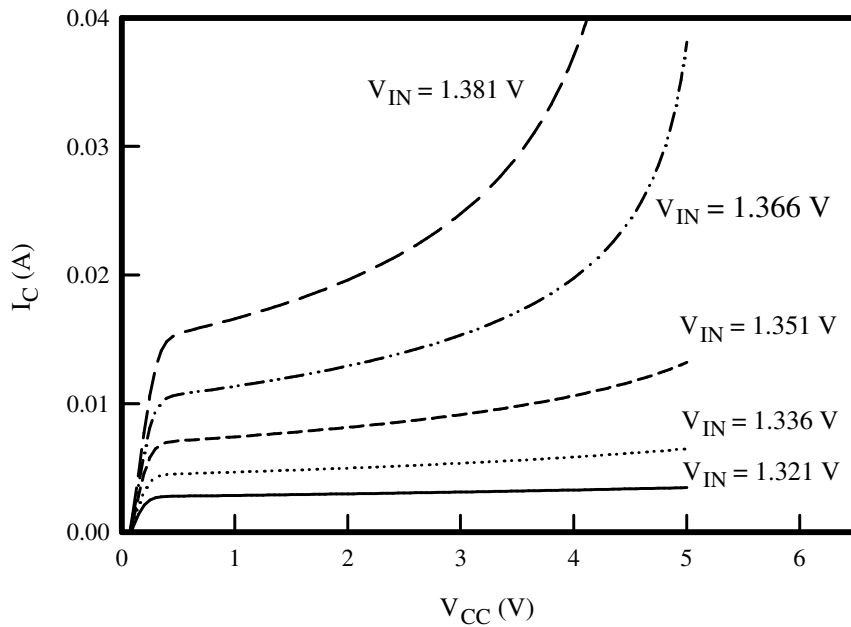


Figure 4.8: The $I_C - V_{CC}$ characteristics with voltage source V_{IN} .

the voltage source V_{IN} is being substituted for I_{IN} in Fig. 4.6, the I-V characteristic becomes different as shown in Fig. 4.8. Contrary to curves with input current source, there is no NDR region in Fig. 4.8. The extreme high collector current happens at high base-emitter input voltage. With high voltage and current operation, the device will encounter second breakdown and be irreversibly damaged. In the operation of common-emitter, even for the HBTs, one should carefully control the voltage input source to prevent the device from the second breakdown.

4.3 Thermal Effects of Multi-Finger Device

A multi-finger HBT can be viewed several sub-HBTs connected in parallel, with their respective collector, emitter and base leads connected together. The DC equivalent circuit with thermal network of an n -finger HBT can be drawn as Fig. 4.9. It is possible for all identical n fingers to have different bias

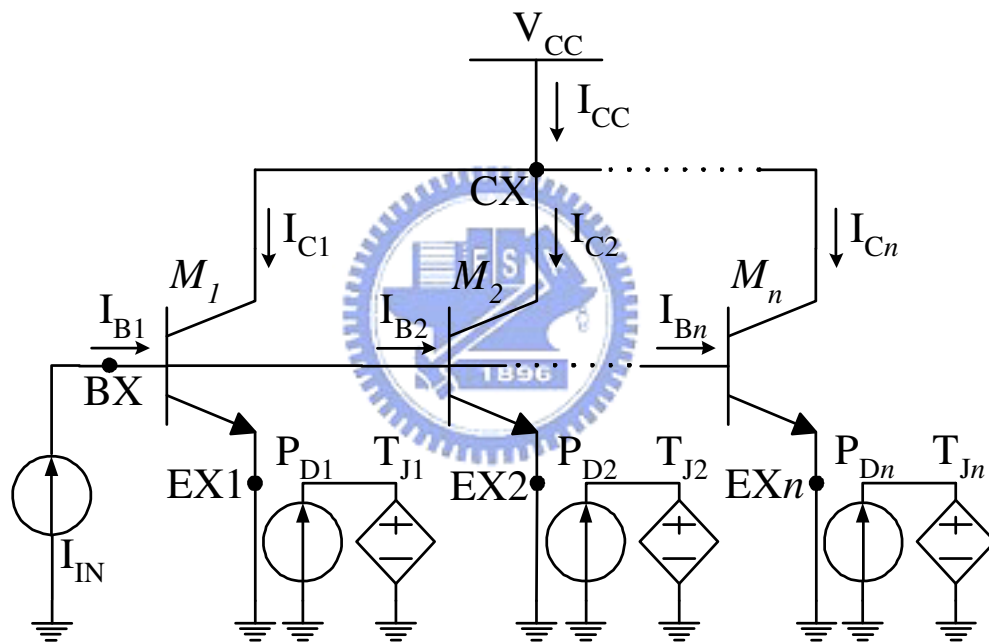


Figure 4.9: An equivalent circuit including thermal networks of an n -finger HBT with constant current bias.

condition, due to the significance of the coupled electrical-thermal feedback. Therefore, this will influence the DC and RF characteristics of each finger and the whole multi-finger transistor, in particular for devices under high current or high power operation. With electrical-thermal iteration been discussed

in section 3.1.4, our approach can explore the collapse phenomenon of the multi-finger HBT under high voltage and current bias. To clearly examine the nonlinearity, we perform the simulation for a three-finger HBT, i.e. $n = 3$. Without loss of generality, each finger is theoretically assumed identical. The model parameters of each finger for both the electrical and thermal models are shown in Table 4.2. Besides, the multiplier factor M of each distinct finger is set to be 1.0.

Finger 1, Finger 2 and Finger 3 of this three-finger HBT are represented by $M1$, $M2$ and $M3$, respectively. I_{CC} and I_{IN} denote the total collector current of the device and DC base input current in Fig. 4.9. The behavior of those two side fingers, Finger 1 and Finger 3, are the same for the identical finger assumption. According to the case of three-finger transistor, the junction temperature of outside finger, T_{J1} and central finger, T_{J2} can be derive from equations (2.26) and (2.27) and is shown as follows:

$$T_{J1} = T_{J3} = T_N \left\{ 1 - \frac{(\mathbf{BB} - 1)}{T_N} [\mathbf{P}_{D1} \cdot (R_{TH0} + R_{TC2}) + \mathbf{P}_{D2} \cdot R_{TC1}] \right\}^{\frac{-1}{\mathbf{BB}-1}}, \quad (4.2)$$

and

$$T_{J2} = T_N \left\{ 1 - \frac{(\mathbf{BB} - 1)}{T_N} [\mathbf{P}_{D1} \cdot (2 \cdot R_{TC1}) + \mathbf{P}_{D2} \cdot R_{TH0}] \right\}^{\frac{-1}{\mathbf{BB}-1}}. \quad (4.3)$$

In above equations, $R_{TH0} = R_{T11} = R_{T22} = R_{T33}$, $R_{TC1} = R_{T12} = R_{T21}$, and , see also Eq. (2.27). The emitter area of each finger is equal to $2.8 \times 12 \mu m^2$ and the substrate thickness is $100 \mu m$. There is the same spacing between Finger 1 and Finger 2, and between Finger 2 and Finger 3, which is $14.4 \mu m$.

Therefore, the theoretical values of R_{TH0} , R_{TC1} and R_{TC2} are 1834.20, 487.04 and 101.43 °C/W, respectively [52, 65, 66, 67, 72]. Furthermore, T_N is set to be ambient temperature, 300 K and the energy band gap of GaAs at this temperature, $E_g(T_N)$, equals 1.424 eV.



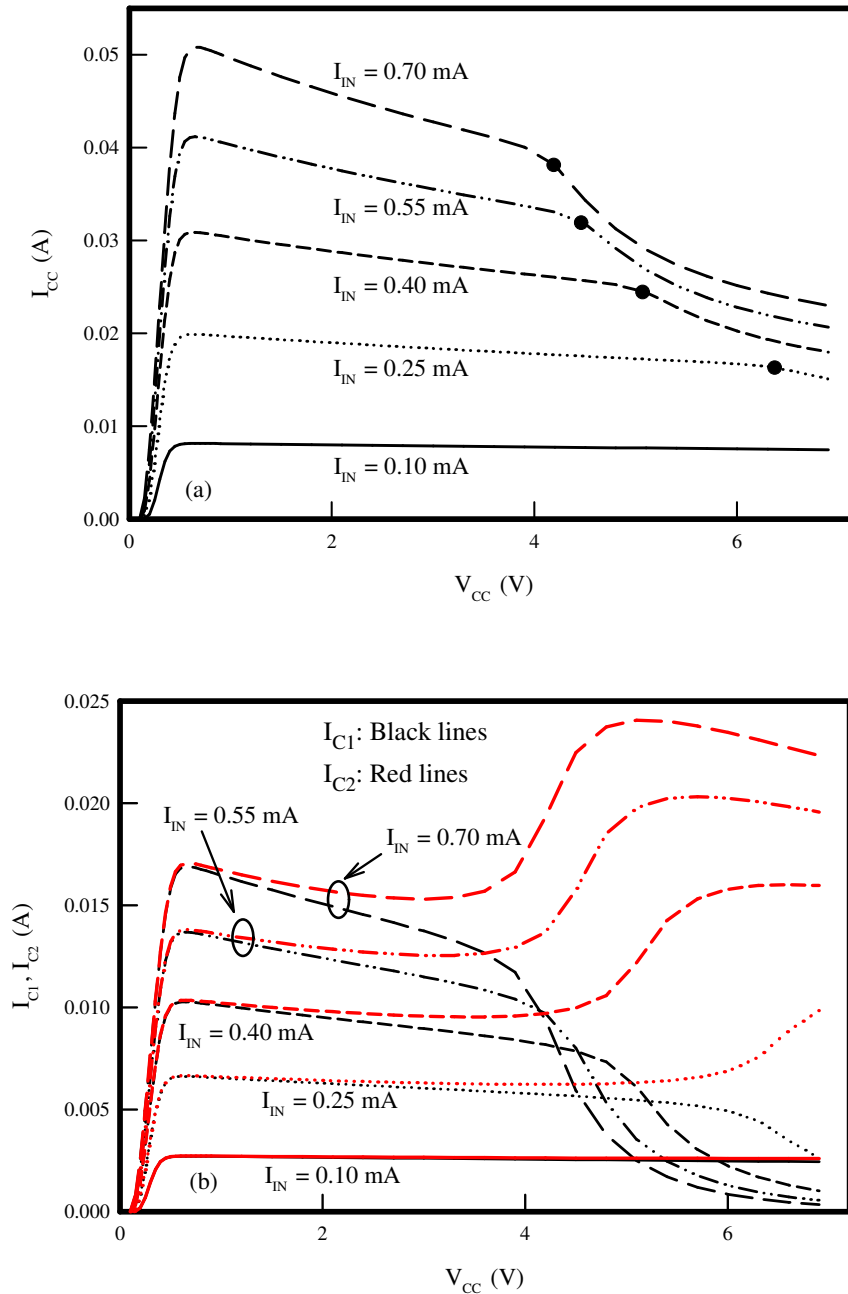


Figure 4.10: The common-emitter I-V characteristics: (a) I_{CC} versus V_{CC} (b) and I_{C1} and I_{C2} versus V_{CC} of the three-finger HBT with thermal effects being considered.

The simulated common-emitter I-V curves for this three-finger HBT is demonstrated in Fig. 4.10. Each line in Fig. 4.10 (a) represents the total collector current under the bias of a constant input current, I_{IN} . As collector-emitter voltage V_{CC} is less than 4.0 V, the NDR region could also be observed in the low and moderate bias region. When V_{CC} increases even more (> 4.0 V), an abrupt lowering of I_{CC} occurs. The dots in Fig. 4.10 mark the break points between the collapse (abrupt lowering) and NDR region. These marks collectively form the collapse loci. The collector currents of Finger 1 (I_{C1}) and Finger 2 (I_{C2}) are plotted as black and red lines in Fig. 4.10 (b) to explain the collapse in detail. I_{C1} and I_{C2} with the same I_{IN} are denoted by lines with the same styles, and they begin to split when collector-emitter voltage V_{CC} increases. As V_{CC} raises, the central finger (Finger 2) becomes slightly warmer than the others, then its base-emitter junction turn-on voltage becomes slightly lower (see also Fig. 4.11 and Fig. 4.12). Consequently, Finger 2 conducts more current for a given fixed base input current. This increased collector current, in turn, increases the power dissipation in the junction. From Eq. (4.3), the increased dissipated power raises the junction temperature even further. Collapse occurs when the junction temperature at Finger 2, T_{J2} , becomes much higher than those at the side fingers. So that the feedback action of increased collector current with junction temperature quickly leads to a situation that just the central finger conducts the almost entire current of this device. Though I_{C2} raises, the whole device drains less current for the current degradation of side fingers. Since the transition from near even current conduction to one

finger domination occurs suddenly, an dramatic current gain lowering due to the lowered emitter injection efficiency at high temperatures can be observed. Conclusively, the fundamental reason of both NDR and collapse is the current gain drop with increasing temperature.

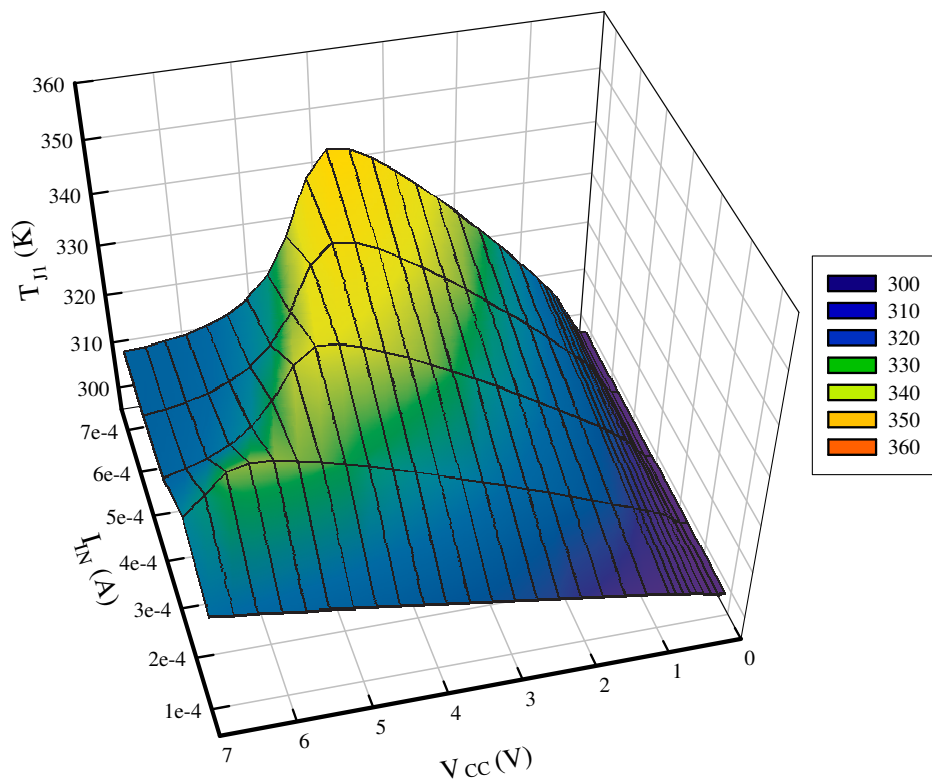


Figure 4.11: T_{J1} with respect to V_{CC} and I_{IN} .

Furthermore, the changes of junction temperature is shown in Fig. 4.11 and Fig. 4.12. In the comparison between T_{J1} and T_{J2} , we can observe the concentrated heat at the central finger, which induces the current gain collapse.

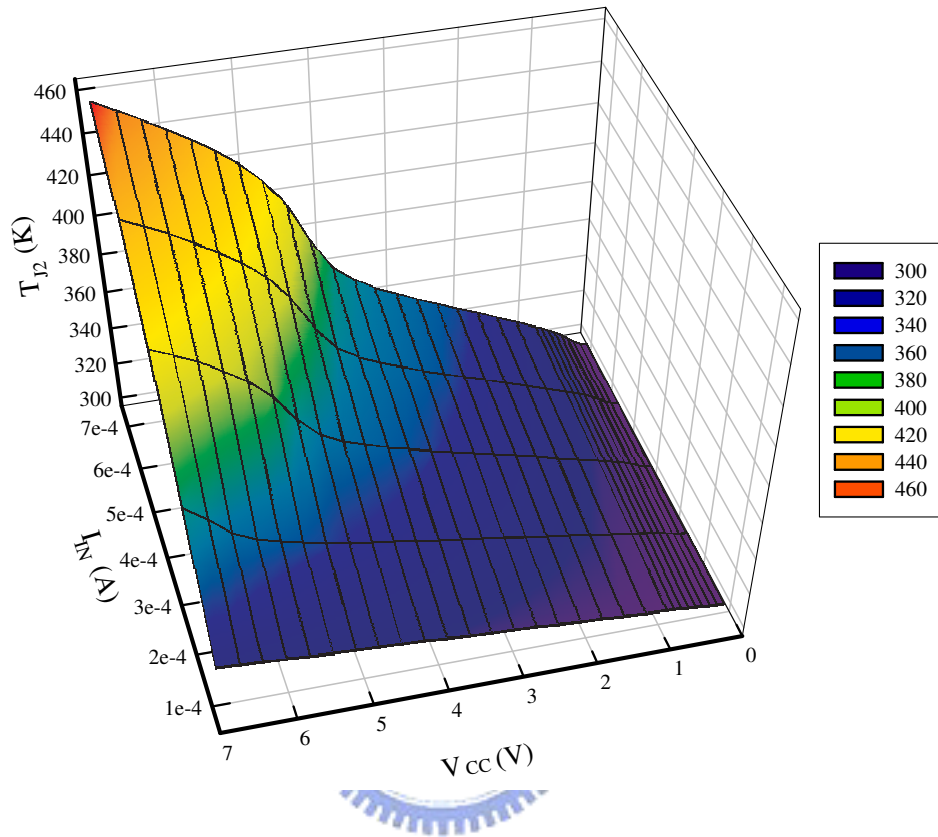


Figure 4.12: T_{J2} with respect to V_{CC} and I_{IN} .

In NDR region, all fingers shares relatively even amount of current and the junction temperatures increase gradually with V_{CC} . In contrast, as the device power is almost dissipated in Finger 2 and T_{J2} surges rapidly in the collapse region, the current gain suddenly plummets.

4.4 Summary of This Chapter

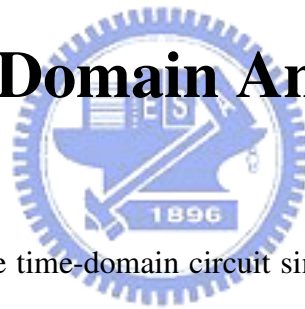
We presented the DC simulation and the comparison between our simulated outcome and HSPICE's results in this chapter. The contents of this chapters are written as:

- our DC simulation results for an HBT, which is compared with measured data and results of HSPICE solver,
- the simulated results with the consideration of self-heating effect, and
- the DC simulation for an multi-finger HBT with self-heating and thermal coupling effects.

The DC results are the initial condition of the time-domain simulation discussed in next chapter. With accurate initial value, our solver can deliver stable and reliable solution for large-signal time-domain circuit problem.

Chapter 5

Time Domain Simulation and Frequency Domain Analysis



We focus on the time-domain circuit simulation in this work. With the algorithms discussed in Chapter 3, the coupled nonlinear ODEs of the simulated circuits are solved in time-domain without any approximation. Thus, the accuracy of the time-domain analysis with this method is guaranteed. Based on the efficiency of this method, we significantly reduce the consumed simulation time for intermodulation distortion analysis, which is a major weakness in the most of time-domain methods. The other improvement is the prevention of error propagation. As the simulated time steps increase, the max norm error become larger for the traditional Newton's iterative (NI) related methods. With the robustness of MI method, our method

can keep its accuracy after tremendous time steps. We demonstrate the simulated results in time-domain of both our method and HSPICE simulator in this chapter. The HSPICE is a well-known NI-based numerical solver. Compared with HSPICE, our method shows its capability to simulate the intermodulation distortion. In addition, the spectrums after FFT are also be shown in this chapter. These frequency-domain results illustrates the difference between our method and HSPICE simulator more clearly.



5.1 Non-Thermal-Effect Simulation

The results of time-domain simulation for the circuit plotted in Fig. 2.2 is demonstrated in this section. The function of input excitation is written as Eq. (2.41). Fig. 5.1 is the result simulated by our proposed method.

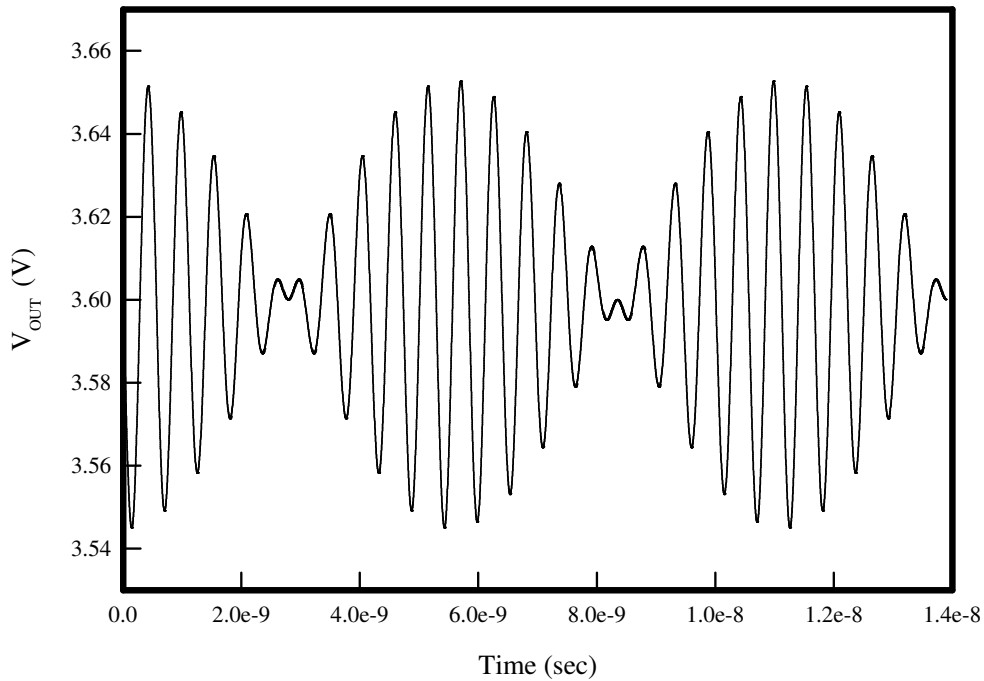


Figure 5.1: The time-variant V_{OUT} , which is simulated by our numerical solver.

Where V_m , V_{IN} and V_{CC} are equal to 0.05, 1.402, and 3.6 V, respectively. The fundamental frequencies f_1 and f_2 are set to be 1.71 and 1.89 GHz. In the meanwhile, the result of HSPICE simulator with the same simulation conditions is shown in Fig. 5.2. We note that the setting of `.OPTIONS ACCURATE`

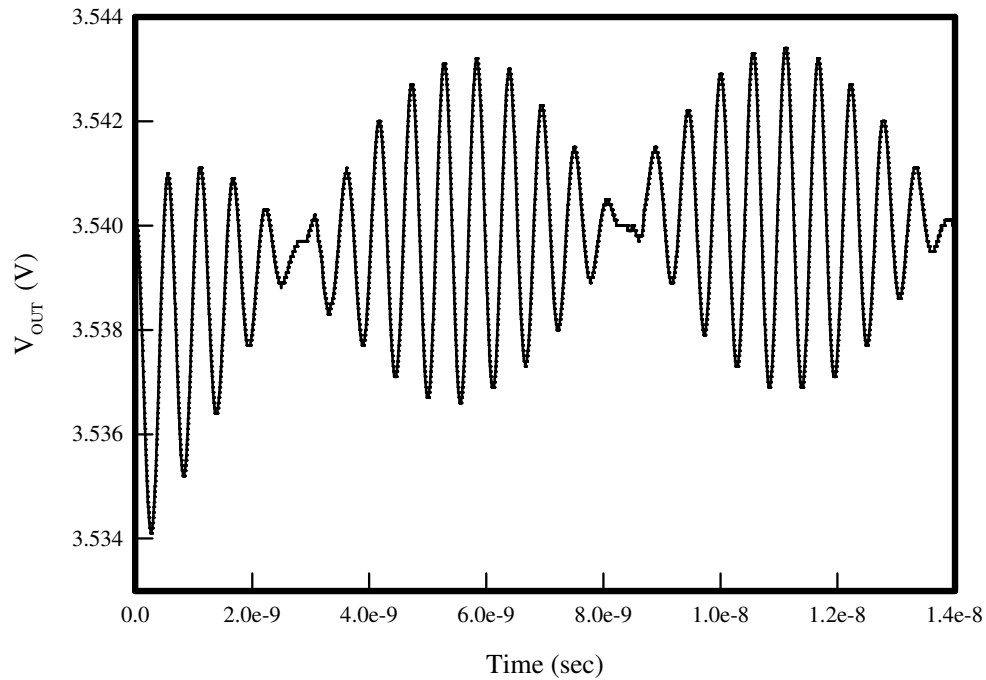


Figure 5.2: The time-variant V_{OUT} , which is simulated by HSPICE solver.

for HSPICE is selected in the performed simulations. The even time step size for output time-domain data is set to be 5×10^{-13} sec. The evenly separated time step is used for the need to do FFT. The real step sizes during the process of time-domain simulation are adaptive for the required TOL (see also Sec. 3.1.2) in both our method and HSPICE.

In Fig. 5.1 and Fig. 5.2, over 25 periods, which is counted by the central frequency $f_c = 1.8$ GHz, are directly calculated in time-domain with the two-tone excitation. Contrary to the HSPICE's result, which initially has some

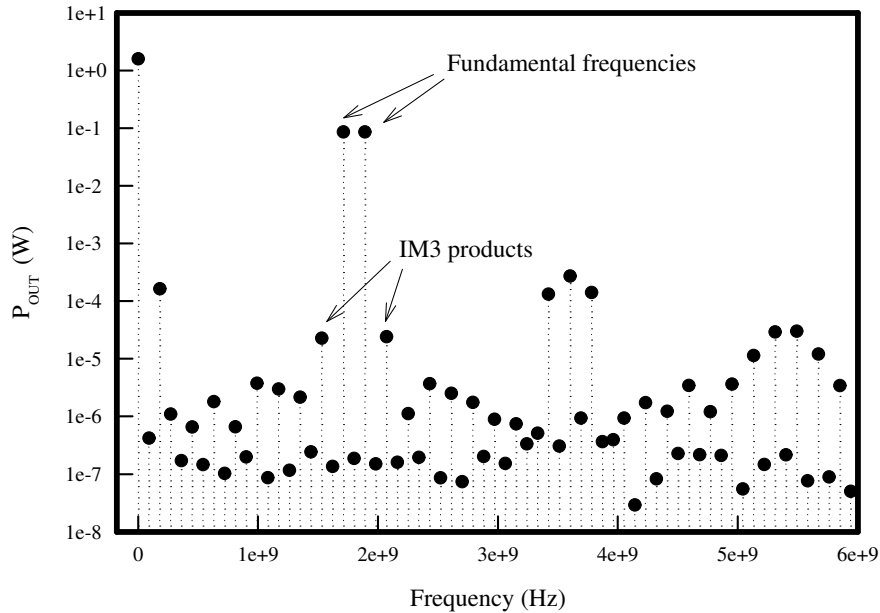


Figure 5.3: The plot for the output power spectrum ,which bases on the FFT results of Fig. 5.1.

unstable outputs, our simulator presents its robustness in large-signal time-domain transient analysis. The initial unstable cycles, as shown in Fig. 5.2, is called the start-up sequence. For the resolution in the frequency domain as discussed in Sec. 3.3, we need time-domain data for 20 cycles, in other words, time window equals 11.11 ns. To prevent including the behavior of the start-up sequence, the first 5 cycles in Fig. 5.2 has been removed in the calculation of FFT. In particular, we counted the 6-25 cycles of the data both in Fig. 5.1 and Fig. 5.2. The corresponding spectra of Fig. 5.1 and Fig. 5.2 is shown in Fig. 5.3 and Fig. 5.4, respectively.

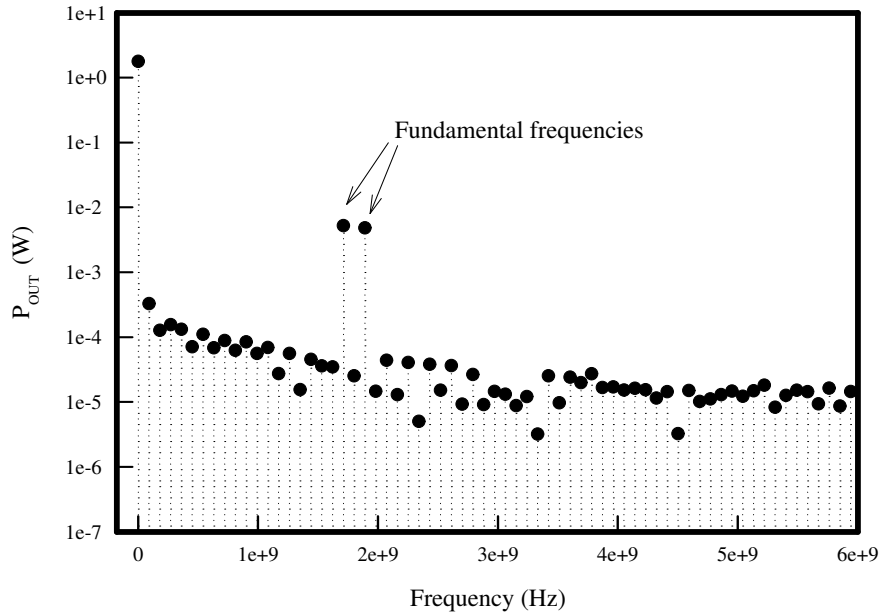


Figure 5.4: The plot for the output power spectrum ,which bases on the FFT results of Fig. 5.2.

In the spectrum of our simulated data, the peaks at the fundamental frequencies, IM3 product at $2f_1 - f_2$ and $2f_2 - f_1$, and the higher order products can be identified clearly in the same time. In contrast, only the peak at fundamental frequencies can be found in Fig. 5.4. Through FFT, the error of numerical method in time domain causes the noise-like signal in frequency domain. In this work, the noise level for our result is about 10^{-7} W and for HSPICE's result is between 10^{-4} and 10^{-5} W. Our methodology demonstrate its superiority in this simulation case.

As shown in Fig. 5.5(a)-(c) and Fig. 5.6(a)-(c), to clarify the time-domain results calculated with our approach and HSPICE in detail, we have performed more computational investigation. Here, we reset the input amplitude V_m to be 0.005 V. The time windows of sub-figures (a), (b) and (c) are 0 ns – 122 ns, 90 ns – 110 ns, and 107 ns – 110 ns. It is found that, in Fig. 5.5(a), the result also has start-up sequence, which is not obviously observed in Fig. 5.5(a). Comparing the two sub-figures (c), for HSPICE's outputs, the stair-like curve is calculated till 100 ns outputted. This result is because the NI-related method converges quadratically in a sufficiently small neighborhood of the exact solution. In contrast, the result of our solver can still maintain smooth sinusoidal waveform as shown in Fig. 5.5(c). In our experience, the erroneous results occur in HSPICE simulation especially for nonlinear devices with time-variant voltage sources.

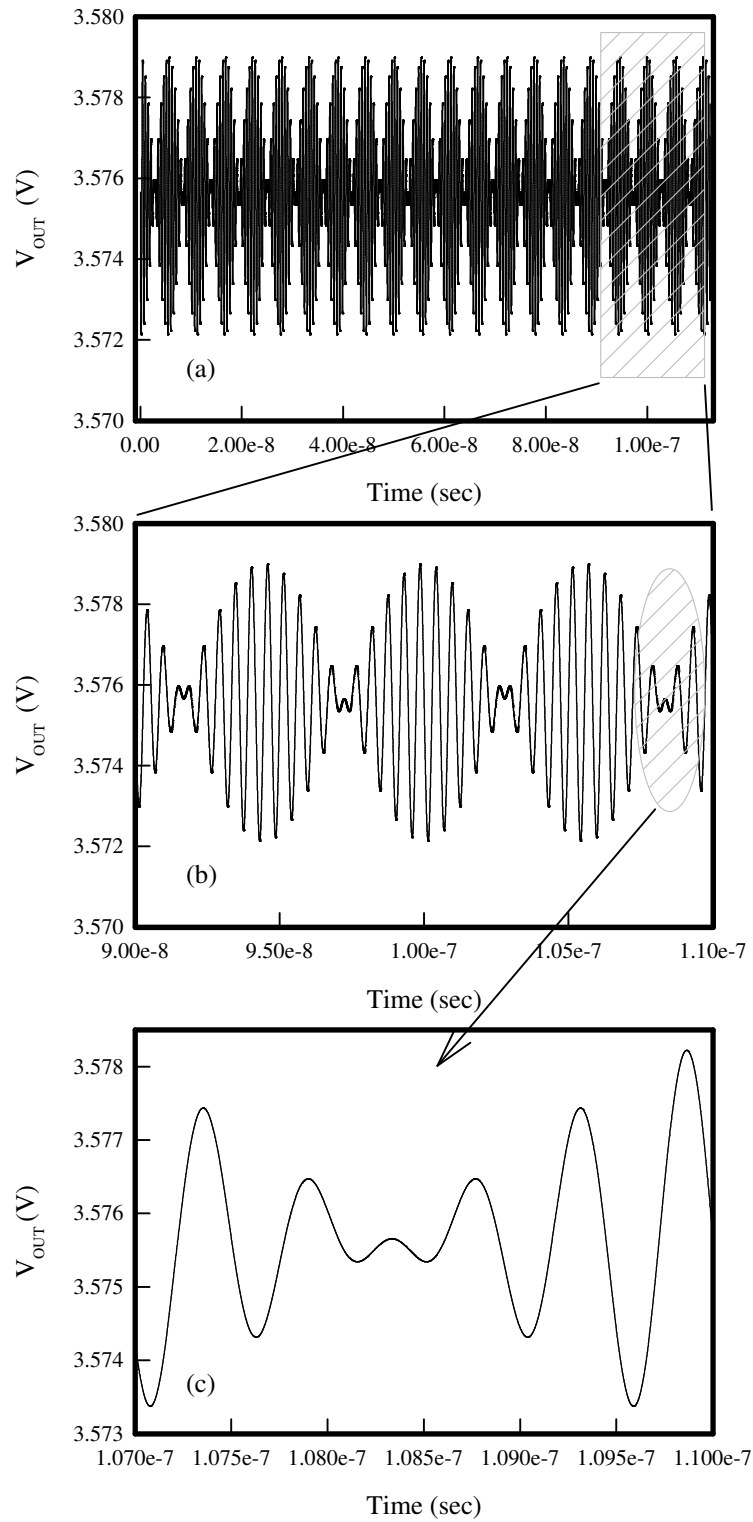


Figure 5.5: Zoom-in plots investigation for V_{OUT} simulated by the developed solver.

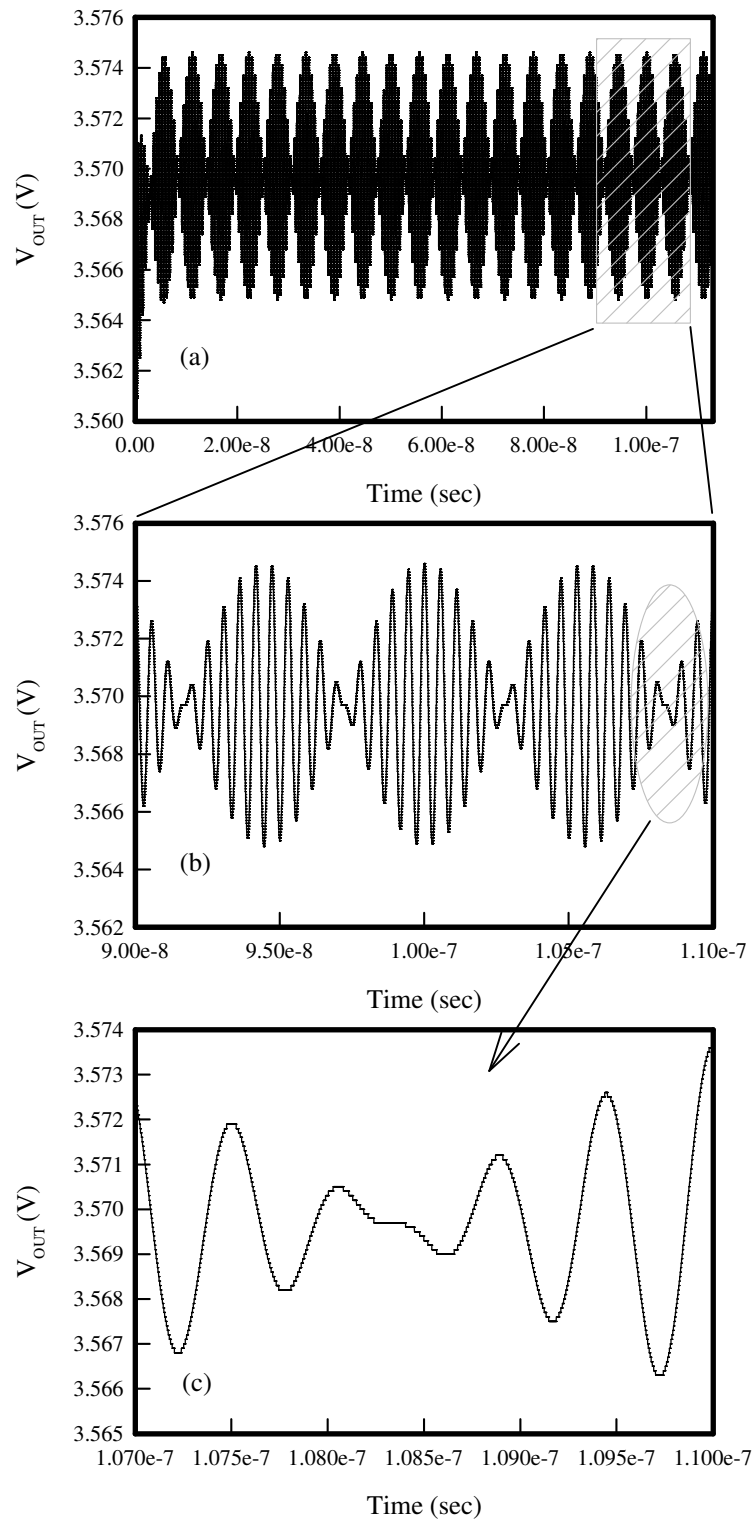


Figure 5.6: Zoom-in plots investigation for V_{OUT} simulated by HSPICE.

5.2 Results with Self-Heating Effect

We introduce the self-heating effect into the time-domain simulation. Since the thermal effect will change the bias condition, it can influence the time-domain behavior, too. By the algorithm proposed in section 3.1.4, the circuit as plotted in Fig. 2.3 is simulated. The parameters are listed in Table 4.2 and the thermal resistance R_{TH} equals $1834.20\text{ }^{\circ}\text{C}/\text{W}$. Besides, the multiplier factor M is set to be 3. The DC biases exercised in this section are $I_{IN} = 1.0\text{ mA}$ and $V_{CC} = 6.5\text{ V}$. Here, the input excitation is a two-tone power source as written in Eq. (2.42). At base of the HBT, the node equation (2.35) becomes different for the voltage of this node becomes an new unknown. The utilization of power source in this simulation is because of the clearly identification for input power level without additional calculation. The given input power is -22 dBm per tone and the time-domain simulation is continued till 68.33 ns (123 cycles at 1.8 GHz). In contrast with our simulated result in Fig. 5.7(a)-(c), the output of HSPICE simulator is demonstrated in Fig. 5.8(a)-(c).

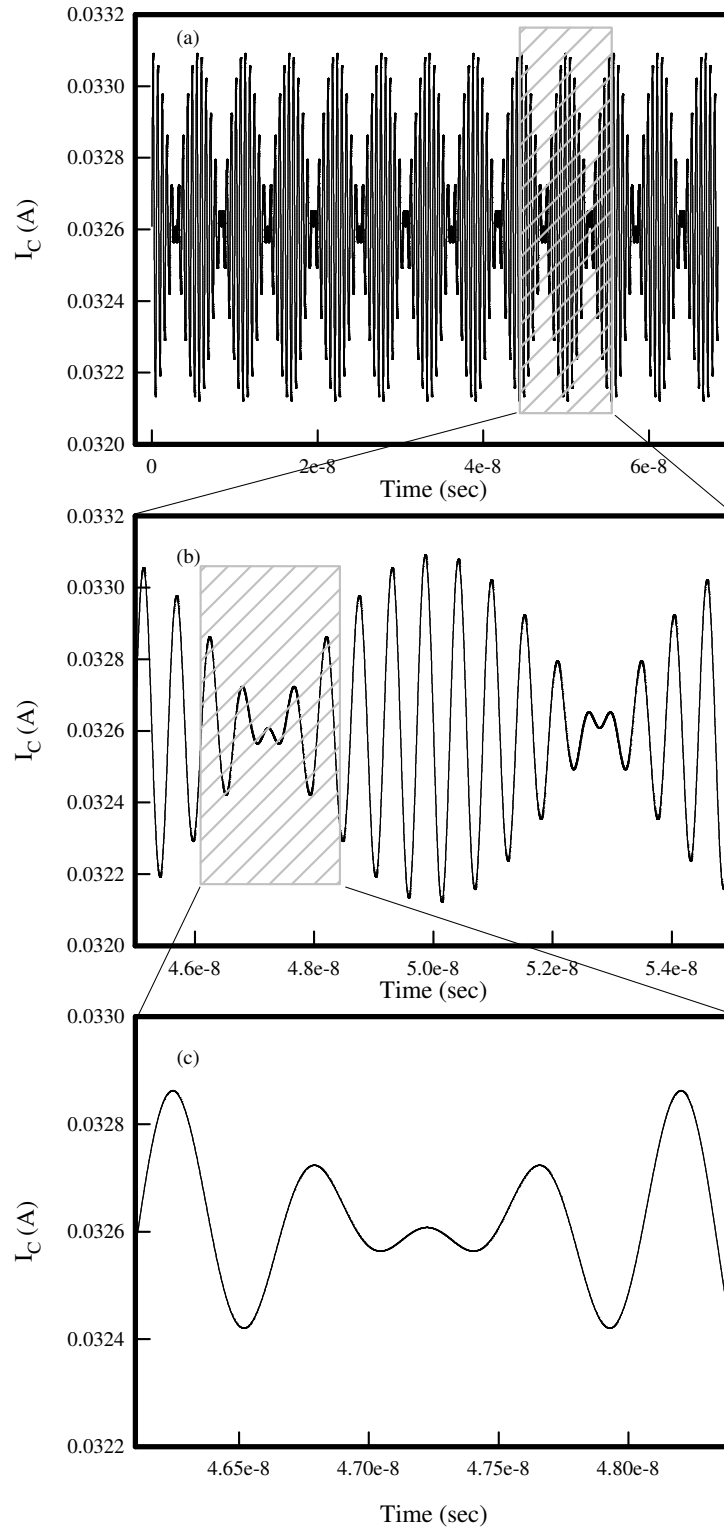


Figure 5.7: Zoom-in plots investigation for I_C simulated by the developed solver.

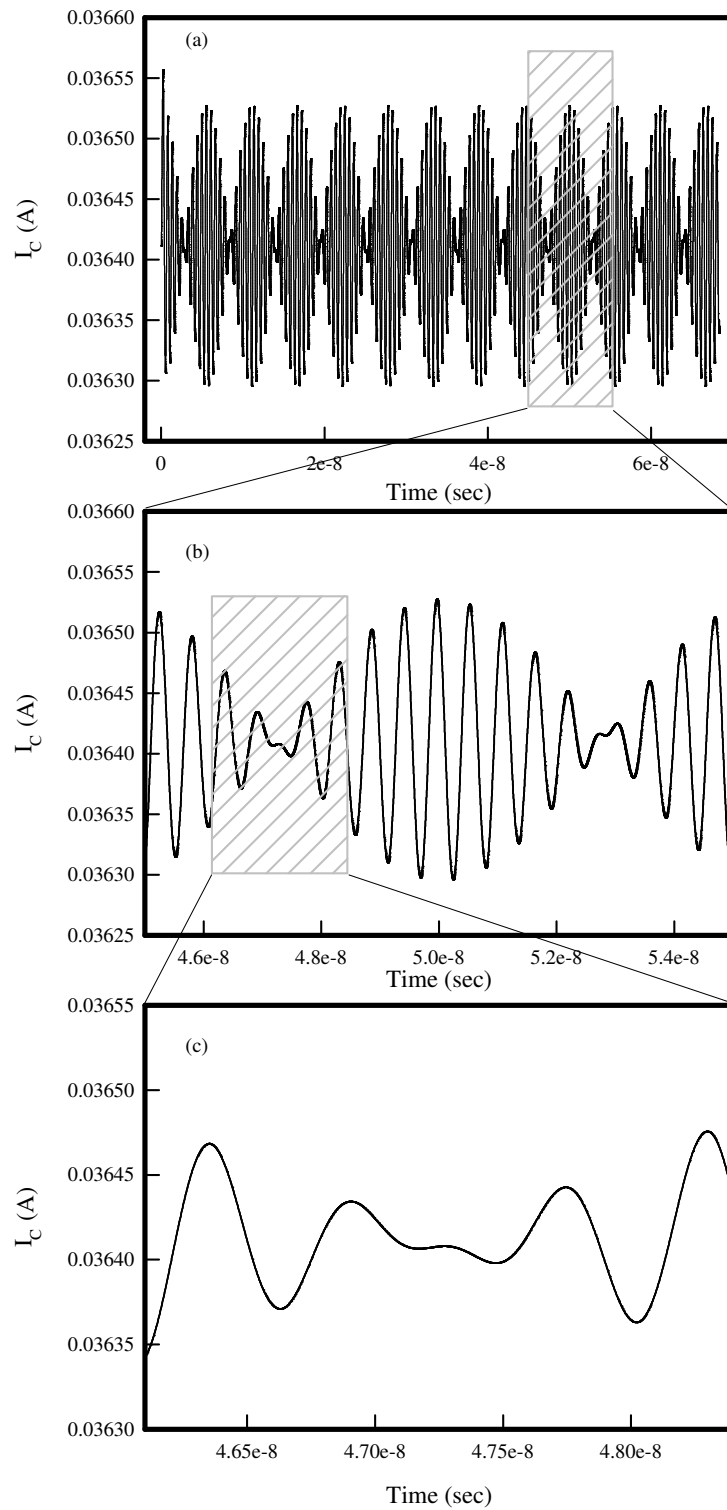


Figure 5.8: Zoom-in plots investigation of I_C simulated by HSPICE.

On the one hand, the result of our method is still stable and smooth. The usage of power source dose not affect the calculation of our developed solver. On the other hand, the result of HSPICE, especially in Fig. 5.8(c), becomes much smooth than the result shown in Fig. 5.6(c). It is because that we utilize

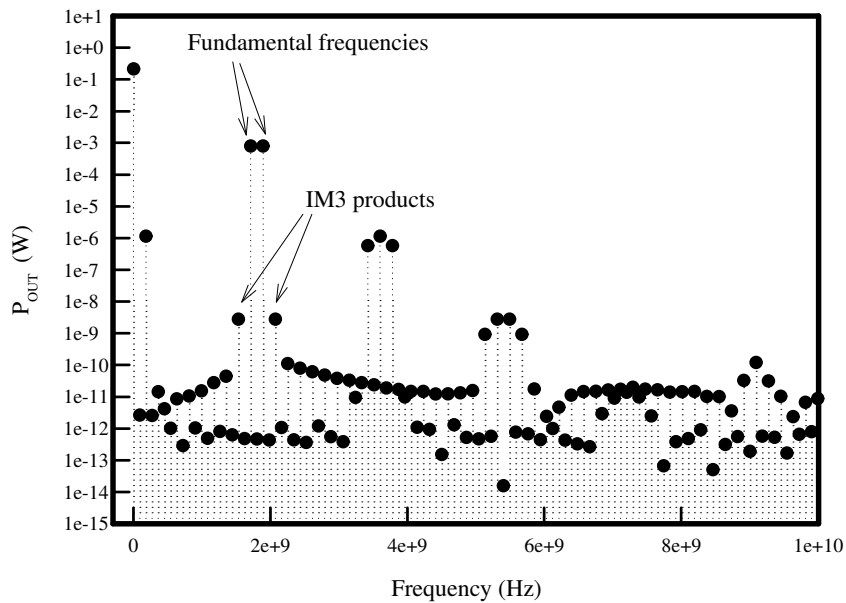


Figure 5.9: Spectrum of P_{OUT} simulated by our solver including the self-heating effect.

time-variant current source in the HSPICE simulation and the current source is equalized in power magnitude to the power source used in our simulator. The transient analysis of HSPICE solver can handle the nonlinear circuits with current source better than those with voltage source. But, the unstable start-up

sequence caused by numerical method is still be found in Fig. 5.6(a). Furthermore, although the result seems become better in Fig. 5.6, there is still some degradation in sub-figure (c). If we transfer the outputs to frequency domain, the unapparent inaccuracy leads an erroneous FFT outcome. In the compari-

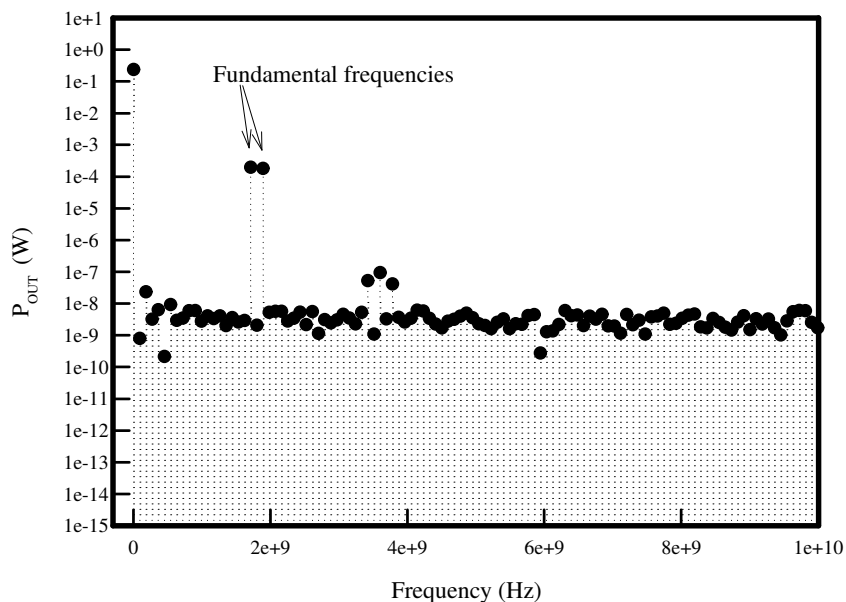


Figure 5.10: Spectrum of P_{OUT} simulated by HSPICE solver including the self-heating effect.

son between Fig. 5.9 and Fig. 5.10, the noise level of our result and HSPICE's are about 10^{-12} W and 10^{-9} W. So that the IM3 products can only be recognized from Fig. 5.9, which is the data for the OIP3 value calculation. In order to investigate the heating effect, we perform the simulation for the circuit in Fig. 2.3 again, but ignore the corresponding thermal network. In other words,

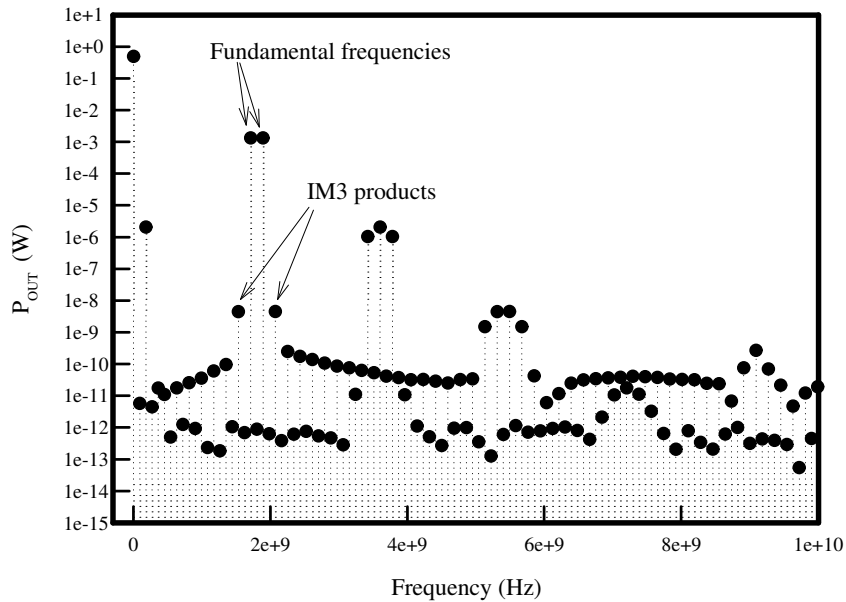


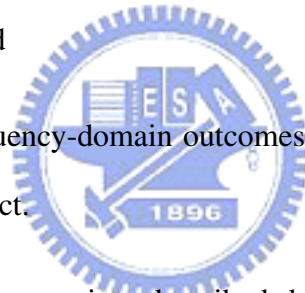
Figure 5.11: Spectrum of P_{OUT} simulated by our solver without the self-heating effect.

all the settings are the same except the R_{TH} , which is set to be zero in this calculation. Figure 5.11 shows the FFT outcome of the time-domain data. The result is quite similar to Fig. 5.9. But, without thermal effect, the performance of this device is over estimated. The output power at 1.71 and 1.89 GHz are both 1.1663 dBm. In contrast, the result with consideration of self-heating are -1.0232 and -1.0233 dBm at 1.71 and 1.89 GHz, respectively. The self-heating effect degrades not only the output power but also the linearity. The OIP3 value is reduced from 28.5148 dBm to 26.2577 dBm.

5.3 Summary of This Chapter

Comparison between our solver and HSPICE in solving time-domain circuit problem shows the advantages of the proposed numerical algorithms. With the MI method, our solver can prevent error propagation even after tremendous time-step estimations. In this chapter we demonstrated:

- the time-domain simulated results of both our and HSPICE simulator,
- the frequency-domain data after FFT with respect to previous time-domain results, and
- the time- and frequency-domain outcomes including the consideration of self-heating effect.



From the simulation and comparison described above, we execute further analyses, for example, the distortion analysis in the following chapter.

Chapter 6

Intermodulation Distortion and Power Characteristics



By the discrete Fourier transform, the information in frequency domain is extracted from our time-domain calculated data. These discrete intensity or power at sampled frequencies can be converted to useful engineer data by proper calculation. In the section 3.3, the intermodulation distortion analysis is briefly described. For narrow band communication, in order to prevent channels from cross talk, the two-tone intermodulation nonlinearity is an important benchmark to verify the quality of the devices. In fact, all practical devices and systems are either strongly or weakly nonlinear. With a limited range of bias and operating frequencies, some lumped elements can be treated as linear components and the circuit can be divided into linear and nonlinear parts. The developed simulation kernel has its superiority on solving strongly

nonlinear circuit. This advantage had been demonstrated in previous chapters. By utilization of this kernel, we can perform correct intermodulation distortion and power analysis. In this chapter, the estimation of OIP3 values for an HBT without thermal effects is described first. Then, the characterization of an HBT with the self-heating effect and the multi-finger devices with thermal coupling effect are discussed sequentially in the next sections. After all, a brief summary of this chapter is given.



6.1 Characteristics without Thermal Effects

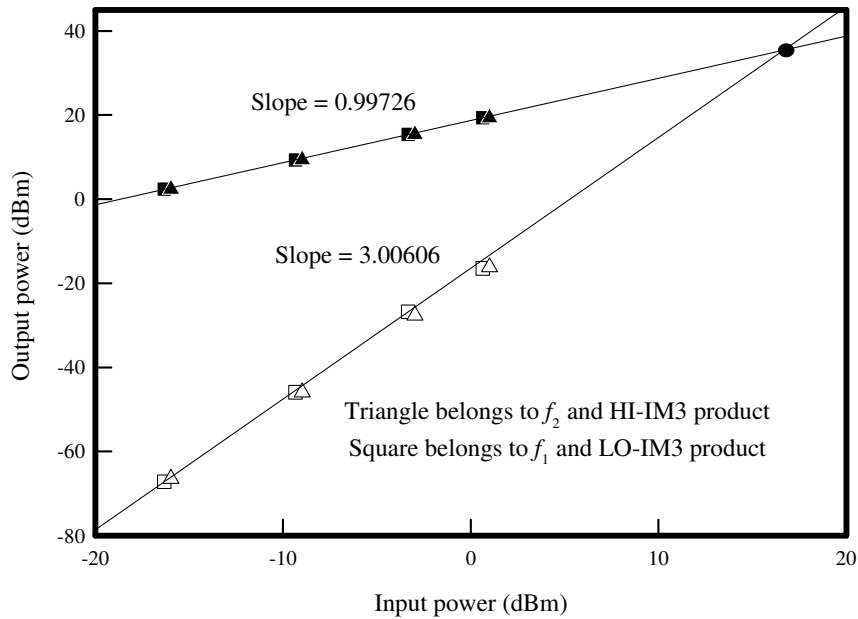


Figure 6.1: Output power, simulated by our solver, at the fundamental frequencies (black-filled symbol) and the IM3 products (white-filled symbol) versus input power.

As the illustration in Fig. 3.11, the third order intermodulation (IM3) products at $2f_1 - f_2$ and $2f_2 - f_1$ are denoted as LO-IM3 and HI-IM3, respectively. In our simulation, f_1 and f_2 are set to be 1.71 and 1.89 GHz. Therefore, the frequencies of LO-IM3 and HI-IM3 become 1.53 and 2.04 GHz. The plots of extracted output powers at the fundamental frequencies and IM3 products versus input powers are demonstrated in Fig. 6.1 and Fig. 6.2. The slopes of

our calculated data in dBm scale are 0.99726 and 3.00606. These values are almost identical to the theoretical values (1 and 3) discussed in section 3.3. From the cross-point of the extrapolated lines, we can get the value of output third-order intercept point (OIP3), which equals 36.9 dBm. We noted that the HI-IM3 and LO-IM3 are close enough and, hence, they have almost the same OIP3 values. Unfortunately, as shown in Fig. 6.2, the slopes of the fundamental frequencies and IM3 products from the simulated time-domain data by HSPICE solver are equal to 0.99964 and -0.28781 , respectively. It leads to a

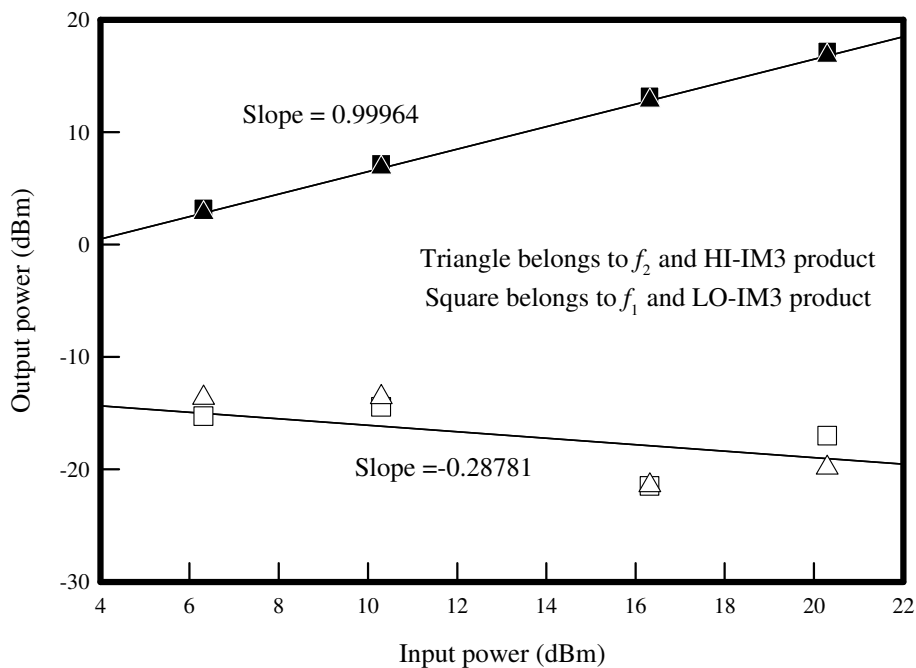


Figure 6.2: Output power, simulated by HSPICE solver, at the fundamental frequencies (black-filled symbol) and the IM3 products (white-filled symbol) versus input power.

nonpredictable OIP3 value and is caused by the errors of numerical method in time-domain.

For an input power, we can also estimate the OIP3 value with output spectrum. If the slopes of the fundamental frequencies and IM3 products are 1.0 and 3.0, the OIP3 values is directly given by

$$\text{OIP3 Value} = P_O^{\text{FF}} + \frac{1}{2}(P_O^{\text{FF}} - P_O^{\text{IM3}}), \quad (6.1)$$

where P_O^{FF} and P_O^{IM3} represent the output powers of the fundamental frequencies and IM3 products, respectively. Fig. 6.3 shows the OIP3 values with respect to different frequency spacing ($\Delta f = f_1 - f_2$) between fundamental frequencies. The OIP3 values of HI-IM3 and LO-IM3 are denoted by HI-OIP3 and LO-OIP3. Besides, the central frequency f_c of each OIP3 calculation is identical and equals to 1.8 GHz. As shown in Fig. 6.3, there are only slight deviations of OIP3 values as Δf increases. Variation of Δf from 360 to 20 MHz produces $|36.5294 - 36.5014| = 0.0180$ dBm difference in LO-OIP3. In addition, the difference between LO-OIP3 and HI-OIP3 are 0.0719 and 0.0034782 dBm when Δf varies from 360 to 20 MHz. With this observation, our approach enables us to efficiently calculate the two-tone intermodulation distortion with a larger Δf . On the one hand, for $\Delta f = 20$ MHz, we have to preform the computation with over 180 cycles for good FFT resolution in frequency domain (see also Sec. 3.3). On the other hand, for $\Delta f = 360$ MHz, there are only ten cycles required. From our numerical experience, we would like to point out that our method can compute the simulation condition with a

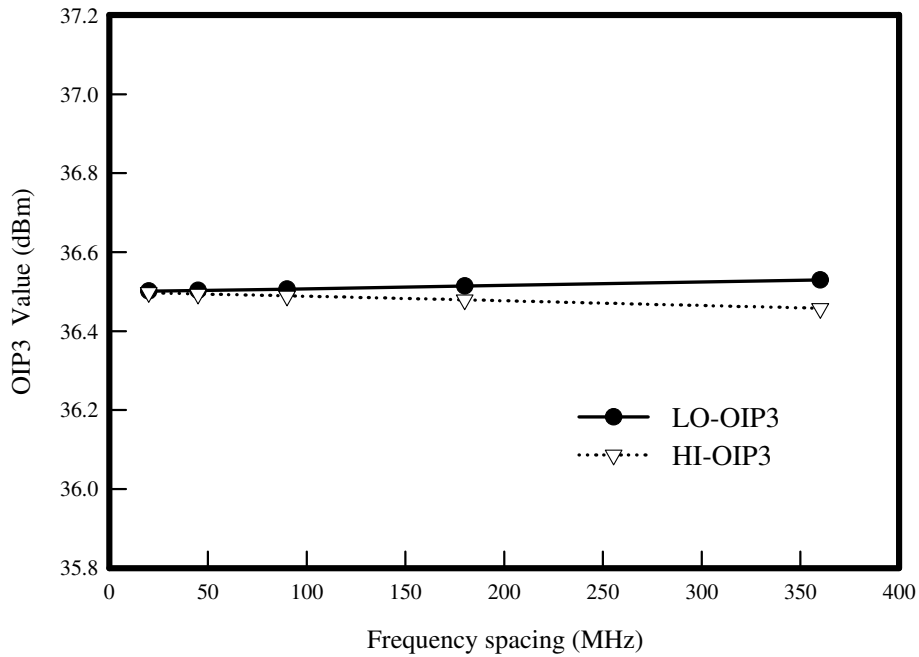


Figure 6.3: A deviation plot of OIP3 value versus frequency spacing Δf .

narrow tone spacing of 10 MHz. In our practical implementation, this method provides a more efficient computing alternative and may overcome one of the weakness of the conventional time-domain approaches, such as the enormous requirement of computational resources.

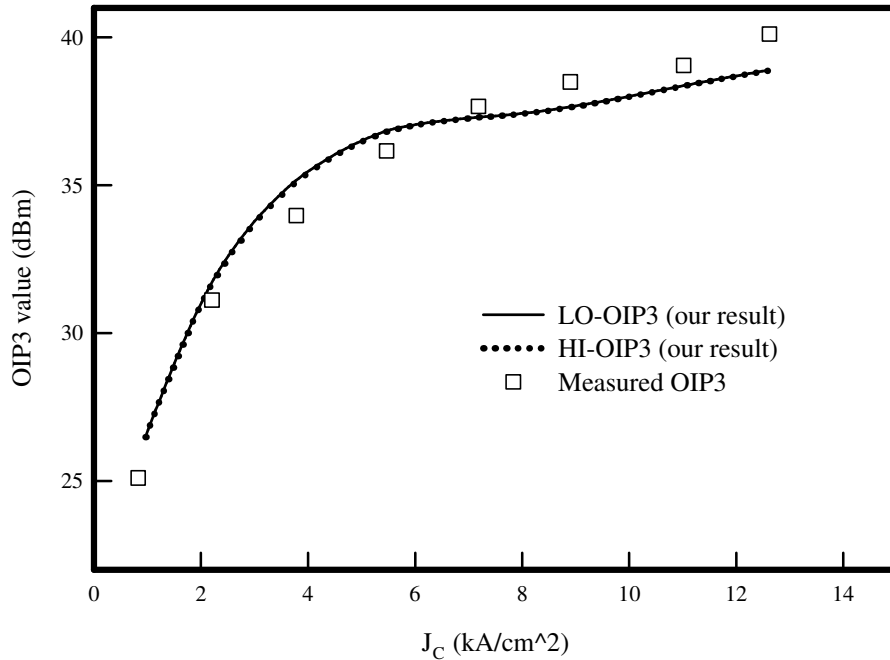


Figure 6.4: Plots of OIP3 value versus J_C , where symbols are measured data and lines are simulated results of our proposed method.

By utilization of on-wafer device testing with harmonic load-pull system mentioned in Sec. 3.4, we compare the results of simulation with the data from measurement. Fig. 6.4 shows the OIP3 values versus collector current density J_C . Here, we note that unit of J_C is $\frac{\text{kA}}{\text{cm}^2}$. Our results of HI-OIP3 (dotted line) and LO-OIP3 (solid line) are almost coincident in the scale of this figure. Comparing with the the measured data (square symbols), our results indicate their accuracy for different bias conditions. Fig. 6.5 plots the results

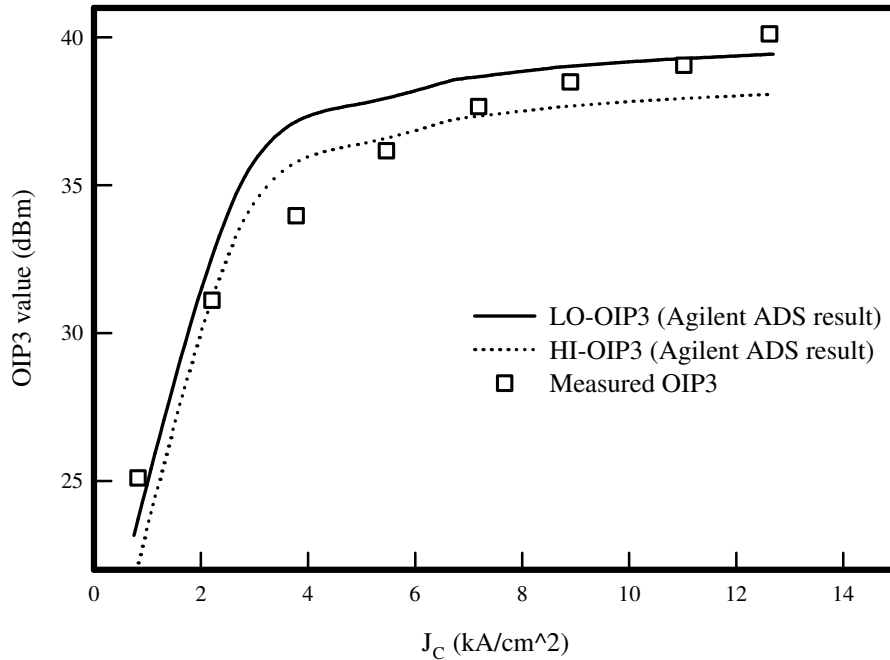


Figure 6.5: Plots of OIP3 value versus J_c , where symbols are measured data and lines are simulated results of harmonic balance method.

of *Agilent Advanced Design System (ADS)*, which is a well-known harmonic balance based RF circuit solver [40]-[63], and measured data. We can also observe a quite fitting results between simulation and measurement. But, there is over a 1 dBm difference between the values of HI-OIP3 and LO-OIP3. Our measurement is performed on an HBT device with $2.8 \times 12 \mu\text{m}^2$ emitter area size \times 104 fingers. In this case, we simply set the multiplier factor M (see also Sec. 2.1) to be 104 in both the our simulator and ADS. The 104 fingers are assumed to be 104 parallel connected one-finger devices. In our

simulation with ADS, we find that the differences between HI-OIP3s and LO-OIP3s always exists and it is difficult to let the measured data, simulated HI-OIP3 and LO-OIP3 fit well at the same time. We should note that, for the curve fitting in Fig. 6.4 and Fig. 6.5, the parameters of device are adjusted to different values when utilize different simulators.



6.2 Characteristics with Self-Heating Effect

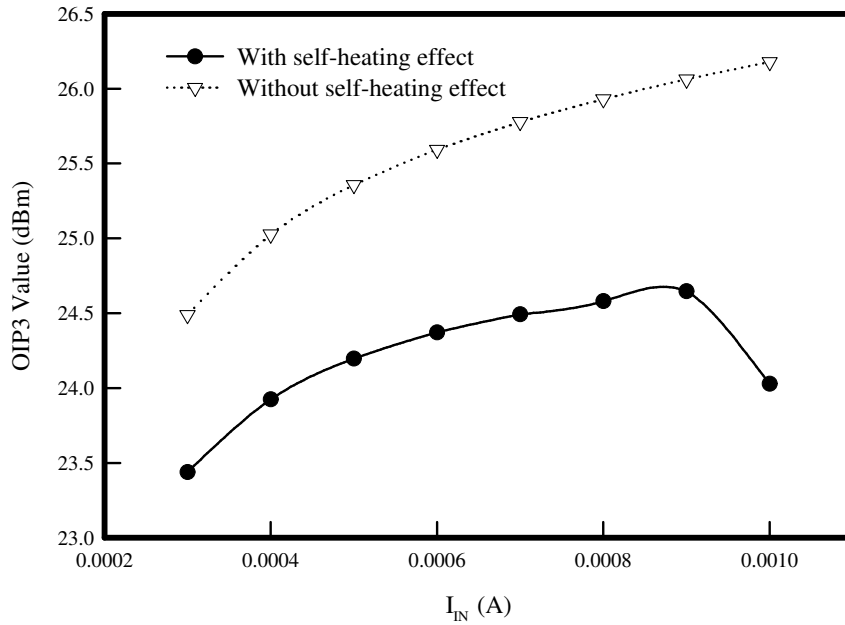


Figure 6.6: A plot of OIP3 values versus I_{IN} , which demonstrates the difference between results with and without the self-heating effect.

Inheriting the frequency-domain results from simulations mentioned in Sec. 5.2, we further calculate the data to analyze intermodulation distortion. The OIP3 values simulated with self-heating and without self-heating effect is plotted in Fig. 6.6. Here, we use LO-OIP3 to stand for OIP3 value in the diagram. The collector bias voltage V_{CC} is set to be 3.8 V and input power is -22 dBm per tone. The OIP3 value raises with the increasing of I_{IN} in the low and medium current bias region. But, with high level current injection, the

heat, which generated by power dissipation, degrades the two-tone linearity of this device. Only the simulation with thermal effect consideration can model the nonlinear phenomenon under high current bias. Without thermal-electrical feedback algorithm described in Sec. 3.1.4, the linearity performance will be over rated as shown in Fig. 6.6.

In addition, we simulated the device two-tone nonlinearity under various

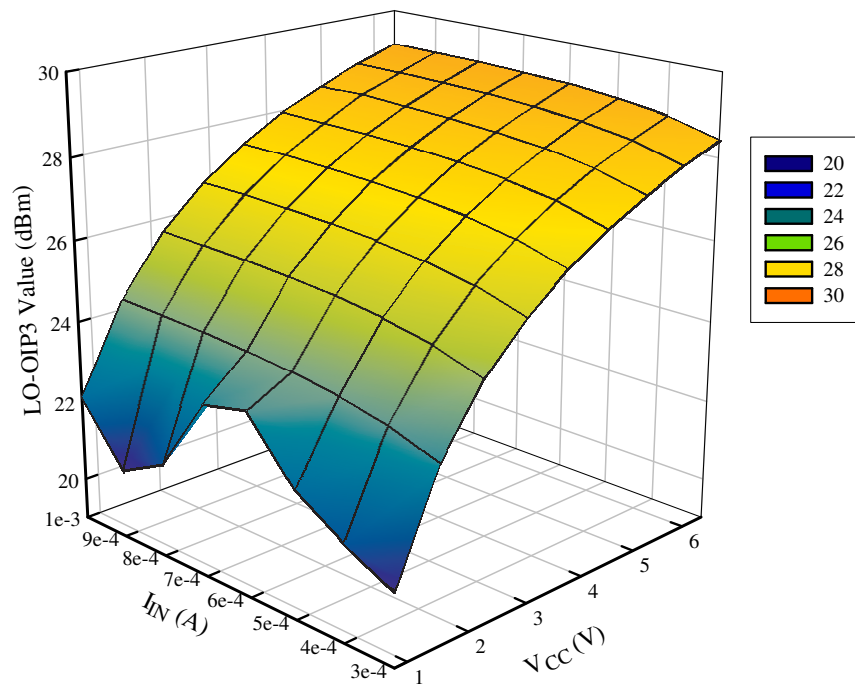


Figure 6.7: Simulated LO-OIP3 values for an HBT under different I_{IN} and V_{CC} biases.

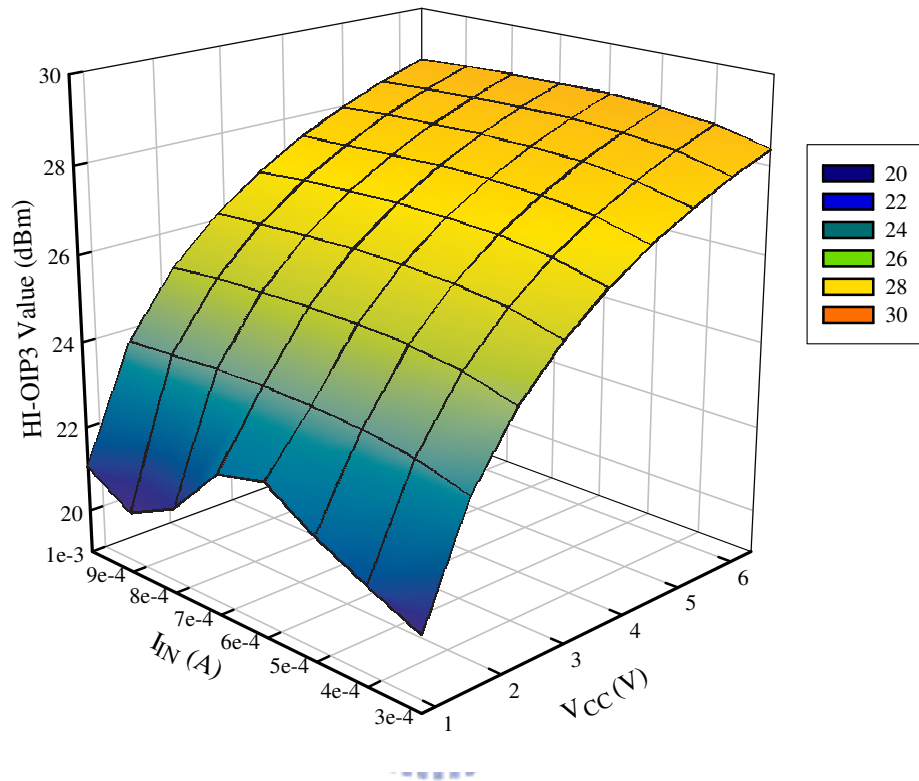


Figure 6.8: Simulated HI-OIP3 values for an HBT under different I_{IN} and V_{CC} biases.

base input current I_{IN} and collector bias voltage V_{CC} . The three dimensional diagram of LO-OIP3 and HI-OIP3 are as shown in Fig. 6.7 and Fig. 6.8, respectively. Both I_{IN} and V_{CC} influence the two-tone characteristic. When V_{CC} is at relatively low level, the OIP3 value varies rapidly under different I_{IN} injection.

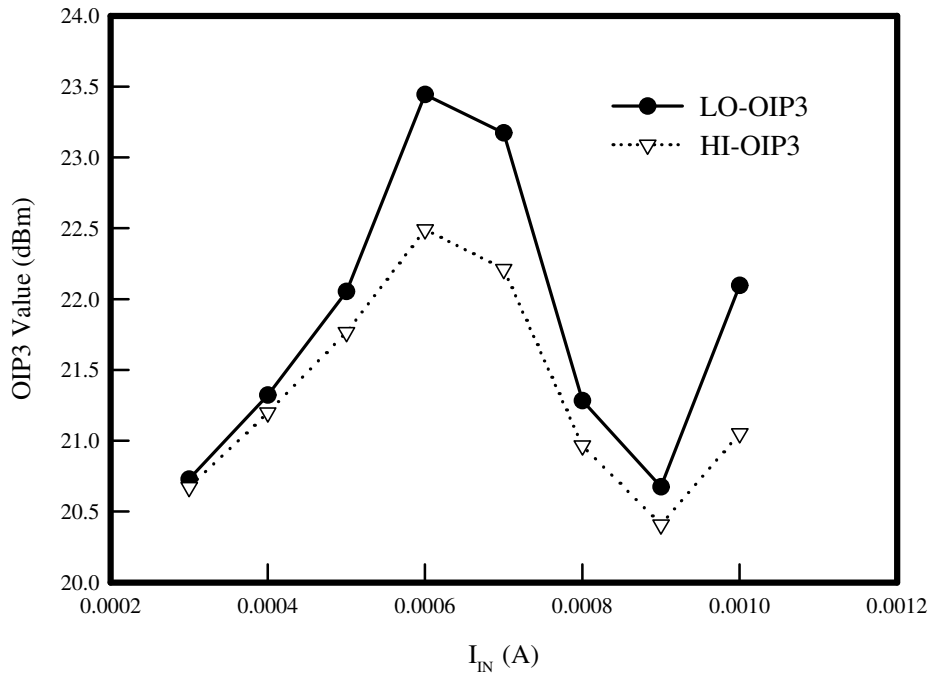


Figure 6.9: A plot of OIP3 values versus I_{IN} , where V_{CC} is set to be 0.8 V.

The detail is presented in Fig. 6.9, where V_{CC} equals 0.8 V. At this collector bias, the device is just in between the active and saturation region so that the device shows strongly nonlinear characteristic. In contrast, we extract OIP3 value variation at high collector voltage operation from Fig. 6.7 and Fig. 6.8. As the phenomenon seen in Fig. 6.6, the two-tone linearity is degraded by heat. The LO-OIP3 and HI-OIP3 begins to separate at higher voltage bias and current injection. In Fig. 6.10, here $V_{CC} = 6.4$ V, the difference between LO-OIP3 and HI-OIP3 is over 0.3 dBm at $I_{IN} = 1.0$ mA. This

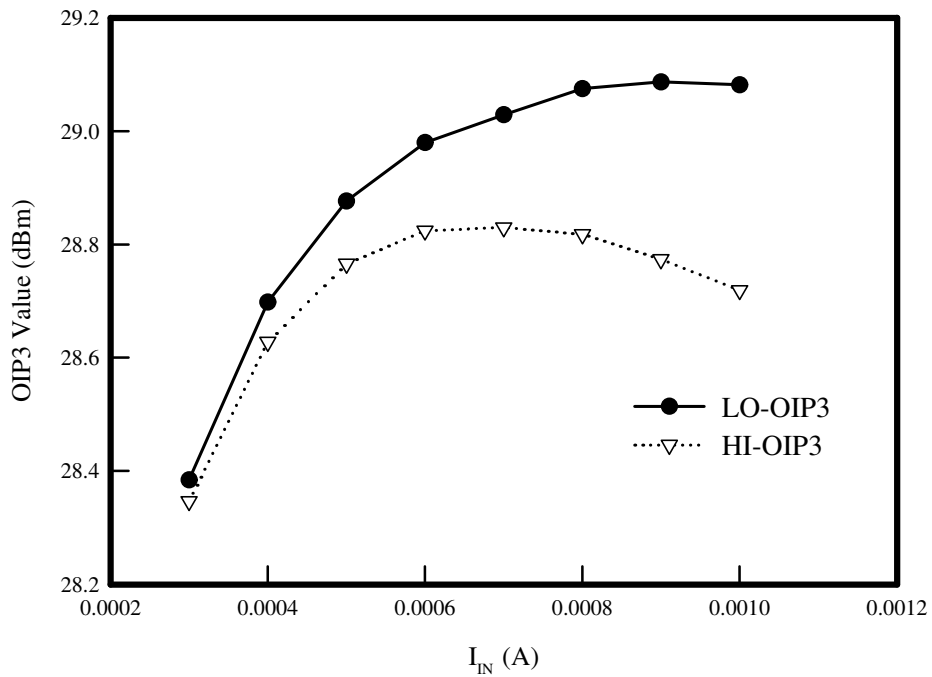


Figure 6.10: A plot of OIP3 values versus I_{IN} , where V_{CC} is set to be 6.4 V.

is also one kind of heat-caused nonlinear characteristic.

6.3 Characteristics with Thermal Coupling Effect

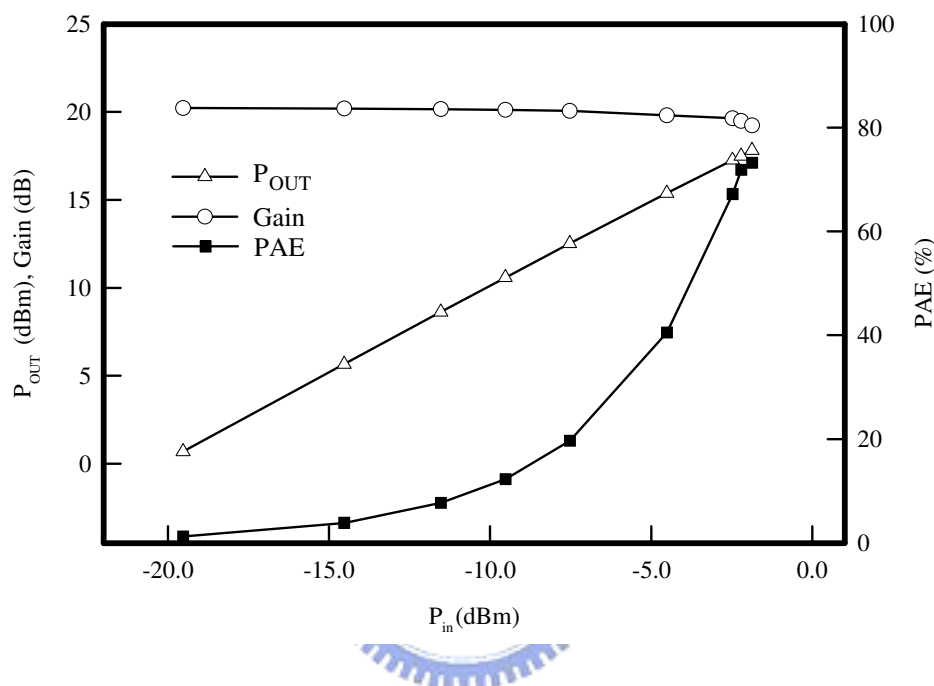


Figure 6.11: Plots of output power, PAE, and power gain versus P_{in} , respectively.

In this section, we demonstrate some single-tone and two-tone characteristics, which extracted from the time-domain simulation of a three-finger HBT device. For the finger of this device, not only self-heating effect of itself has been considered, but also the heat coupling from other fingers is counted. The related algorithm is discussed in Sec. 3.1.4. We note that the parameters of this device is listed in Table 4.2, and the theoretical values of thermal resistances R_{TH0} , R_{TC1} and R_{TC2} are 1834.20, 487.04 and 101.43 °C/W, respectively.

As the input excitation is a single-tone signal at 1.8 GHz, Fig. 6.11 shows the output power (P_{OUT}), power-added efficiency (PAE), and power gain for different values of input power (P_{in}). The definition of PAE is written as:

$$\text{PAE} \equiv \frac{\text{Output Power} - \text{Input Power}}{\text{DC Dissipated Power}} \approx \frac{P_{\text{OUT}} - P_{\text{in}}}{I_{\text{C,DC}} \cdot V_{\text{CC}}}. \quad (6.2)$$

The bias condition of this single-tone simulation is with $V_{\text{CC}} = 3.6 \text{ V}$ and

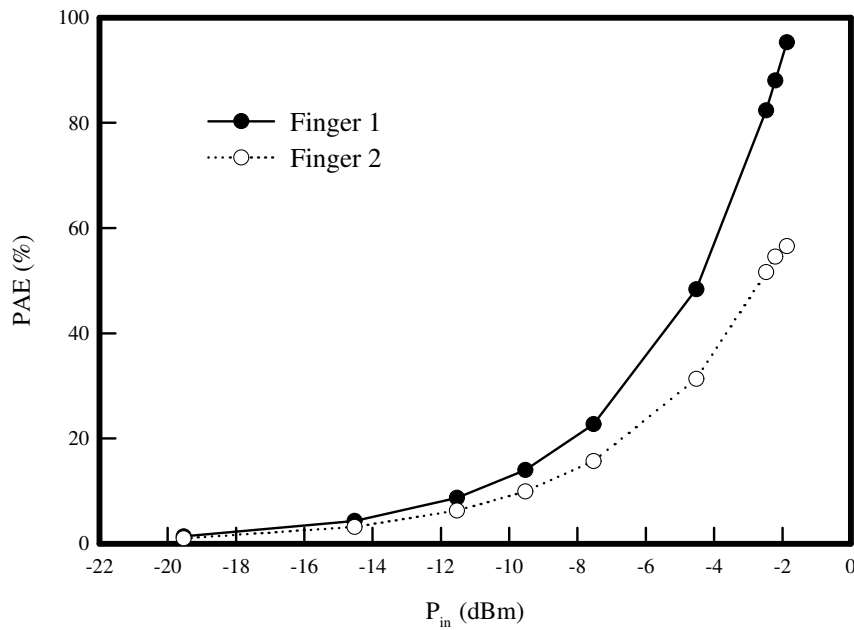


Figure 6.12: Plots of PAE for Finger 1 and 2 versus P_{in} .

$I_{\text{IN}} = 0.6 \text{ mA}$. In this simulation, we have taken the heating effect of input RF power into consideration by adjusting average power for junction temperature iteratively. It is found that, shown in Fig. 6.11, the power gain and PAE

degrade as P_{in} increases. With the curve of power gain, we can find the input power where the power gain decrease for 1-dB in magnitude. This input power is called 1-dB compression point (P_{1dB}) and it equals -2.45 dBm in this case. The thermal coupling effect among fingers also influenced the performance of the three-finger device. As shown in Fig. 6.12, the PAE of the central finger (Finger 2) is lower and degrades when $P_{in} > -3$ dBm. In the meanwhile, the PAE of side finger (Finger 1) still raises as P_{in} increases. This phenomenon illustrates that the performance degradation of the whole transistor is mainly caused by the hotter central finger.



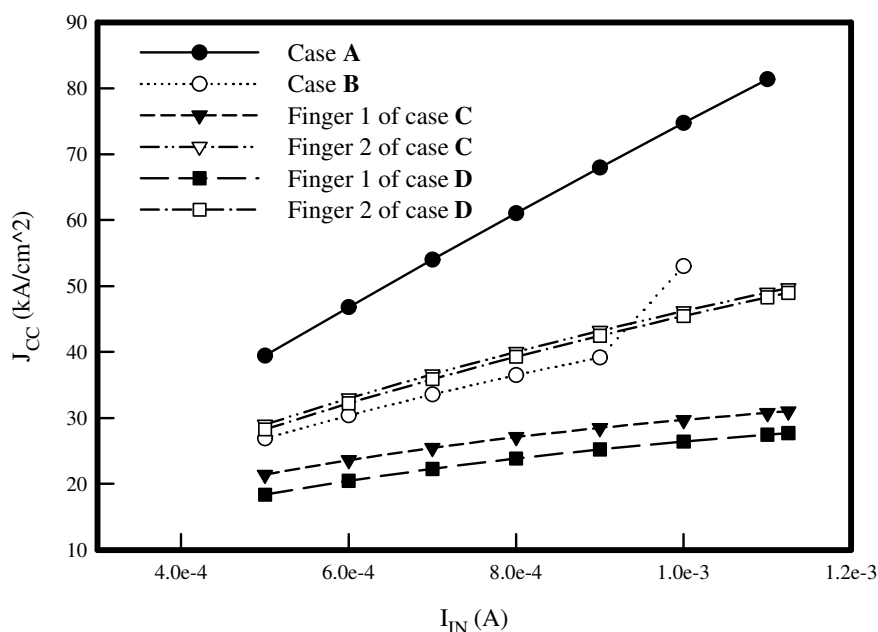


Figure 6.13: Plots of the collector current density (J_{CC}) versus the input bias current (I_{IN}) for the cases **A**, **B**, **C**, and **D**.

For two-tone intermodulation simulation, we perform four testing cases in this section. Each case uses the same model parameters (as shown in Table 4.2), V_{CC} bias (3.6 V) and a two-tone excitation input. The input power of each tone is -10 dBm and the frequencies of this two-tone signal are 1.71 and 1.89 GHz, respectively. In the case **A**, we ignore all thermal effects, in other words, $R_{TH0} = R_{TC1} = R_{TC2} = 0$ °C/W. Only the self-heating effect is included in the case **B**, which means $R_{TC1} = R_{TC2} = 0$ °C/W and $R_{TH0} = 1834.20$ °C/W. For the case **C**, we consider both the self-heating and

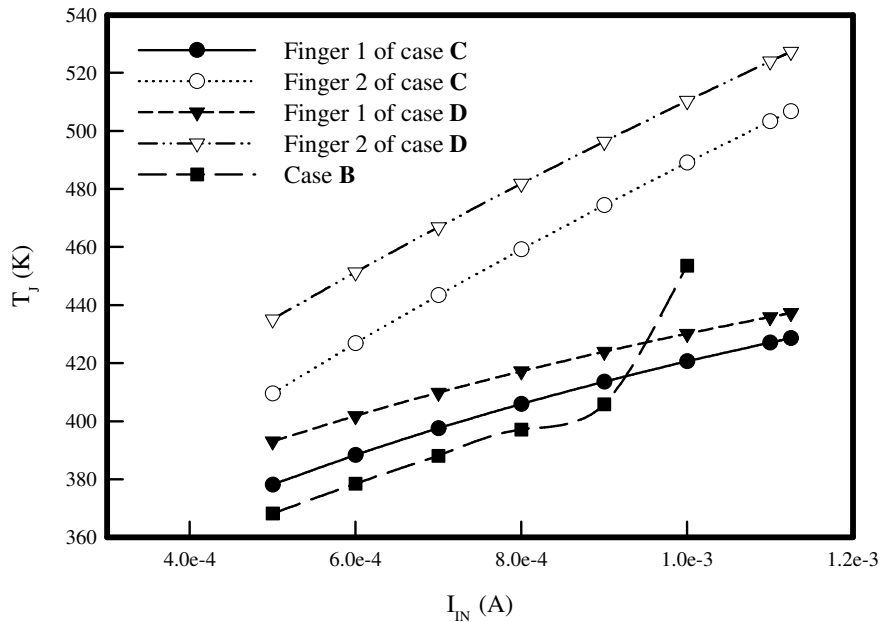


Figure 6.14: Plots of the junction temperature (T_J) versus I_{IN} for the cases **B**, **C**, and **D**.

thermal coupling effects, and the values of thermal resistances R_{TH0} , R_{TC1} and R_{TC2} are 1834.20, 487.04 and 101.43 °C/W, respectively. Finally, the case **D** has the same conditions as the case **C**, besides the consideration for heating effect of input RF signal. To incorporate the heating from the input signal for the case **D**, the averaged additional power is iteratively calculated with Eq. (4.2) and Eq. (4.3) until the junction temperature T_J converged.

The collector current density (J_{CC}) and junction temperature (T_J) of each finger in all cases are shown in Fig. 6.13 and Fig. 6.14, respectively. In the case **A**, T_J keeps a constant value (300 K) and J_{CC} rises almost linearly as I_{IN}

increases since the thermal effects are ignored. It is found that, in the case **B**, there are suddenly jump for J_{CC} and T_J when $I_{IN} > 0.9$ mA. Furthermore, both J_{CC} and T_J of Finger 2 are higher than those of Finger 1 in the cases **C** and **D**. Because of the consideration for additional heating from the RF input signal, T_J in the case **D** is higher than that in the case **C**, and J_{CC} in the case **D** is contrastively lower.

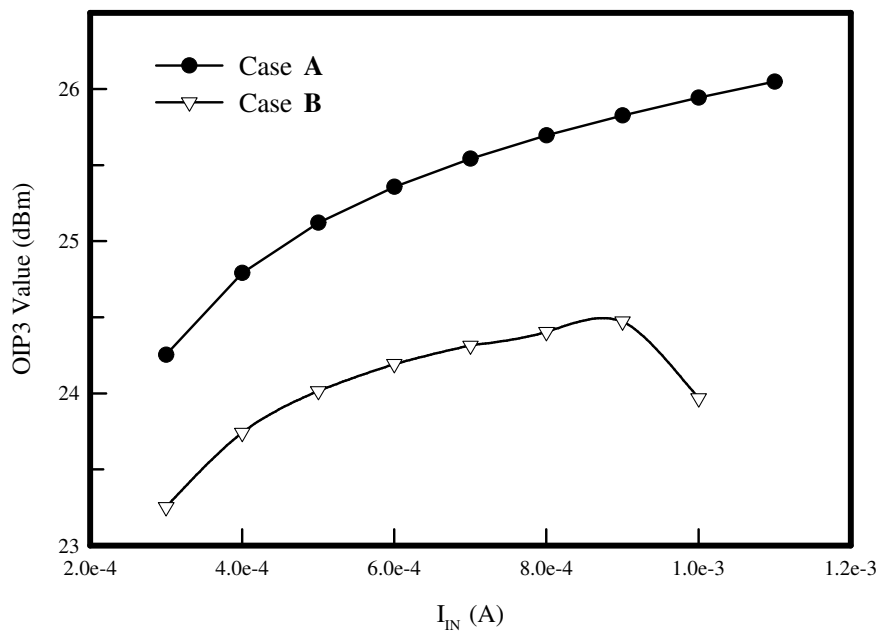


Figure 6.15: A comparison of OIP3 values under different biases I_{IN} between the cases **A** and **B**.

Figure 6.15 shows the plots of OIP3 values versus I_{IN} for the testing cases **A** and **B**. OIP3 values of the case **A** are higher than those of the case **B** for the neglect of thermal effects in the case **A**. As $I_{IN} > 0.9$ mA, the OIP3 value

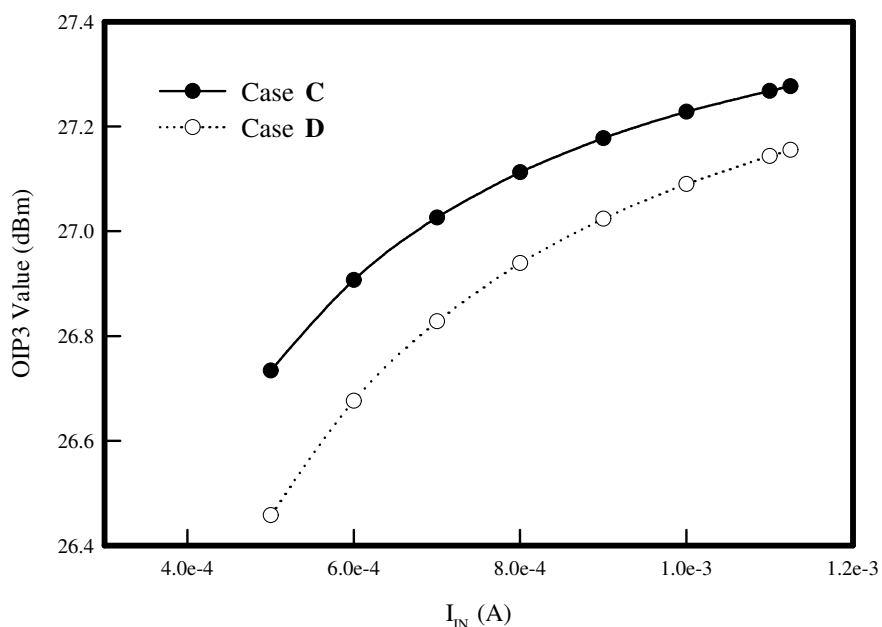


Figure 6.16: A comparison of OIP3 values of the whole device under different biases I_{IN} between the cases **C** and **D**.

begins to drop, and J_{CC} and T_J rise abruptly in the meantime, as shown in Fig. 6.13 and Fig. 6.14. The self-heating effect downgrades the two-tone linearity of HBT in the case **B**. We take the thermal coupling effect among fingers into account in the cases **C** and **D**. It is found that, as shown in Fig. 6.16, OIP3 value of the whole device varies smoothly with I_{IN} . Because there are two cold fingers (Fingers 1 and 3) in the cases **C** and **D**, the abrupt degradation for linearity in the case **B** can be prevented. In comparison between the cases **C** and **D**, OIP3 values in the case **D** are slightly lower than those in the case **C** for additional heating induced by the input RF signal. Furthermore, we

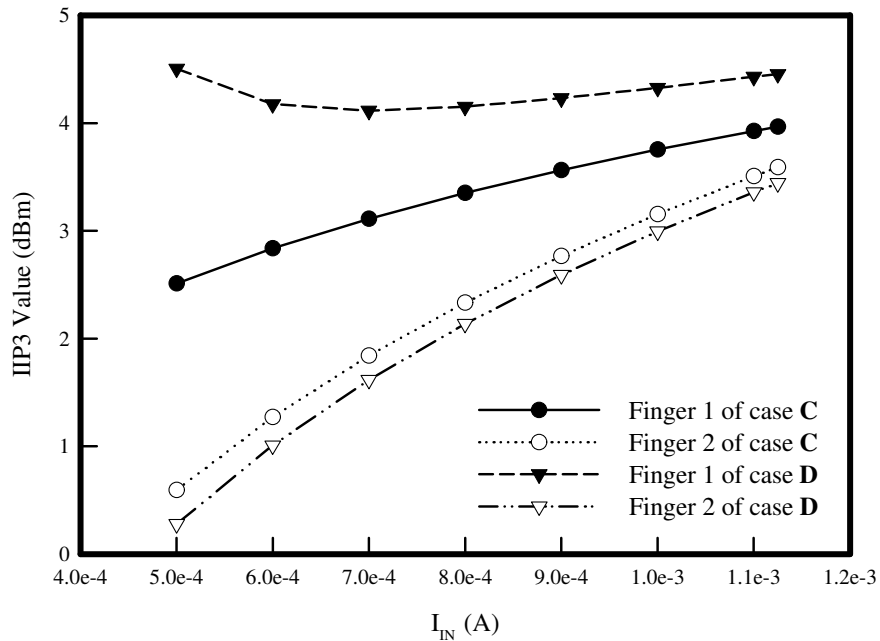


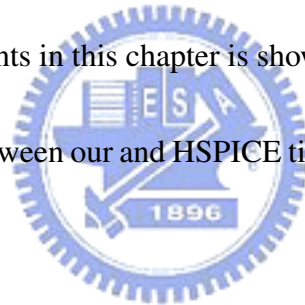
Figure 6.17: Plots of the input third-order intercept point (IIP3) values versus I_{IN} of the case **C** and **D**.

demonstrate the input third-order intercept point (IIP3) values for each finger in Fig. 6.17. It is reasonable that the colder finger (Finger 1) has better linearity. In comparison with the case **C**, the difference in linearity performance between fingers for the case **D** is enlarged by the additional heating. This expansion of difference among fingers lowers the OIP3 values of whole device as shown in Fig. 6.16.

6.4 Summary of This Chapter

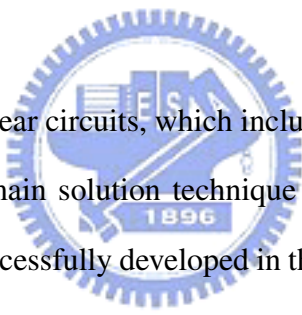
We demonstrated several two-tone intermodulation and power characteristics of HBTs in this chapter. From the comparison of OIP3 values between our time-domain and ADS harmonic balance solver, our developed kernel shows its capability to solve the steady-state circuit problem, which is not suitable for traditional time-domain circuit solver. Besides, as we introduce the thermal effects into the circuit simulation, the influence of device heating both on power and linearity performance has been simulated by our simulator. The itemized list of the contents in this chapter is shown as:

- the comparison between our and HSPICE time-domain solver in solving OIP3 values,
- the two-tone intermodulation distortion analysis computed by both our and ADS solver,
- the intermodulation distortion characteristic of an HBT as the self-heating been counted, and
- power and two-tone linearity characteristics of an multi-finger HBT with the consideration of thermal coupling effect.



Chapter 7

Summary and Suggestions



To solve the nonlinear circuits, which include active semiconductor devices, a time-domain solution technique based on the WR, MI, and RK methods has been successfully developed in this dissertation. With the MI technique, we have numerically demonstrated each decoupled circuit ODE converges monotonically in Chapter 3 and Appendix C. Compared with commercial simulators, such as HSPICE and ADS, our solution method has been presented to show its accuracy and efficiency when evaluated against the measurement data. The proposed method here is not only an alternative computational technique for the time-domain solution of circuit ODEs, but also can be generalized for high frequency circuit simulation including more and variant kinds of semiconductor transistors.

In this chapter, we briefly summarize the essentials of our work first. Then, in the last section, some suggestions are proposed to further improve our study

and give the goals of future work.

7.1 Summary

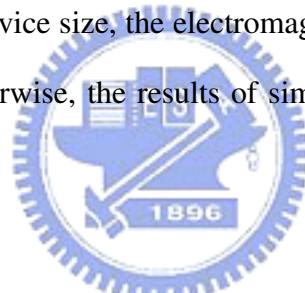
We have stated the following key points in this dissertation:

- **Chapter 1:** the overview of this dissertation,
- **Chapter 2:** the mathematical models, which include the GP model equations for an HBT and the nodal equations of the tested circuits,
- **Chapter 3:** computational techniques, characterization methodology and measurement procedure,
- **Chapter 4:** DC simulation and analysis of the HBTs,
- **Chapter 5:** the results of time-domain simulation and frequency domain analysis, and
- **Chapter 6:** the discussion of the intermodulation distortion and power characteristics.

In addition, we also present the appendices to complete the related issues of this dissertation.

- **Appendix A:** the equations of the MOSFET EKV model,
- **Appendix B:** the related EKV model simulation results, and
- **Appendix C:** the convergence properties of our developed numerical methods.

The major contribution of this work is the development of the transient analysis solver for high-frequency nonlinear circuit problems. The CAD prototype based on MI and Runge-Kutta methods has been applied to solving different kinds of semiconductor compact models. The simulation results shows the advantages of the developed solver in comparison between HSPICE, especially for the nonlinear circuits. We should emphasize that the proposed method only works when the KCL is valid. In other words, the limitation of the developed method is the operation frequency. Once the wave length of signal competes with the device size, the electromagnetic effects should be took into consideration. Otherwise, the results of simulation becomes physically meaningless.



7.2 Suggestions for Further Work

On the basis of the developed numerical solution techniques, the following suggestions are given for the future work:

1. automatically generate the circuit nodal equations with modified nodal analysis in the net list formation, such as .ps file of SPICE,
2. in the MI algorithm, utilize vector and matrix forms for unknown variables and linear/weak-nonlinear circuit elements,
3. accelerate the numerical solution methods by parallel computation techniques,

4. extend our method to more and newer semiconductor compact models,
5. replace the NI related part of the numerical solution methods for RF steady-state circuit problems, such as frequency-domain HB method, with the MI algorithm, and
6. combine the nonlinear circuit solver and parameter extraction algorithm, such as GA, to develop new compact models for modern semiconductor devices.



Bibliography

- [1] Christopher M. Snowden, *Semiconductor Device Modelling*, London: Springer-Verlag, 1989.
- [2] Behzad Razavi, *RF Microelectronics*, Prentice Hall PTR, 1998.
- [3] Thomas H. Lee, *The Design of CMOS Radio-Frequency Integrated Circuits*, Cambridge University Press, 1998.
- [4] Paul R. Gray, Paul J. Hurst, Stephen H. Lewis, and Robert G. Meyer, *Analysis and Design of Analog Integrated Circuits, 4th ed.*, New York: John Wiley & Sons, Inc., 2001.
- [5] L. Nagel, *SPICE2: A computer program to simulate semiconductor circuits*, Electron. Res. Lab., Univ. California at Berkeley, UCB/ERL M520, 1975.
- [6] T. Quarles, *The SPICE3 implementation guide*, Electron. Res. Lab., Univ. California at Berkeley, UCB/ERL M89/44, 1989.

- [7] K. Mayaram, D.C. Lee, S. Moinian, D.A. Rich, and J. Roychowdhury, "Computer-aided circuit analysis tools for RFIC simulation: algorithms, features, and limitations," *IEEE Transactions on Circuits and SystemsXII: Analoh and Digital Signal Processing*, vol. 47, no. 4, pp. 274-286, April 2000.
- [8] Kenneth S. Kundert, "Introduction to RF Simulation and Its Application," *IEEE Journal of Solid-State Circuits*, vol. 34, no. 9, pp. 1298-1319, Sept. 1999.
- [9] Paulo J. Rodrigues, *Computer-Aided Analysis of Nonlinear Microwave Circuits*, Artech House, Inc., 1998.
- [10] T.J. Aprille and T.N. Trick, "Steady-state analysis of nonlinear circuits with periodic inputs," *Proc. IEEE*, vol. 60, pp. 108-114, Jan. 1972.
- [11] T.J. Aprille and T.N. Trick, "A computer algorithm to determine the steady-state response of nonlinear oscillators," *IEEE Trans. Circuit Theory*, vol. CT-19, pp. 354-360, July 1972.
- [12] R. Telichevesky, K. Kundert, and J. White, "Efficient steady-state analysis based on matrix-free Krylov subspace methods," in *Proc. IEEE DAC*, pp. 480-484, 1995.
- [13] M. Nakhla and J. Vlach, "A piecewise harmonic balance technique for determination of the periodic response of nonlinear systems," *IEEE Trans. Circuits Syst.*, vol. CAS-23, pp. 85-91, Feb. 1976.

- [14] A. Ushida and L. Chua, "Frequency-domain analysis of nonlinear circuits driven by multi-tone signal," *IEEE Trans. Circuits Syst.*, vol. CAS-31, pp. 766-778, Sept. 1984.
- [15] K. Kundert and A. Sangiovanni-Vincentelli, "Simulation of nonlinear circuits in the frequency domain," *IEEE Trans. Computer-aided Design*, vol. CAD-5, pp. 521-535, Oct. 1986.
- [16] D. Long, R. Melville, K. Ashbu, and B. Horton, "Full-chip harmonic balance," in *Proc. IEEE CICC*, pp. 379-382, May 1997.
- [17] K. S. Kundert, J. K. White, and A. Sangiovanni-Vincentelli, *Steady-State Methods for Simulating Analog and Microwave Circuits*, Kluwer Academic Publisher, 1990.
- [18] Stephen A. Mass, *Nonlinear Microwave and RF Circuits, 2nd ed.*, Artech House, Inc., 2003.
- [19] Leon O. Chua, Charles A. Desoer, and Ernest S. Kuh., *Linear and non-linear circuits*, McGraw-Hill, 1987.
- [20] W.H. Press, S.A. Teukolsky, W.T. Vetterling, and B.P. Flannery, *Numerical Recipes in C++: the art of scientific computing, 2nd ed.*, Cambridge University Press, 2002.
- [21] Shoichiro Nakamura, *Applied Numerical Methods in C*, Prentice Hall, Inc., 1995.

- [22] K. Kundert, J. White, and A. Sangiovanni-Vincentelli, "A mixed frequency-time approach for distortion analysis of switching filter circuits," *IEEE J. Solid-State Circuits*, vol. 24, pp. 443-451, Apr. 1989.
- [23] J. Roychowdhury, "Analyzing circuits with widely-separated time scales using numerical PDE methods," *IEEE Trans. Circuits Syst. I*, May 1999.
- [24] L. Petzold, "An efficient numerical method for highly oscillatory ordinary differential equations," *SIAM J. Numer. Anal.*, vol. 18, pp. 455-479, June 1981.
- [25] K. Kundert, J. White, and A. Sangiovanni-Vincentelli, "An envelope-following method for the efficient transient simulation of switching power and filter circuits," in *Proc. ICCAD*, pp. 446-449, Nov. 1988.
- [26] E. Ngoya and R. Larcheveque, "Envelope transient analysis: A new method for the transient and steady-state analysis of microwave communication circuits and systems," in *IEEE MTT Symp. Dig.*, pp. 1365-1368, June 1996.
- [27] J. Roychowdhury, "MPDE methods for efficient analysis of wireless systems," in *Proc. IEEE CICC*, pp. 451-454, May 1998.
- [28] M. Okumura, T. Sugawara, and H. Tanimoto, "An efficient small-signal frequency analysis method for nonlinear circuits with two frequency

- excitations," *IEEE Trans. Computer-aided Design*, vol. 9, pp.225-235, Mar. 1990.
- [29] P. Wambacq, and W. Sansen, *Distortion Analysis of Analog Integrated Circuit*, Kluwer Academic Publisher, 1998.
- [30] E. Lelarsmee, A. Ruehli, and A. Sangiovanni-Vincentelli, "The waveform relaxation method for time-domain analysis of large scale integrated circuits," *IEEE Trans. on CAD of IC and Systems*, vol. CAD-1, pp. 131-145, July 1982.
- [31] H. K. Gummel, "A self-consistent iterative scheme for one-dimensional steady state transport calculations," *IEEE Trans. Electron Devices*, ED-11, pp. 455-465, 1964.
- [32] Vandewalle Stefan, *Parallel multigrid waveform relaxation for parabolic problems*, Teubner, 1993.
- [33] S. Heikkilä and V. Lakshmikantham, *Monotone iterative techniques for discontinuous nonlinear differential equations*, New York: Marcel Dekker, 1994.
- [34] C. V. Pao, *Nonlinear Parabolic and Elliptic Equations*, New York: Plenum Press, 1992.

- [35] Yiming Li, "A monotone iterative method for bipolar junction transistor circuit simulation," *WSEAS Transactions on Mathematics*, vol. 1, no. 4, pp.159-164, Oct. 2002.
- [36] Yiming Li, "A Parallel Monotone Iterative Method for the Numerical Solution of Multidimensional Semiconductor Poisson Equation," *Computer Physics Communications*, vol. 153, no. 3, pp. 359-372, July 2003.
- [37] C.-W. Ho, A. Ruehli, and P. Brennan, "The modified nodal approach to network analysis," *IEEE Trans. on Circuits and Systems*, vol. 22, pp. 504-509, June 1975.
- [38] Kenneth S. Kundert, *Spectre user's guide: a frequency domain simulator for nonlinear circuits*, EECS Industrial Liaison Program, Univ. California at Berkeley, Apr. 1987.
- [39] Kenneth S. Kundert, *The designer's guide to SPICE and SPECTRE*, Kluwer Academic Publisher, 1995.
- [40] Advanced Design System, ADS., Agilent Technologies. [Web resources: <http://eesof.tm.agilent.com/products/adsoview.html>]
- [41] Affirma Analog Artist circuit design environment, Cadence Design System. [Web resources: http://www.cadence.com/technology/custom/products/_artist.html]

- [42] S.M. Sze, *Physics of Semiconductor Devices, 2nd ed*, New York: John Wiley & Sons, Inc., 1981.
- [43] B. Bayraktaroglu and J. A. Higgins, "HBTs for microwave power applications," in *Current Trends in Heterojunction Bipolar Transistors*, M. F. Chang, Ed. Singapore: World Scientific, 1996.
- [44] M. Yanagihara, H. Sakai, Y. Ota, and A. Tamura, "High f_{max} Al-GaAs/GaAs HBT with L-shaped base electrode and its application to 50 GHz amplifier," *Solid-State Electron*, vol. 41, pp. 1615-1620, Oct. 1997.
- [45] N. Pan, J. Elliott, M. Knowles, D. P. Vu, K. Kishimoto, J. K. Twynam, H. Sato, M. T. Fresina, and G. E. Stillman, "High reliability InGaP/GaAs HBT," *IEEE Trans. Electron Devices*, vol. 19, pp. 115-117, April 1998.
- [46] T. Oka, K. Hirata, H. Suzuki, K. Ouchi, H. Uchiyama, T. Taniguchi, K. Mochizuki, and T. Nakamura, "High-speed small-scale InGaP/GaAs HBT technology and its application to integrated circuits," *IEEE Trans. Electron Devices*, vol. 48, pp. 2625-2630, Nov. 2001.
- [47] M. Sokolich, M.Y. Chen, D.H. Chow, Y. Royter, S. Thomas III, C.H. Feilds, D.A. Hitko, B. Shi, M. Montes, S.S. Bui, Y.K. Boegeman, A. Arthur, J. Duvall, R. Martinez, T. Hussain, R.D. Rajavel, J.C. Li, K. Elliott, and J.D. Thompson, "InP HBT integrated circuit technology with

- selectively implanted subcollector and regrown device layers," *IEEE Journal of Solid-State Circuits*, vol.39, pp. 1615-1621, Oct. 2004.
- [48] R.S. Burton and P. Dai, "Characterization and modeling of InGaP HBT low-frequency oscillations," *IEEE Trans. Electron Devices*, vol. 51, pp. 1033-1036, June 2004.
- [49] J. J. Ebers and J. L. Moll, "Large-signal behavior of junction transistors," *Proc. IRE*, vol. 42, pp. 1761-1772, Dec. 1954.
- [50] H. K. Gummel and H. C. Poon, "An integral charge control model of bipolar transistors," *Bell Syst. Tech. J.*, vol. 49, pp. 827-852, May 1970.
- [51] I.E. Getreu, *Modeling the Bipolar Transistor*, Elsevier, 1984.
- [52] William Liu, *Handbook of III-V Heterojunction Bipolar Transistor*, New York: John Wiley & Sons, Inc., 1998.
- [53] D. Berger, D. Cell, M. Schroter, M. Malorny, T. Zimmer, and B. Ardouin, "HICUM parameter extraction methodology for a single transistor geometry," in *Proceedings of Bipolar/BiCMOS Circuits and Technology Meeting*, pp. 116-119, 2002.
- [54] M. Schroter, S. Lehmann, H. Jiang, and S. Komarow, "HICUM/Level0 - a simplified compact bipolar transistor model," in *Proceedings of Bipolar/BiCMOS Circuits and Technology Meeting*, pp. 112-115, 2002.

- [55] M. Schroter, "Staying current with HICUM," *IEEE Circuits and Devices Magazine*, vol. 18, pp. 16-25, May 2002.
- [56] W.J. Kloosterman, J.A.M. Geelen, and D.B.M. Klaassen, "Efficient parameter extraction for the MEXTRAM model," in *Proceedings of Bipolar/BiCMOS Circuits and Technology Meeting*, pp. 70-73, 1995.
- [57] E. Sonmez, W. Durr, P. Abele, K.-B. Schad, and H. Schumacher, "Parameter extraction of SiGe HBTs for a scalable MEXTRAM model and performance verification by SiGe HBT MMIC active receive mixer design for 11 GHz," in *Topical Meeting on Integrated Circuits in RF Systems, Digest of Papers.*, pp. 159-162, 2000.
- [58] X. Cao, J. McMacken, K. Stiles, P. Layman, J.J. Liou, A. Ortiz-Conde, and S. Moinian, "Comparison of the new VBIC and conventional Gummel-Poon bipolar transistor models," *IEEE Trans. Electron Devices*, vol. 47, pp. 427-433, Feb. 2002.
- [59] B. Senapati and C.K. Maiti, "Advanced SPICE modelling of SiGe HBTs using VBIC model," *IEE Proceedings G- Circuits, Devices and Systems*, vol. 149, pp. 129-135, April 2002.
- [60] X. Cao, J. McMacken, K. Stiles, P. Layman, J.J. Liou, A. Sun, and S. Moinian, "Parameter extraction and optimization for new industry standard VBIC model," in *Second International Conference on Advanced Semiconductor Devices and Microsystems*, vol. 149, pp. 107-116, 1998.

- [61] Avant! Corp., *Star-Hspice Manual Volume II - Elements and Device Models*, Avant! Corp. and Avant! subsidiary, 1999.
- [62] W. Ryu, A.L.C. Wai, F. Wei, W.W. Lai, and J. Kim, "Over GHz low-power RF clock distribution for a multiprocessor digital system," in *Proc. IEEE Electronic Components and Technology Conf.*, pp. 133-140, 2001.
- [63] L. Dermentzoglou, A. Arapoyanni, and A. Pneumatikakis, "A direct conversion receiver analysis for multistandard wireless applications," in *Proc. IEEE The 10th Mediterranean Electrotechnical Conf.*, pp. 318-321, 2000.
- [64] Yiming Li, Chuen-Tsat Sun, and Cheng-Kai Chen, "A Floating-Point Based Evolutionary Algorithm for Model Parameters Extraction and Optimization in HBT Device Simulation," in *Advances in Soft Computing - Neural Networks and Soft Computing*, Edited by L. Rutkowski and J. Kacprzyk, Physica-Verlag, pp. 364-369, Jan. 2003.
- [65] W. Liu, "Transient response of junction temperature in power heterojunction bipolar transistors," *Jpn. J. Appl. Phys.*, vol. 32, pp. 5503-5507, 1993.
- [66] L. L. Liou, J. L. Ebel, and C. I. Huang, "Thermal effects on the characteristics of AlGaAs/GaAs heterojunction bipolar transistors using two-dimensional numerical simulation," *IEEE Trans. Electron Devices*, vol.

40, pp. 35-43, Jan. 1993.

- [67] J. J. Liou, L. L. Liou, and C. I. Huang, "Analytical model for the Al-GaAs/GaAs multiemitter finger HBT including self-heating and thermal coupling effects," *IEE Proc. Circuits, Devices and Systems*, vol. 141, pp. 469-475, Dec. 1994.
- [68] Y. Zhu, J. K. Twynam, M. Yagura, M. Hasegawa, T. Hasegawa, Y. Eguchi, Y. Amano, E. Suematsu, K. Sakuno, N. Matsumoto, H. Sato, and N. Hashizume, "Self-heating effect compensation in HBTs and its analysis and simulation," *IEEE Trans. Electron Devices*, vol. 48, pp. 2640-2646, Nov. 2001.
- [69] S. Heckmann, R. Sommet, J.-M. Nebus, J.-C. Jacquet, D. Floriot, P. Auxemery, and R. Quere, "Characterization and modeling of bias dependent breakdown and self-heating in GaInP/GaAs power HBT to improve high power amplifier design," *IEEE Trans. Microwave Theory Tech.*, vol. 50, pp. 2811-2819, Dec. 2002.
- [70] M. Rudolph, "Uniqueness problems in compact HBT models caused by thermal effects," *IEEE Trans. Microwave Theory Tech.*, vol. 52, pp. 1399-1403, May 2004.
- [71] C.-H. Liao, C.-P. Lee, N. L. Wang, and B. Lin, "Optimum Design for a Thermally stable multifinger power transistor," *IEEE Trans. Electron Devices*, vol. 49, pp. 902-908, May 2002.

- [72] C. H. Liao and C. P. Lee, "Optimum Design for a Thermally stable multifinger power transistor with temperature-dependent thermal conductivity," *IEEE Trans. Electron Devices*, vol. 49, pp. 909-915, May 2002.
- [73] P. M. Asbeck, H. Kobayashi, M. Iwamoto, G. Hanington, S. Nam, L. and E. Larson, "Augmented behavioral characterization for modeling the nonlinear response of power amplifiers," in *IEEE MTT-S Microwave Symp. Dig.*, pp. 135-138, 2002.
- [74] Y. Zhu, Q. Cai, R. Balasubramanian, and J. Gerber, "Multi-finger power HBT model for nonlinear circuit simulation," in *Proc. IEEE RAWCON*, pp. 129-132, 2001.
- [75] A. Samelis and D. Pavlidis, "Analysis of the large-signal characteristics of power heterojunction bipolar transistors exhibiting self-heating effects," *IEEE Trans. Microwave Theory Tech.*, vol. 45, pp. 534-542, Apr. 1997.
- [76] H.-M. Park and S. Hong, "A novel temperature-dependent large-signal model of heterojunction bipolar transistor with a unified approach for self-heating and ambient temperature effects," *IEEE Trans. Electron Devices*, vol. 49, pp. 2099-2106, Dec. 2002.
- [77] Kuen-Yu Huang, Yiming Li, and Chien-Ping Lee, "Computer simulation of multifinger heterojunction bipolar transistor with self-heating

and thermal coupling models,” *Microelectronic Engineering*, vol. 75, pp. 137-144, Aug. 2004.

[78] *BSIM3 MOSFET Model*, Device Group, Department of Electrical Engineering and Computer Sciences, University of California, Berkeley. [Web resources: <http://www-device.eecs.berkeley.edu/bsim3/late-news.html>]

[79] *BSIM4 MOSFET Model*, Device Group, Department of Electrical Engineering and Computer Sciences, University of California, Berkeley. [Web resources: <http://www-device.eecs.berkeley.edu/bsim3/bsim4.html>]

[80] C. Enz, F. Kruppenacher, E. Vittoz, “An analytical MOS transistor model valid in all regions of Operation and dedicated to low-voltage and low-current applications,” *Journal on Analog Integrated Circuits and Signal Processing*, Kluwer Academic Pub., pp.83-114, July 1995. [Web resources: <http://legwww.epfl.ch/ekv>]

[81] V. Lakshmikantham and S. Leela, *Differential and integral inequalities*, New York: Academic Press, 1968.

[82] Yiming Li, Kuen-Yu Huang, Cheng-Kai Chen, Chien-Ping Lee, “A Parallel Computational Technique for High Frequency HBT Circuit Simulation,” in *Technical Proceedings of 5th ACR/IEEE/SIAM International*

Conference on Modeling and Simulation of Microsystems (MSM 2002), April, pp. 376-379, 2002.

- [83] Kuen-Yu Huang, Yiming Li, C.-P. Lee, and S. M. Sze, "A computational efficient method for HBT intermodulation distortions and two-tone characteristics simulation," in *International Conference on Simulation of Semiconductor Processes and Devices, SISPAD*, pp. 226-229, 2001.
- [84] Kuen-Yu Huang, Yiming Li, and Chien-Ping Lee, "A time-domain approach to simulation and characterization of RF HBT two-tone intermodulation distortion," *IEEE Trans. Microwave Theory Tech.*, vol. 51, pp. 2055-2062, Oct. 2003.
- [85] Melanie Mitchell, *An Interoduction to Genetic Algorithms*, The MIT Press, 1998.
- [86] David E. Goldberg, *Genetic Algorithms in Search, Optimization, and Machine Learning*, Addison Wesley Longman, Inc., 17th Printing, March 1988.
- [87] K.F. Man, K.S. Tang, S. Kwong, and W.A. Halang, *Genetic Algorithm for Control and Signal Processing*, London: Springer Verlag, 1997.
- [88] R. Menozzi, A. Piazzzi, and F. Contini, "Small signal modeling for microwave FET linear circuits based on a genetic algorithm," *IEEE Trans. Circ. Syst. -I*, vol. 43, pp. 839-847, Oct. 1996.

- [89] D. R. Pehlke and D. Pavlidis, "Evaluation of the factors determining HBT high-frequency performance by direct analysis of S-parameter data," *IEEE Trans. Microwave Theory Techn.*, vol. 40, pp. 2367-2373, Dec. 1992.
- [90] W. M. Spears and K. De Jong, "On the Virtues of Parameterized Uniform Crossover," in *The Fourth International Conference on Genetic Algorithm*, pp. 230-236, 1991.
- [91] MATLAB 6.0, Natick, MA: The Mathworks, Inc. [Web resources: <http://www.mathworks.com>]
- [92] B. Li, and S. Prasad, "Harmonic and two-tone intermodulation distortion analyses of the inverted InGa/InAlAs/InP HBT," *IEEE Trans. Microwave Theory Techn.*, vol. 45, pp. 1135-1137, July 1997.
- [93] B. Troyanovsky, Z. Yu, and R. W. Dutton, "Physics-based simulation of nonlinear distortion in semiconductor devices using the harmonic balance method," *Comput. Methods Appl. Mech. Engrg.*, vol. 181, pp. 467-482, Jan. 2000.
- [94] J. Lee, W. Kim, Y. Kim, T. Rho, and B. Kim, "Intermodulation mechanism and linearization of AlGaAs/GaAs HBT's," *IEEE Trans. Microwave Theory Techn.*, vol. 45, pp. 2065-2072, Dec. 1997.

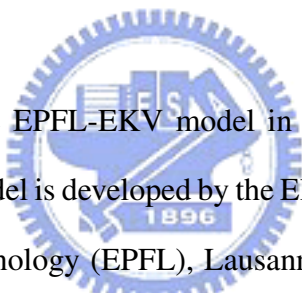
- [95] B. Li, and S. Prasad, "Intermodulation analysis of the collector-up In-GaAs/InAlAs/InP HBT using Volterra series," *IEEE Trans. Microwave Theory Tech.*, vol. 46, pp.132-1323, Sept. 1998.
- [96] M. Iwamoto, P.M. Asbeck, T.S. Low, C.P. Hutchinson, J.B. Cognata, X. Qin, L.H. Camnitz, and D.C. D'Avanzo, "Linearity characteristics of GaAs HBTs and the influence of collector design," *IEEE Trans. Microwave Theory Tech.*, vol. 48, pp. 2377-2388, Dec. 2000.
- [97] G. Niu, Q. Liang, J. D. Cressler, C. S. Webster, and D. L. Hareme, "Systematic analysis of RF distortion in SiGe HBT's," in *IEEE RFIC Symp. Dig.*, pp. 147-150, 2001.
- [98] Y. Wang, S. V. Cherepko, J. C. M. Hwang, F. Wang, and W. D. Jemison, "Asymmetry in intermodulation distortion of HBT power amplifiers," in *IEEE GaAs IC Symp. Tech. Dig.*, pp. 201-204, 2001.
- [99] Steve C. Cripps, *RF Power Amplifiers for Wireless Communications*, Artech House, Inc., 1999.
- [100] B. Hughes, A. Ferrero, and A. Cognata, "Accurate on-wafer power and harmonic measurement of microwave amplifiers and devices," in *Proc. IEEE Intl. Microwave Symp.*, pp. 1019-1022, 1992.
- [101] ATN Microwave, "A load-pull system with harmonic tuning," *Microwave Journal*, pp. 128-132, March 1996.

- [102] Thomas S. Laverghetta, *Morden Microwave Measurements and Techniques*, Artech House, Inc., 1988.
- [103] Chung-Er Huang, Chien-Ping Lee, Hsien-Chang Liang, and Ron-Ting Huang, "Critical spacing between emitter and base in InGaP Heterojunction Bipolar Transistor (HBTs)," *IEEE Electron Device Letters*, vol. 23, pp. 576-578, Oct. 2002.
- [104] Avant! Corp., *Star-Hspice Manual Volume III - MOSFET Models*, Avant! Corp. and Avant! subsidiary, 1999.



Appendix A

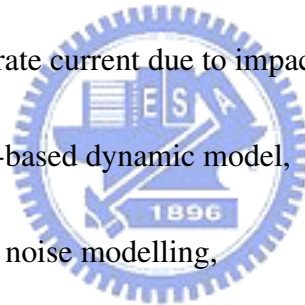
The MOSFET EKV Model



We describe the EPFL-EKV model in this appendix. EPFL-EKV MOSFET model is developed by the Electronics Laboratories, Swiss Federal Institute of Technology (EPFL), Lausanne, Switzerland [80]. It is a scalable and compact simulation model built on fundamental physical properties of the MOS structure. This model is dedicated to the design and simulation of low-voltage, low-current, analog, and mixed single circuit using submicron CMOS technology. The EKV MOSFET model is in principle formulated as a single expression, which preserves continuity of first and higher-order derivatives with respect to any terminal voltage, in the entire range of validity of the model. The EPFL-EKV MOSFET model version 2.6 includes modelling of the following effects:

1. basic geometrical and process related aspects such as oxide thickness, junction depth, and effective channel length/width,

2. effects of doping profile and substrate effect,
3. modelling of weak, moderate and strong inversion behaviors,
4. modelling of mobility effects due to vertical/lateral fields and velocity saturation,
5. short-channel effects such as channel-length modulation (CLM), source/drain charge-sharing (including for narrow channel widths), and reverse short channel effect (RSCE),
6. modelling of substrate current due to impact ionization,
7. quasi-static charge-based dynamic model,
8. thermal and flicker noise modelling,
9. a first-order non-quasistatic model for the transadmittances, and
10. short-distance geometry- and bias-dependent device matching.



The description concentrates on the intrinsic part of the MOSFET, and is intended to give model users the information on parameter handling and the actual equations used in the computer simulation. The extrinsic part of the MOSFET is handled as it is often made for other MOSFET models. The extrinsic model includes the series resistances of the source and drain diffusions, which are handled as external elements, as well as junction currents and capacitances. The complete model can be found in [104].

A.1 Equivalent Circuit

Figure A.1 represents a conventional intrinsic and extrinsic elements of the MOSFET device. The C_{gs} , C_{gd} , C_{gb} , C_{sb} , C_{db} , I_{DS} , and I_{DB} are the intrinsic EKV model elements. Others, like C_{gs0} , C_{gd0} , C_{gb0} , R_S , R_D , and R_G are the extrinsic part of a MOSFET device. The EKV model used in our case involves 29 parameters. A detail description of parameters and their unit are shown in Tab. A.1.



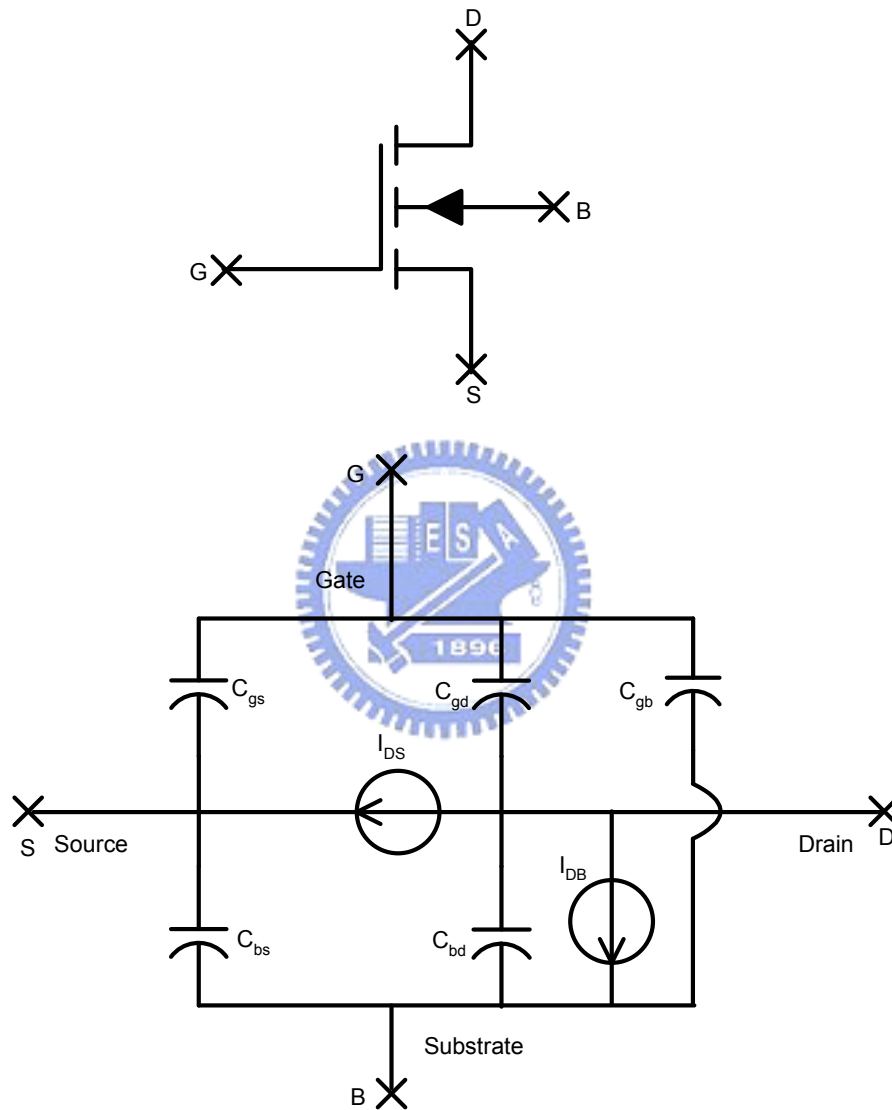


Figure A.1: A EKV MOSFET equivalent circuit for DC and transit analysis.

Name	Description	Unit
L	channel length	m
W	channel width	m
NP	parallel multiple device number	-
NS	series multiple device number	-
COX	gate oxide capacitance per unit area	F/m ²
XJ	junction depth	m
DW	channel width correction	m
DL	channel length correction	m
VTO	long-channel threshold voltage	V
GAMMA	body effect parameter	V ^{1/2}
PHI	bulk Fermi potential	V
KP	transconductance parameter	A/V ²
E0	mobility reduction coefficient	V/m
UCRIT	longitudinal critical field	V/m
LAMBDA	depletion length coefficient	-
WETA	narrow channel effect coefficient	-
LETA	short channel effect coefficient	-
Q0	reverse short channel effect peak charge density	As/m ²
LK	reverse short channel effect characteristic length	m
IBA	first impact ionization coefficient	1/m
IBB	second impact ionization coefficient	V/m
IBN	saturation voltage factor for impact ionization	-
TCV	threshold voltage temperature coefficient	V/K
BEX	mobility temperature exponent	-
UCEX	longitudinal critical field temperature exponent	-
IBBT	temperature coefficient for IBB	1/K
AVTO	area related threshold voltage mismatch parameter	V · m
AKP	area related gain mismatch parameter	m
AGAMMA	area related body effect mismatch parameter	V ^{1/2} m

Table A.1: The MOSFET EKV compact model parameters.

A.2 Model Equations

In order to implement the EKV model to perform the sub-micron MOSFET DC and time-domain circuit simulation, we first write the main of model equations. The drain to source current (I_{DS}) is the most important part in a MOSFET model. It is a single equation, valid in all operation region: weak inversion, moderate inversion, strong inversion, no-saturation, and saturation. Therefore, it is not only continuous but also continuously differentiable among all operational regions.

$$I_{DS} = I_S \cdot (i_f - i'_r). \quad (\text{A.1})$$

Subject to Eq. (A.1), the transconductances are obtained through derivation of Eq. (A.1) by V_G , V_S , and V_D .

$$g_{mg} \equiv \frac{\partial I_{DS}}{\partial V_G}. \quad (\text{A.2})$$

$$g_{ms} \equiv \frac{\partial I_{DS}}{\partial V_S}. \quad (\text{A.3})$$

$$g_{md} \equiv \frac{\partial I_{DS}}{\partial V_D}. \quad (\text{A.4})$$

The specific current is:

$$I_S = 2n\beta V_t^2, \quad (\text{A.5})$$

where V_t is thermal voltage. The i_f and i'_r are the forward normalized current and reverse normalized current.

$$i_f = F \left[\frac{V_P - V_S}{V_t} \right]. \quad (\text{A.6})$$

$$i'_r = F \left[\frac{V_P - V_{ds} - V_S - \sqrt{V_{DSS}'^2 + \Delta V^2} + \sqrt{(V_{ds} - V_{DSS}')^2 + \Delta V^2}}{V_t} \right]. \quad (\text{A.7})$$

The function $F(v)$ is a large-signal interpolation function relating the normalized currents to the normalized voltages. The large-signal interpolation function can be stated as follows:

$$y = \sqrt{0.25 + i} - 0.5, \quad \text{and} \quad (\text{A.8})$$

$$v = 2y + \ln(y). \quad (\text{A.9})$$

The pinch-off voltage V_P is formulated as follows:

$$V_P = \begin{cases} V_G' - \text{PHI} - \gamma' \cdot \left(\sqrt{V_G' + \left(\frac{\gamma'}{2}\right)^2} - \frac{\gamma'}{2} \right) & \text{for } V_G' > 0 \\ -\text{PHI} & \text{for } V_G' \leq 0. \end{cases} \quad (\text{A.10})$$

The parameter PHI is the bulk Fermi potential.

ΔV is subject to the channel-length modulation and the related formulas are shown below:

$$\Delta V = 4 \cdot V_t \cdot \sqrt{\text{LAMBDA} \cdot \left(\sqrt{i_f} - \frac{V_{DSS}}{V_t} \right) + \frac{1}{64}}, \quad (\text{A.11})$$

$$V_{ip} = \sqrt{V_{DSS}'^2 + \Delta V^2} - \sqrt{(V_{ds} - V_{DSS}')^2 + \Delta V^2}, \quad (\text{A.12})$$

$$V_{ds} = \frac{V_D - V_S}{2}, \quad (\text{A.13})$$

$$\Delta L = \text{LAMBDA} \cdot L_C \cdot \ln \left(1 + \frac{V_{ds} - V_{ip}}{L_C \cdot \text{UCRIT}} \right), \quad \text{and} \quad (\text{A.14})$$

$$L_C = \sqrt{\frac{\epsilon_{si}}{\text{COX}}} \cdot \text{XJ}. \quad (\text{A.15})$$

Velocity saturation voltage V_{DSS} and drain-to-source saturation voltage V'_{DSS} is represented in the following form:

$$V_C = \text{UCRIT} \cdot \text{NS} \cdot L_{eff} , \quad (\text{A.16})$$

$$V_{DSS} = V_C \cdot \left[\sqrt{\frac{1}{4} + \frac{V_t}{V_C} \cdot \sqrt{i_f}} - \frac{1}{2} \right] , \quad \text{and} \quad (\text{A.17})$$

$$V'_{DSS} = V_C \cdot \left[\sqrt{\frac{1}{4} + \frac{V_t}{V_C} \cdot \left(\sqrt{i_f} - \frac{3}{4} \ln(i_f) \right)} - \frac{1}{2} \right] + V_t \cdot \left[\ln\left(\frac{V_C}{2V_t}\right) - 0.6 \right] . \quad (\text{A.18})$$

The reverse short-channel effect(RSCE) is formulated as follows:

$$\Delta V_{RSCE} = \frac{2 \cdot Q_0}{\text{COX}} \frac{1}{\left[1 + \frac{1}{2} \cdot \left(\xi + \sqrt{\xi^2 + C_\varepsilon} \right) \right]^2} , \quad (\text{A.19})$$

$$\xi = C_A \cdot \left(10 \cdot \frac{L_{eff}}{\text{LK}} - 1 \right) , \quad (\text{A.20})$$

$$C_\varepsilon = 4 \cdot (22 \times 10^{-3})^2 , \quad \text{and} \quad (\text{A.21})$$

$$C_A = 0.028 . \quad (\text{A.22})$$

LK, COX, and Q0 are model parameters.

Effective gate voltage including RSCE is shown as:

$$V'_G = V_G - \text{VTO}_a - \Delta V_{RSCE} + \text{PHI} + \text{GAMMA}_a \sqrt{\text{PHI}} . \quad (\text{A.23})$$

The effective channel length and width are modelled as:

$$W_{eff} = W + DW , \quad \text{and} \quad (\text{A.24})$$

$$L_{eff} = L + DL . \quad (\text{A.25})$$

Pinch-off voltage for narrow-channel effect is shown in the following formula:

$$V_{P0} = \begin{cases} V'_G - \text{PHI} - \text{GAMMA}_a \cdot \\ \left(\sqrt{V'_G + \left(\frac{\text{GAMMA}_a}{2}\right)^2} - \frac{\text{GAMMA}_a}{2} \right) & \text{for } V'_G > 0 \\ -\text{PHI} & \text{for } V'_G \leq 0. \end{cases} \quad (\text{A.26})$$

The effective substrate factors accounting for charge-sharing are:

$$V'_S = \frac{1}{2} \cdot \left[V_S + \text{PHI} + \sqrt{(V_S + \text{PHI})^2 + 4(V_t)^2} \right], \quad \text{and} \quad (\text{A.27})$$

$$V'_D = \frac{1}{2} \cdot \left[V_D + \text{PHI} + \sqrt{(V_D + \text{PHI})^2 + 4(V_t)^2} \right]. \quad (\text{A.28})$$

Pinch-off voltage including short and narrow channel effects is written as:

$$V_P = \begin{cases} V'_G - \text{PHI} - \gamma' \cdot \left(\sqrt{V'_G + \left(\frac{\gamma'}{2}\right)^2} - \frac{\gamma'}{2} \right) & \text{for } V'_G > 0 \\ -\text{PHI} & \text{for } V'_G \leq 0, \end{cases} \quad (\text{A.29})$$

where

$$\gamma' = \frac{1}{2} \cdot \left(\gamma^\circ + \sqrt{\gamma^{\circ 2} + 0.1 \cdot V_t} \right), \quad \text{and} \quad (\text{A.30})$$

$$\gamma^\circ = \text{GAMMA}_a - \frac{\varepsilon_{si}}{\text{COX}} \cdot \left[\frac{\text{LETA}}{L_{eff}} \cdot \left(\sqrt{V'_S} + \sqrt{V'_D} \right) - \frac{3 \cdot \text{WETA}}{W_{eff}} \cdot \sqrt{V_{P0} + \text{PHI}} \right]. \quad (\text{A.31})$$

The pinch-off voltage accounts for channel doping effects such as threshold voltage and substrate effect. For long channel devices, V_P is a function of gate voltage. However, for short channel devices, V_P becomes a function of gate, source and drain voltage due to the charge-sharing effect.

The slope factor, which is primarily a function of gate voltage, is linked to the weak inversion slope.

$$n = 1 + \frac{\text{GAMMA}_a}{2 \cdot \sqrt{V_P + \text{PHI} + 4V_t}} . \quad (\text{A.32})$$

Transconductance factor due to the vertical field is shown as:

$$\beta = \frac{\beta_0}{1 + \frac{\text{COX}}{\text{E0} \cdot \epsilon_{si}} \cdot V_t \cdot |q_B + \eta \cdot q_I|} , \quad (\text{A.33})$$

where

$$\beta_0 = \text{KP}_a \cdot \frac{\text{NP} \cdot W_{eff}}{L_{eq}} , \quad (\text{A.34})$$

$$\beta'_0 = \beta_0 \cdot \left(1 + \frac{\text{COX}}{\text{E0} \cdot \epsilon_{si}} \cdot q_{B0} \right) , \quad (\text{A.35})$$

$$q_{B0} = \text{GAMMA}_a \cdot \sqrt{\text{PHI}} , \quad \text{and} \quad (\text{A.36})$$

$$\eta = \begin{cases} \frac{1}{2} & \text{for NMOS} \\ \frac{1}{3} & \text{for PMOS} . \end{cases} \quad (\text{A.37})$$

Equivalent channel length including channel-length modulation and velocity saturation is:

$$L_{eq} = \frac{1}{2} \cdot \left(L' + \sqrt{L'^2 + L_{min}^2} \right) , \quad (\text{A.38})$$

where

$$L' = \text{NS} \cdot L_{eff} - \Delta L + \frac{V_{ds} + V_{ip}}{\text{UCRIT}} , \quad \text{and} \quad (\text{A.39})$$

$$L_{min} = \text{NS} \cdot \frac{L_{eff}}{10} . \quad (\text{A.40})$$

Both the charged-based model for transcapacitances, allowing charge-conservation during transit analysis, and the simpler capacitances based model are shown

as follows:

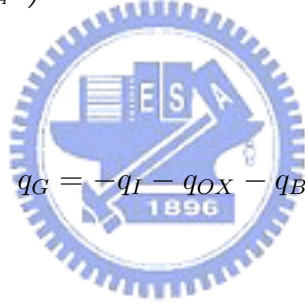
$$n_q = 1 + \frac{\text{GAMMA}_a}{2 \cdot \sqrt{V_P + \text{PHI} + 10^{-6}}}, \quad (\text{A.41})$$

$$q_D = -n_q \cdot \left(\frac{4}{15} \cdot \frac{3x_r^3 + 6x_r^2x_f + 4x_rx_f^2 + 2x_f^3}{(x_f + x_r)^2} - \frac{1}{2} \right), \quad (\text{A.42})$$

$$q_S = -n_q \cdot \left(\frac{4}{15} \cdot \frac{3x_f^3 + 6x_f^2x_r + 4x_fx_r^2 + 2x_r^3}{(x_f + x_r)^2} - \frac{1}{2} \right), \quad (\text{A.43})$$

$$q_I = q_S + q_D, \quad (\text{A.44})$$

$$q_B = \begin{cases} \left(-\text{GAMMA}_a \cdot \sqrt{V_P + \text{PHI} + 10^{-6}} \right) \\ \cdot \frac{1}{V_t} - \left(\frac{n_q - 1}{n_q} \right) \cdot q_I & \text{for } V_G' > 0 \\ -V_G' \cdot \frac{1}{V_t} & \text{for } V_G' \leq 0, \text{ and} \end{cases} \quad (\text{A.45})$$



$$q_G = -q_I - q_{OX} - q_B. \quad (\text{A.46})$$

We note that:

$$x_r = \sqrt{0.25 + i_r} \quad \text{and} \quad (\text{A.47})$$

$$x_f = \sqrt{0.25 + i_f}. \quad (\text{A.48})$$

The charge conservation among the four nodes of the MOSFET is expressed by the above equations. Besides, the total charges are :

$$Q_{(I,B,D,S,G)} = C_{ox} \cdot V_t \cdot q_{(I,B,D,S,G)}, \quad (\text{A.49})$$

where

$$C_{ox} = COX \cdot NP \cdot W_{eff} \cdot NS \cdot L_{eff}. \quad (\text{A.50})$$

We note that the above equations is the main of the EKV model. The complete EKV model equations can be found in [104].

Appendix B

EKV Model Simulation Results

In order to show the developed method can be applied to MOS-like compact model. The simulations for EKV2.6 model will be presented in this appendix. First, we calculate intermodulation distortion characteristic with two-tone input excitation in time-domain. The fundamental frequencies, f_1 and f_2 are 1.71 GHz and 1.89 GHz, respectively. Then, with the time domain results, we calculate the spectrums of the output power by the FFT directly. Using the FFT results, we can denote the IM3 products at $2f_2 - f_1$ and $2f_1 - f_2$, named HI-IM3 and LO-IM3. Finally, a low noise amplifier (LNA) circuit with two MOSFETs has been simulated with the proposed method. We also compare the results of our solver with the outcome of HSPICE in these simulations. Note that the EKV2.6 model is the Level 55 in HSPICE simulator.

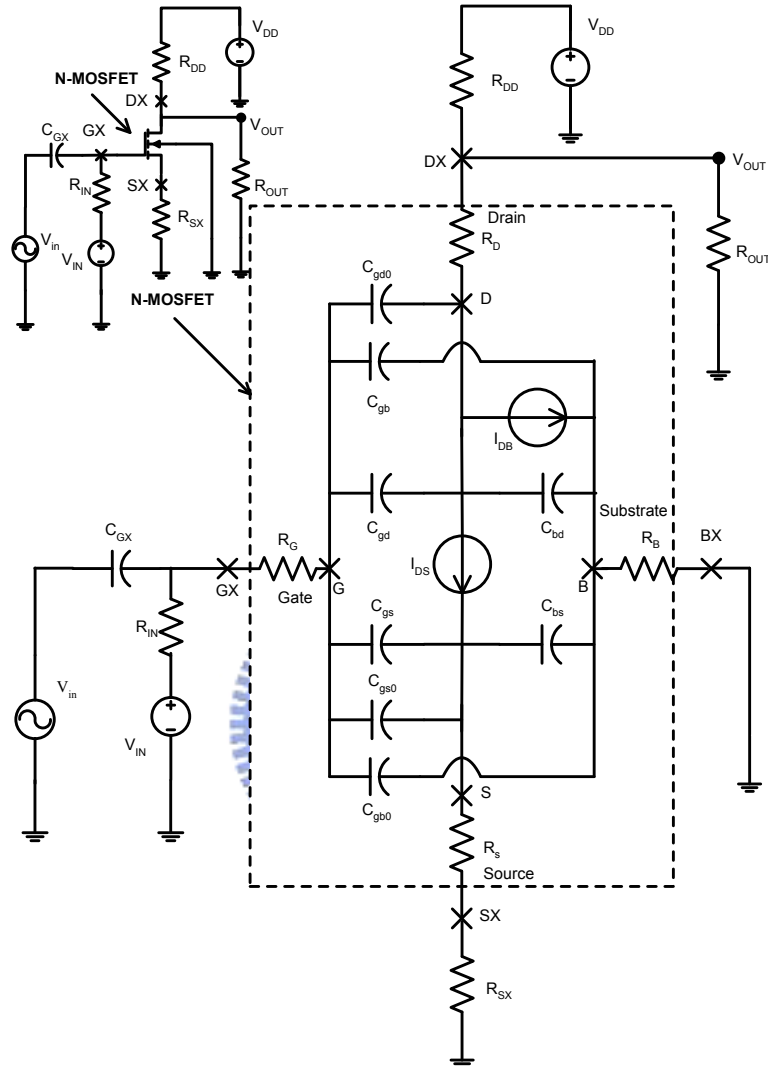


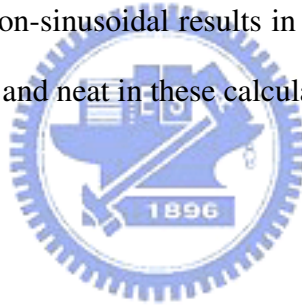
Figure B.1: A MOSFET circuit for large signal time domain analysis and the EKV2.6 large signal model for MOSFET simulation.

B.1 Time Domain Simulation Results

In this section, we demonstrate the computed time domain results. As shown in Fig. B.1, the input signal V_{IN} is the DC bias and the expression of the two-tone input signal V_{in} is written as:

$$V_{in} = V_m \sin(2\pi f_1 t) + V_m \sin(2\pi f_2 t), \quad (\text{B.1})$$

where the $V_m = 0.005$ V is the amplitude per tone, and the frequency f_1 and f_2 are 1.71 GHz and 1.89 GHz, respectively. With the computed periodic results, we remark the good repetition of the output signal as shown in Fig. B.2. Figure B.3 shows the HSPICE results of the time-domain simulation. Contrasting with the unstable output waveform of HSPICE, the proposed simulator shows the stability in the large scale time-domain calculation. In these figures, we can find the difference between two simulators especially at the time intervals 2.5 ns – 3.5 ns and 8.0 ns – 9.0 ns. The HSPICE simulation shows non-smooth and non-sinusoidal results in these intervals. Meanwhile, our results are still stable and neat in these calculation.



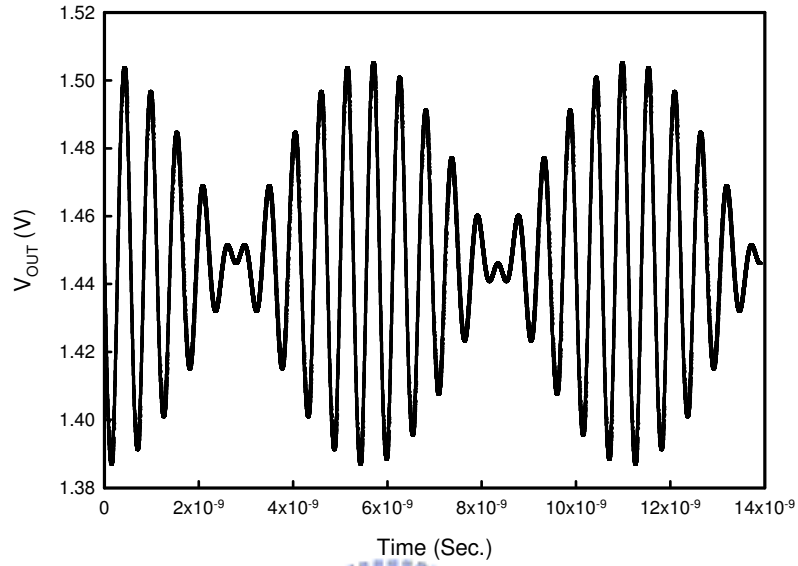


Figure B.2: A plot of V_{OUT} versus time, which is simulated by our method.

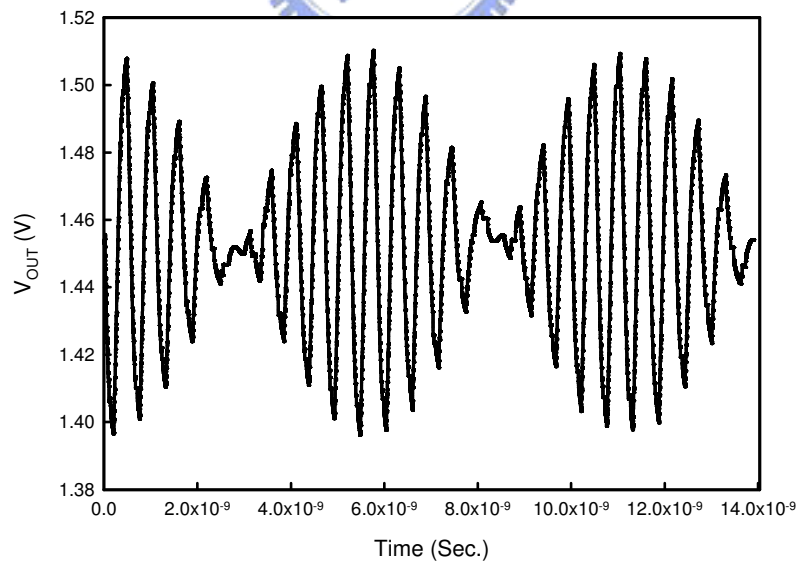
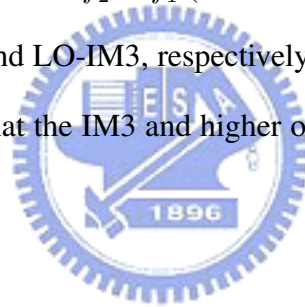


Figure B.3: A plot of V_{OUT} versus time, which is simulated by HSPICE simulator.

B.2 Spectrum Results After FFT

With the time domain results, we calculate the spectrum of the output power by the FFT directly. First, we demonstrate the corresponding spectrums of the figures B.2 and B.3 in the figures B.4 and B.5, respectively. In computing Fig. B.4, our simulated data is between 0 ns and 11.12 ns (20 periods at the center frequency, the center frequency is 1.8 GHz). Figure B.5 shows the FFT results with the computed HSPICE time-domain data with the same time periods. The IM3 products at $2f_2 - f_1$ (2.07 GHz) and $2f_1 - f_2$ (1.53 GHz) are denoted as HI-IM3 and LO-IM3, respectively. In Fig. B.5, the noise level is comparative high so that the IM3 and higher order products are difficult to recognize.



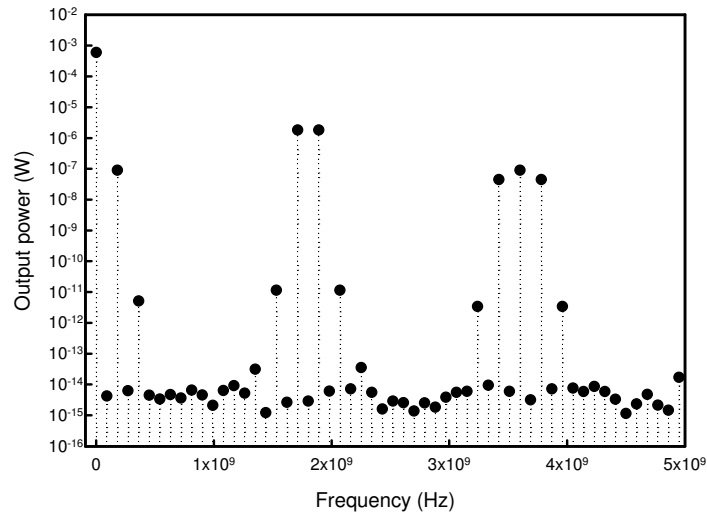


Figure B.4: The spectrum of output power calculated with time-domain data of our method.

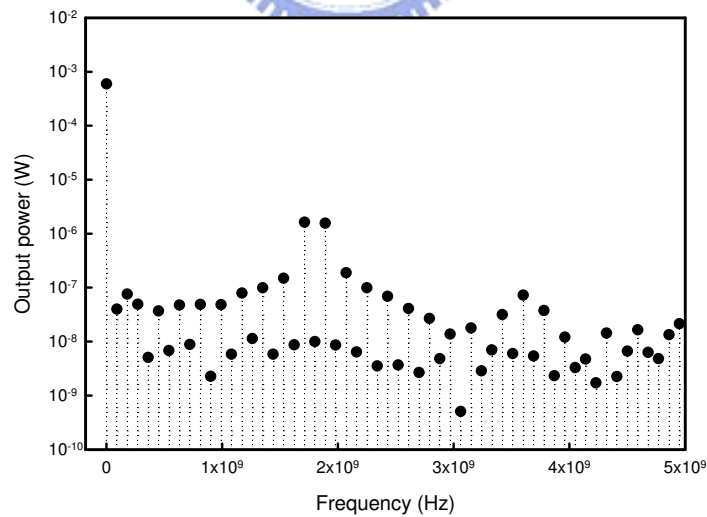
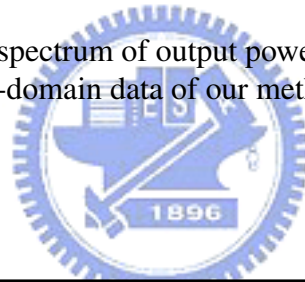


Figure B.5: The spectrum of output power calculated with HSPICE time-domain data.

Figure B.6 shows our simulated output power at the fundamental frequencies and the IM3 products versus the corresponding input power. Figure B.7 shows the output power simulated by HSPICE. As shown in Fig. B.6, our calculation slopes are 0.99 and 2.8, which are near to the theoretical value 1.0 and 3.0, respectively. We note that, with the developed solver, the HI-IM3 and LO-IM3 are close enough and the HI-IM3 and LO-IM3 have the same OIP3 value about 1.59 dBm. Unfortunately, as shown in Fig. B.7, the slopes of the fundamental frequencies and the IM3 products from the HSPICE results equal 1.398 and 1.333, respectively. It leads to a non-predictable OIP3 value because of the non-smooth HSPICE results in time-domain simulation.



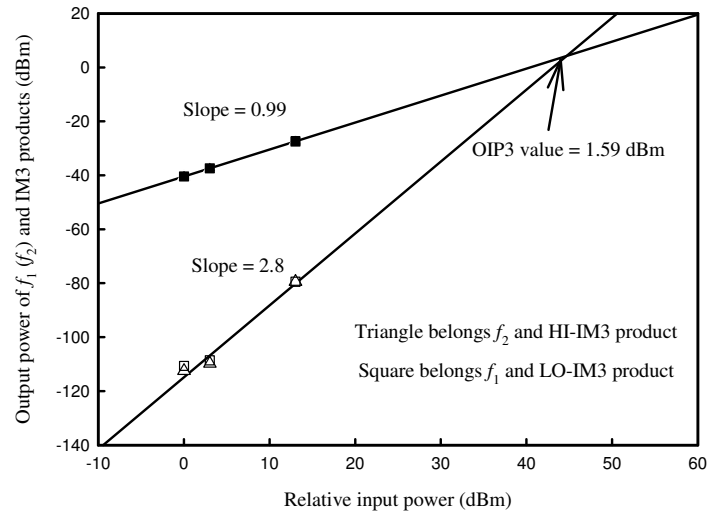


Figure B.6: A plot of the output power at fundamental frequencies and IM3 products, simulated by our method.

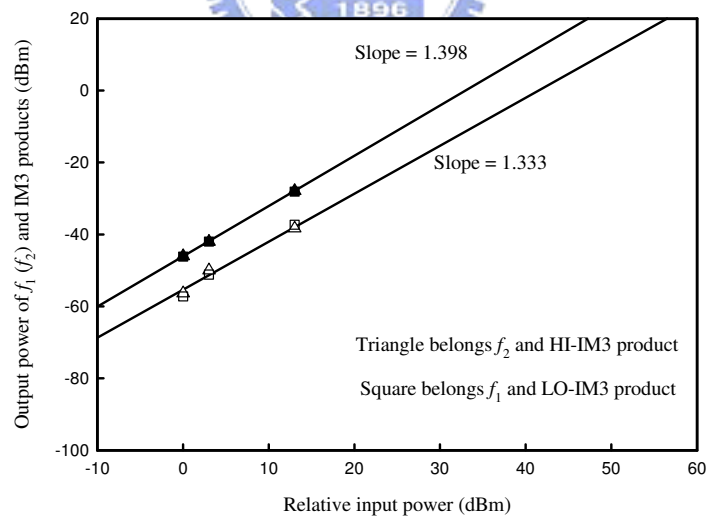


Figure B.7: A plot of the output power at fundamental frequencies and IM3 products, simulated by HSPICE.

B.3 Simulation of a Low Noise Amplifier

To verify the computational accuracy and efficiency of the developed numerical scheme with more MOSFET transistors, a 2-MOSFETs low noise amplifier (LNA) with 2.4 GHz input signal is simulated. Figure B.8 shows the simulated RF low noise amplifier (LNA) circuit. The channel length of these two MOSFETs are $0.24 \mu\text{m}$, and the width of them are $250 \mu\text{m}$ and $110 \mu\text{m}$, respectively. The input signal V_{IN} is the DC bias and the expression of the single-tone input signal V_{in} is written as:

$$V_{\text{in}} = V_{\text{m}} \sin(2\pi f_1 t), \quad (\text{B.2})$$

where $V_{\text{m}} = 0.005 \text{ V}$ is the amplitude of the input excitation, and f_1 equals 2.4 GHz. Figures B.9-B.10 show the simulated results of this LNA. As shown in Fig. B.9, we find the output signal has good repetition. Figure B.10 shows the time-domain simulated result of HSPICE. We can observe that, in the HSPICE calculation, there are some unstable outcomes at the peaks of the signal. With the time-domain results, after the FFT, Figs. B.11 and B.12 show the spectrum of V_{OUT} . In the spectrum of our results, the fundamental frequencies and corresponding harmonics can easily be found. However, the results of HSPICE as shown in Fig. B.12, the fundamental frequency is underestimated and the even order harmonics have vanished. The unstable time-domain calculation of HSPICE induces erroneous spectrum.

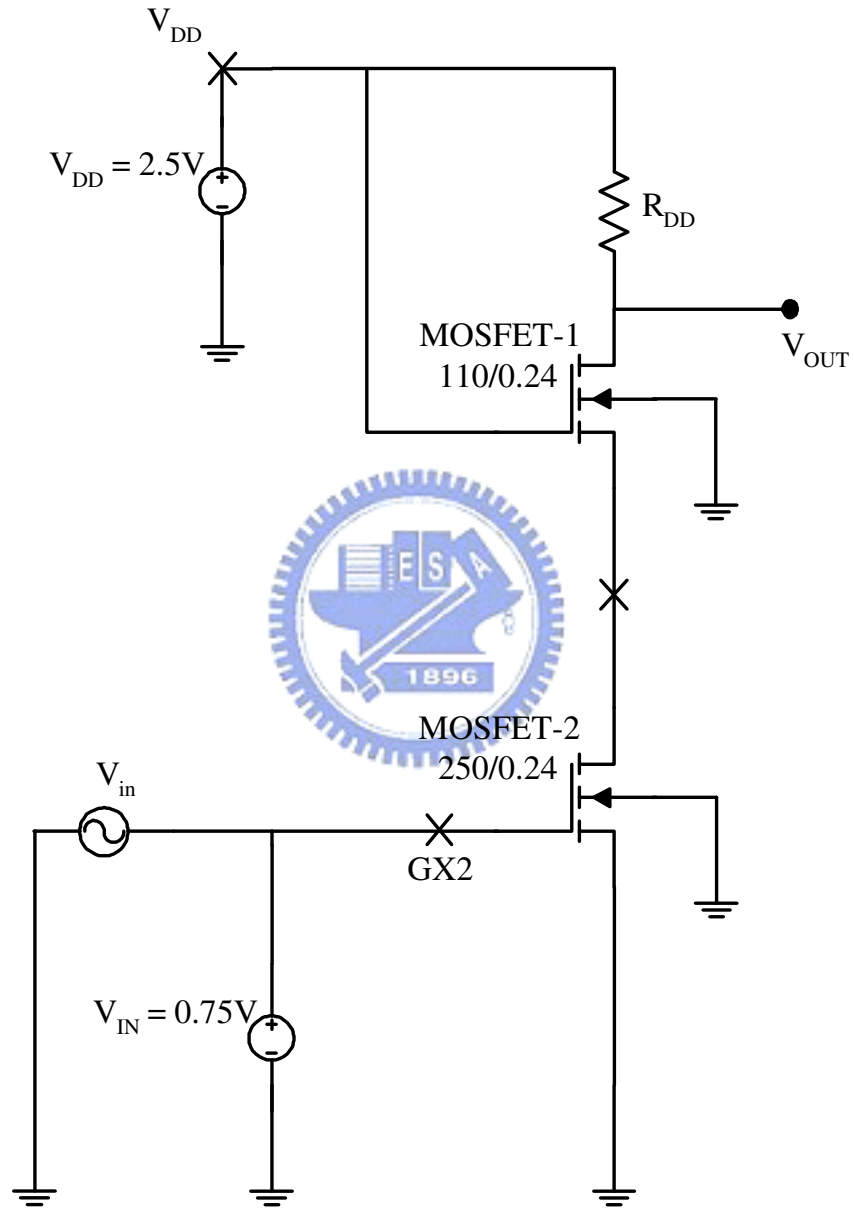


Figure B.8: The circuit of a low noise amplifier (LNA).

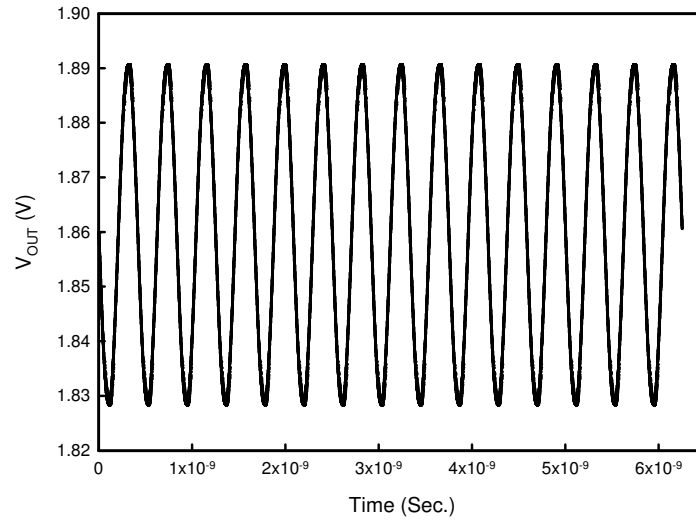


Figure B.9: A plot of V_{OUT} for an LNA simulated by the developed method.

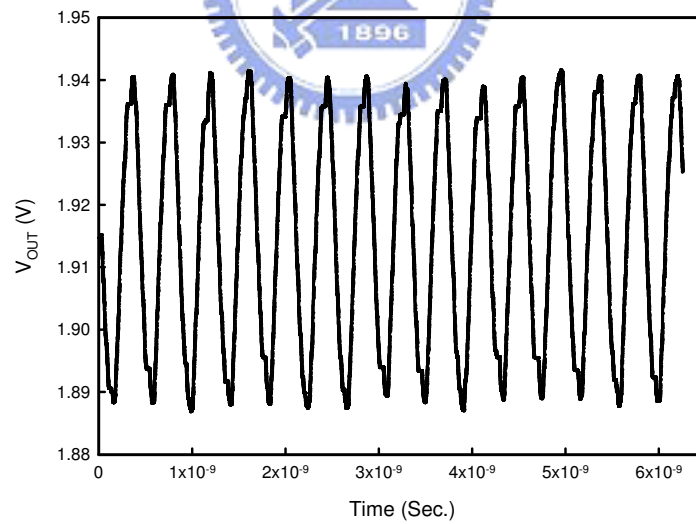


Figure B.10: A plot of V_{OUT} for an LNA simulated by HSPICE.

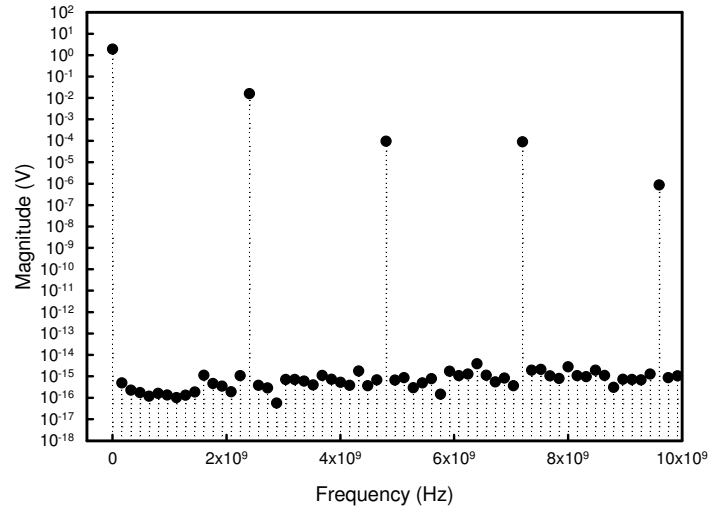


Figure B.11: The spectrum of V_{OUT} simulated by the developed method.

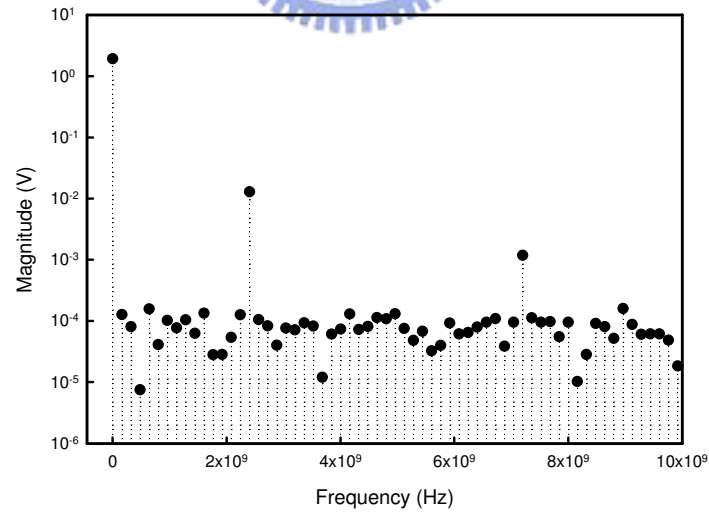
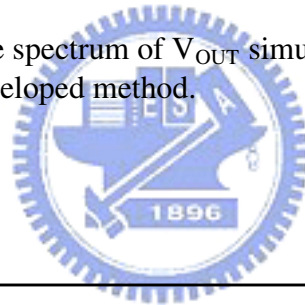


Figure B.12: The spectrum of V_{OUT} simulated by HSPICE simulator.

Appendix C

Convergence Properties

The additional remark about the convergence properties of our developed algorithms is given in this appendix. We demonstrate the maximum norm error versus the number of iterative loops to characterize the convergence properties of numerical methods of this study; which include the DC, time-domain and electrical-thermal feedback solution algorithms.

C.1 Convergence of Time-Domain Solution Algorithm

According to algorithm in Sec. 3.1.2 and the circuit in Fig. 2.2, we record the maximum norm errors of all unknown variables in each outer iteration. Figure C.1 shows the achieved convergence properties on the proposed method, where the $V_{IN} = 1.42 \text{ V}$ and $V_{CC} = 5 \text{ V}$. In our calculation experience, a convergence criterion for all quantities (maximum norm error $< 10^{-10}$ and 10^{-7} for the inner and the overall outer loops) can be reached by 8 – 10 MI inner loops and 25 – 30 outer loops, respectively. All computed unknowns have the

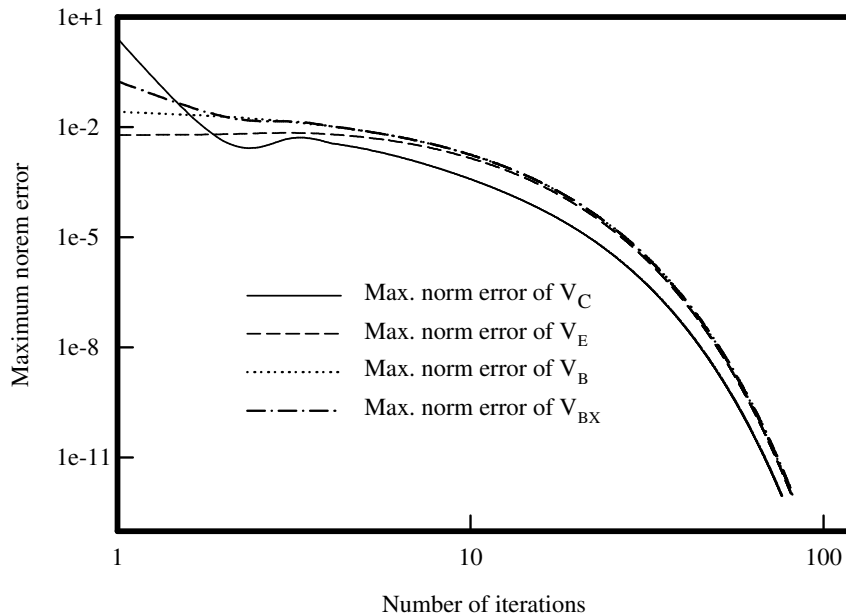


Figure C.1: The maximum norm error of all computed unknowns versus number of the outer iterations.

same strictly convergent behavior.

C.2 Convergence Properties with Thermal Effect

Figure C.2 shows the convergence properties of DC simulation with respect to the algorithms discussed in Sec. 3.1.1 and Sec. 3.1.4. We simulate the circuit shown in Fig. 4.9 with bias condition, $V_{CC} = 5.0$ V and $I_{IN} = 0.5$ mA. Though the maximum norm error of the algorithm with thermal effect is larger than that without thermal effect at the beginning, the norm errors decrease to the same level after 36 iterations. Our method could maintain its accuracy even with the consideration of thermal effect.

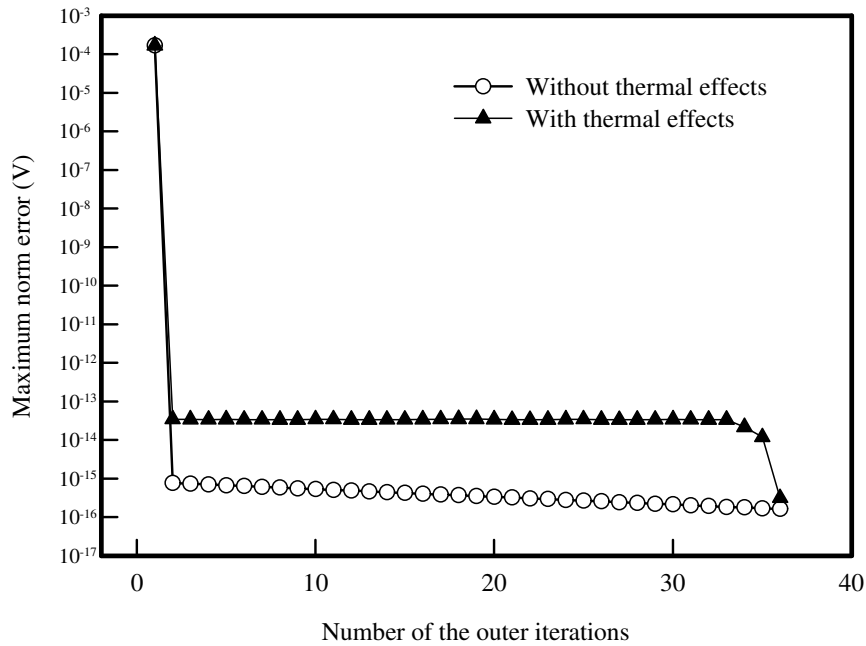


Figure C.2: The maximum norm error of the DC simulation versus number of the outer iterations.

For the time-domain solution and electrical-thermal feedback algorithms (see also Sec. 3.1.2 and Sec. 3.1.4), we give the convergent comparison between the simulations with and without thermal effect at different types of time steps. We show the illustration of the simulated time steps, which are chosen for the comparison in input excitation waveform (Fig. C.3). In these time steps, the values of the differential terms are quite distinct. The tested circuit is shown in Fig. 2.3 and the biases are set to be $V_{CC} = 5.0$ V and $I_{IN} = 0.5$ mA.

As shown in figures C.4 and C.5, the convergence properties of maximum

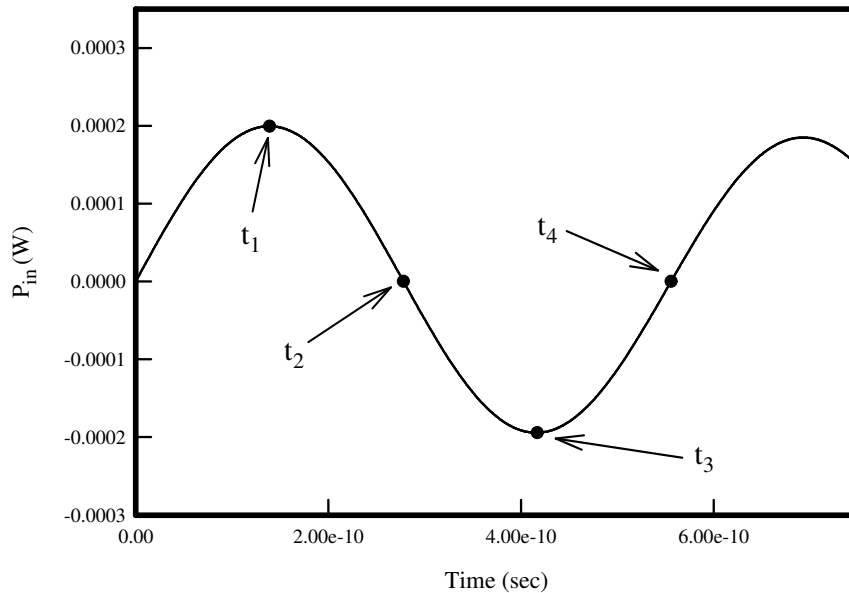


Figure C.3: The illustration of the chosen time steps for the convergence comparison.

norm error for algorithms including electrical-thermal feedback equations are similar to those without thermal effect. The additional electrical-thermal interactive algorithm influences the convergent characteristics slightly. Besides, at time steps t_2 and t_4 , the norm errors converge slower than those at time steps t_1 and t_3 ; which is because the values of differential terms vary rapidly at t_2 and t_4 .

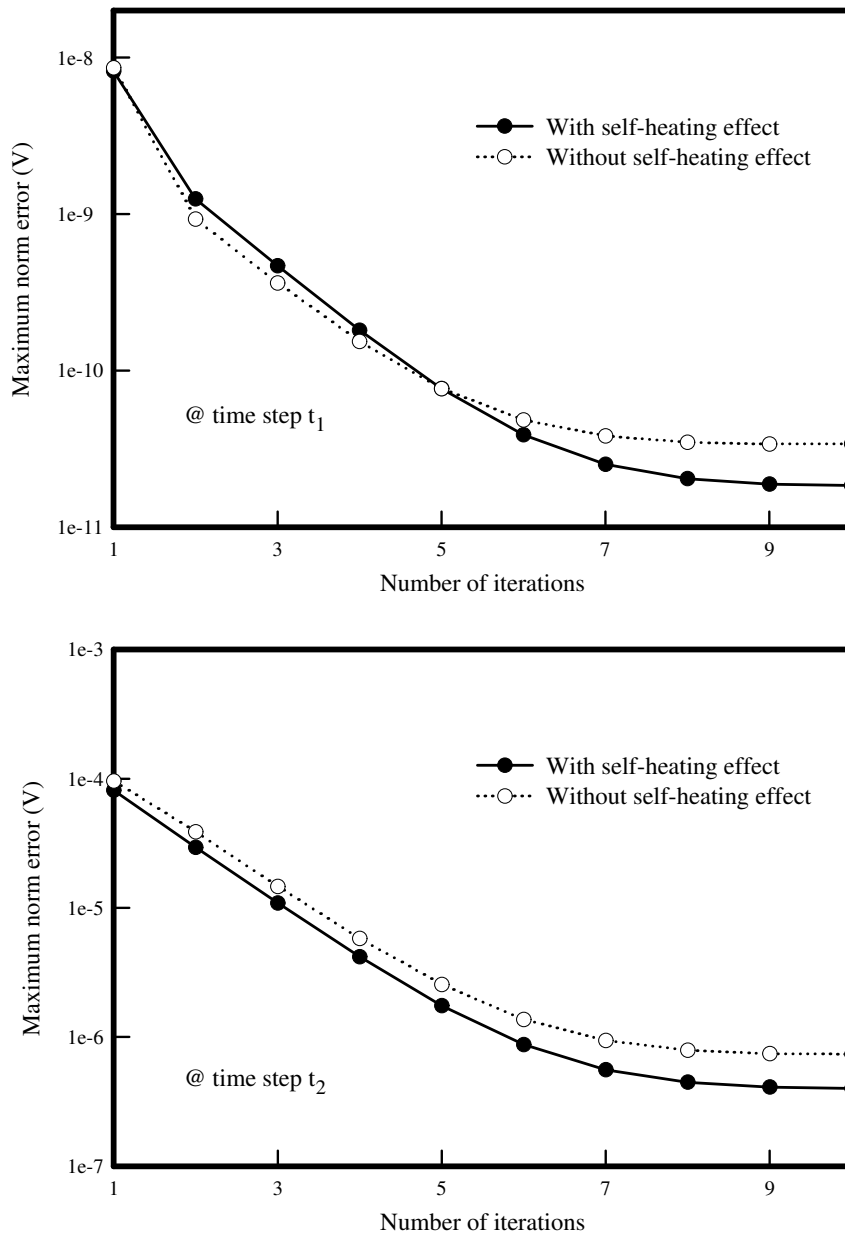


Figure C.4: The maximum norm error versus number of the outer iterations at time steps t_1 and t_2 .

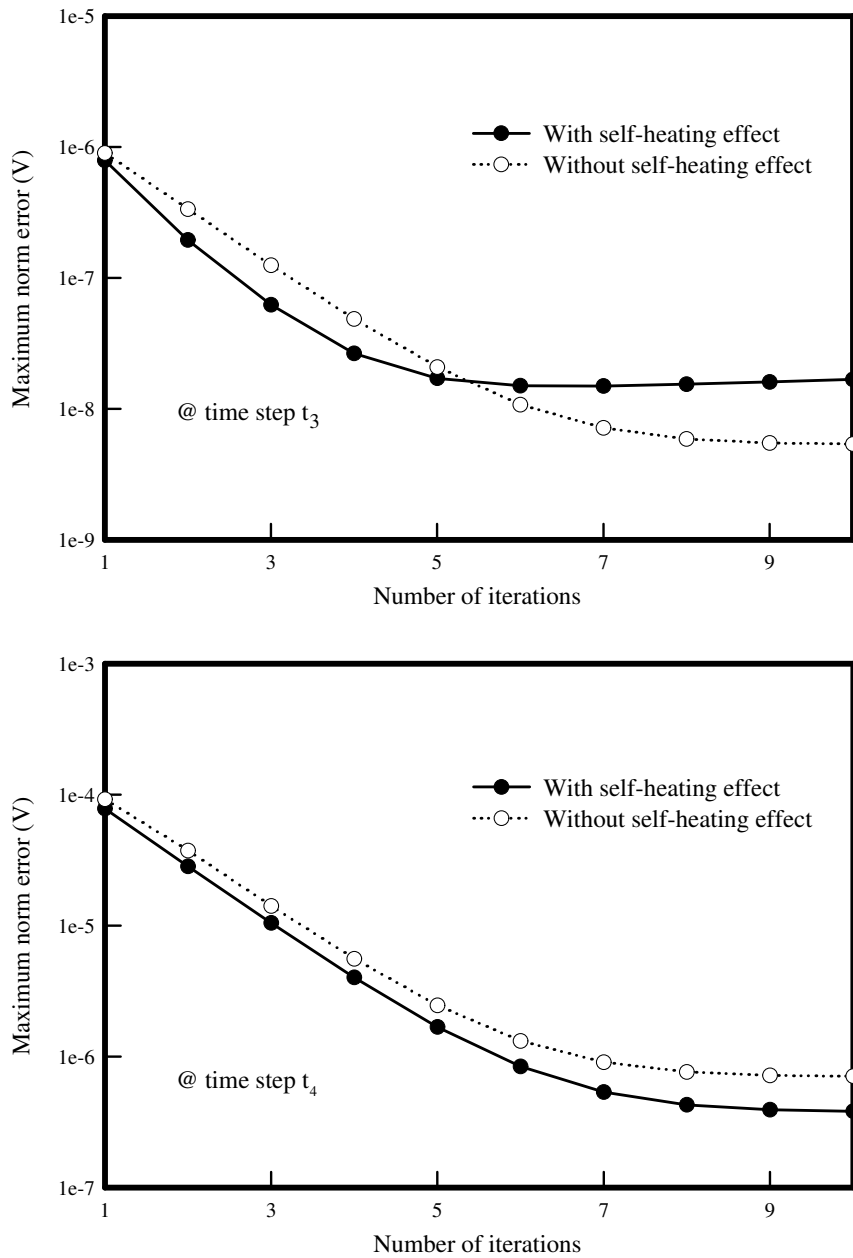


Figure C.5: The maximum norm error versus number of the outer iterations at time steps t_3 and t_4 .

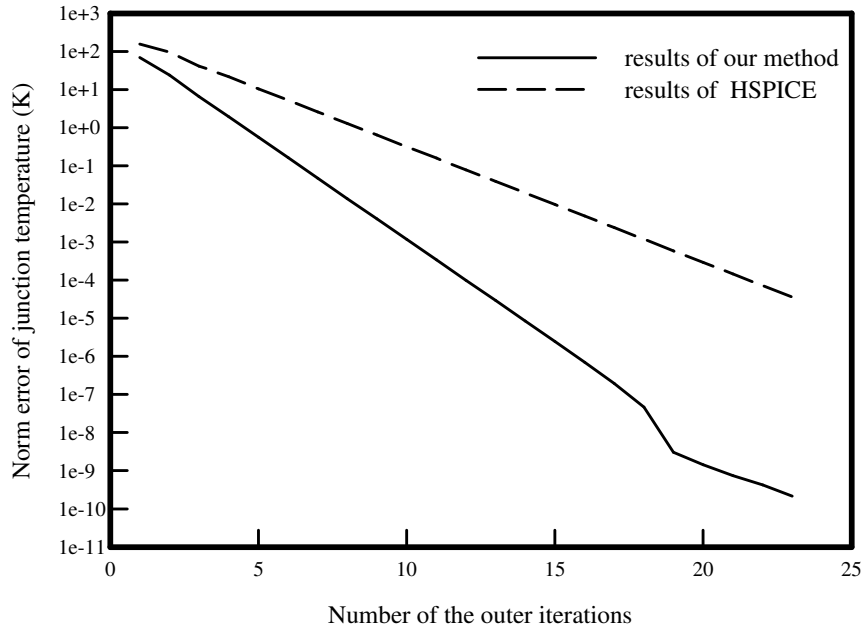


Figure C.6: The maximum norm error of T_J versus number of the outer iterations.

The convergent behavior of junction temperature for both ours and HSPICE's are demonstrated in Fig. C.6. The simulated circuit is plotted in Fig. 2.3. We preset the bias condition as $V_{CC} = 5.0$ V and $I_{IN} = 0.5$ mA. Besides, the power level of this single tone input excitation equals -10 dBm and the frequency is 1.8 GHz. Comparing with HSPICE's results, the maximum norm error of T_J drops more quickly in our simulated results. That shows the computation efficiency of our method.

Appendix D

VITA

- Name: Kuen-Yu Huang.
- Permanent address: No. 288, 10F-1, Park Rd., Hsin-Chu City, Taiwan.
- Date of birth: September 1, 1973.
- Place of birth: Kaohsiung, Taiwan.
- Degree and date to be conferred: Doctor of philosophy in electronics engineering, May, 2005.

Collegiate institution attended	Degree	Date of degree
National Tsing Hua University, Department of Electrical Engineering	B.S.E.E.	June, 1996
National Chiao Tung University, Institute of Electronics Engineering	M.S.E.E.	June, 1998

- Major: Electronics Engineering.
- Title of PHD dissertation: *A Time Domain Approach to High-Frequency Circuit Simulation of Semiconductor Devices.*¹

¹Typeset by the author in L^AT_EX

- Presentation in international conference: "A computational efficient method for HBT intermodulation distortions and two-tone characteristics simulation," in *International Conference on Simulation of Semiconductor Processes and Devices (SISPAD '01)*, Athens, Greece, September 5-7, 2001.



Appendix E

Publication List

1. **Kuen-Yu Huang**, Yiming Li, C.-P. Lee, and S. M. Sze, "A computational efficient method for HBT intermodulation distortions and two-tone characteristics simulation," in *International Conference on Simulation of Semiconductor Processes and Devices, SISPAD*, 2001, pp. 226-229.
2. Yiming Li, **Kuen-Yu Huang**, Cheng-Kai Chen, Chien-Ping Lee, "A Parallel Computational Technique for High Frequency HBT Circuit Simulation," in *Technical Proceedings of 5th ACR/IEEE/SIAM International Conference on Modeling and Simulation of Microsystems (MSM 2002)*, April, 2002, pp. 376-379.
3. **Kuen-Yu Huang**, Yiming Li, and Chien-Ping Lee, "A time-domain approach to simulation and characterization of RF HBT two-tone intermodulation distortion," *IEEE Trans. Microwave Theory Tech.*, vol. 51, pp. 2055-2062, Oct. 2003.

4. **Kuen-Yu Huang**, Yiming Li, and Chien-Ping Lee, "Computer simulation of multifinger heterojunction bipolar transistor with self-heating and thermal coupling models," *Microelectronic Engineering*, vol. 75, pp. 137-144, Aug. 2004.

